KfK 4872
Mai 1991

Chemical and X-Ray Diffraction Analysis on Selected Samples from the TMI-2 Reactor Core

H. Kleykamp, R. Pejsa
Institut für Material- und Festkörperforschung
Hauptabteilung Versuchstechnik
Projekt Nukleare Sicherheitsforschung

Kernforschungszentrum Karlsruhe

KERNFORSCHUNGSZENTRUM KARLSRUHE

Institut für Material- und Festkörperforschung
Hauptabteilung Versuchstechnik
Projekt Nukleare Sicherheitsforschung

KfK 4872

Chemical and X-ray diffraction analysis on selected samples from the TMI-2 reactor core

H. Kleykamp, R. Pejsa

Kernforschungszentrum Karlsruhe GmbH, Karlsruhe

Kernforschungszentrum Karlsruhe GmbH
Postfach 3640, 7500 Karlsruhe 1

ISSN 0303-4003

Chemical and X-ray diffraction analysis on selected samples from the TMI-2 reactor core

Abstract

Selected samples from different positions of the damaged TMI-2 reactor core were investigated by X-ray microanalysis and X-ray diffraction. The measurements yield the following resolidified phases after cooling: Cd and In depleted Ag absorber material, intermetallic Zr-steel compounds, fully oxidized Zircaloy, UO_2-ZrO_2 solid solutions and their decomposed phases, and Fe-Al-Cr-Zr spinels. The composition of the phases and their lattice parameters as well as the eutectic and monotectic character can serve as indicators of local temperatures of the core. The reaction sequences are estimated from the heterogeneous equilibria of these phases. The main conclusions are: (1) Liquefaction onset is locally possible by Inconel-Zircaloy and steel-Zircaloy reactions of spacers and absorber guide tubes at 930 °C. However, increased rates of dissolution occur above 1200 °C. (2) UO_2 dissolution in the Inconel-steel-Zircaloy melt starts at 1300 °C with increased rates above 1900 °C. (3) Fuel temperatures in the core centre are increased above 2550 °C, liquid $(U,Zr)O_2$ is generated. (4) Square UO_2 particles are reprecipitated from the Incoloy-steel-Zircaloy-UO_2 melt during cooling, the remaining metallic melt is oxygen poor; two types of intermetallic phases are formed. (5) Oxidized Fe and Zr and Al_2O_3 from burnable absorber react to spinels which form a low melting eutectic with the fuel at 1500 °C. The spinel acts as lubricant for fuel transport to the lower reactor plenum above 1500 °C. (6) Ruthenium (Ru-106) is dissolved in the steel phase, antimony (Sb-125) in the α-Ag absorber during liquefaction. (7) Oxidation of the Zircaloy-steel phases takes place mainly in the reflood stage 3 of the accident scenario.

Chemische und röntgenographische Analysen an ausgewählten Proben aus dem TMI-2-Reaktorkern

Zusammenfassung

Ausgewählte Proben aus verschiedenen Positionen des zerstörtenTMI-2-Reaktorkerns wurden durch Röntgenmikroanalyse und Röntgenbeugung untersucht. Aus den Messungen ergeben sich folgende Hauptphasen nach der Abkühlung: Cd- und In-abgereichertes Ag-Absorbermaterial, intermetallische Zr-Stahl-Phasen, vollständig oxidiertes Zircaloy, UO_2-ZrO_2-Mischkristalle und zweiphasige Bereiche sowie Fe-Al-Cr-Zr-Spinelle. Die Zusammensetzung der Phasen und deren Gitterkonstanten sowie der eutektische oder monotektische Charakter können als Indikatoren für die lokalen Temperaturen im Reaktorkern dienen. Die Reaktionsabfolge wird aus den heterogenen Gleichgewichten dieser Phasen abgeleitet. Die wesentlichen Schlußfolgerungen sind: (1) Der Beginn der Flüssigphasenbildung ist durch Inconel-Zircaloy- und Stahl-Zircaloy-Reaktionen der Abstandshalter und Absorberführungsrohre bei 930 °C lokal möglich. Eine höhere Auflösungsgeschwindigkeit tritt jedoch erst oberhalb 1200 °C auf. (2) Die UO_2-Auflösung in der Inconel-Stahl-Zircaloy-Schmelze beginnt bei 1300 °C, eine höhere Geschwindigkeit tritt oberhalb 1900 °C auf. (3) Die Brennstofftemperatur im Kernzentrum steigt über 2550 °C an, eine $(U,Zr)O_2$-Schmelze wird gebildet. (4) Quadratische UO_2-Partikel werden während der Abkühlphase aus der Inconel-Stahl-Zircaloy-UO_2-Schmelze ausgeschieden, die verbleibende Schmelze ist sauerstoffarm; zwei verschiedene intermetallische Phasen werden gebildet. (5) Oxidiertes Fe und Zr sowie Al_2O_3 aus dem abbrennbaren Absorber reagieren zu einem Spinell, der mit dem Brennstoff ein niedrig schmelzendes Eutektikum bei 1500 °C bildet. Der Spinell wirkt oberhalb 1500 °C als Schmiermittel für den Brennstofftransport in das untere Reaktorplenum. (6) Ruthenium (Ru-106) wird im Stahl, Antimon (Sb-125) wird im α-Ag-Absorbermaterial während der Flüssigphasenbildung aufgelöst. (7) Eine Oxidation der Zircaloy-Stahl-Phasen erfolgt hauptsächlich in der Stufe 3 (Flutungsphase) des Unfallablaufs.

Contents

1. Introduction

The nuclear research centre Karlsruhe (KfK) is one of the partners of the Committee on the Safety of Nuclear Installations within the Organisation for Economic Cooperation and Development (CSNI-OECD) which submitted in agreement with the respective research establishments a selection of samples from the molten core region of the damaged Three Mile Islands 2 reactor (TMI-2) for materials analysis. The approach of this programme is the understanding of the reactions of the core components after the TMI-2 accident with regard to their sequences and intermediate stages as well as estimations of the local temperature and involved oxygen partial pressures in the different regions of the core. The numerous examinations provide information in the areas of material interactions, distribution of fission products and relocation phenomena.

The main goal of this contribution is hoped to be attained by elemental analysis and complementary crystal structure determinations of selected samples from the core. The principle constituents of the inventory are UO_2 fuel, Zircaloy-4 claddings, Inconel-718 spacers, steel-304 absorber guide tubes, Ag-Cd-In absorber and Al_2O_3-B_4C poison absorber. The TMI-2 core composition is compiled in table 1.

Table 1: TMI-2 core composition ($\geq$ 0.1 % per component).

constituent	mass percent
UO_2	71.8
Zr	19.9
Fe	3.0
Ag	1.8
Cr	1.0
Ni	0.91
In	0.33
Sn	0.32
Al_2O_3	0.18
B	0.14
Cd	0.12
rest	0.58

The spatial and temporal paths of the phase formation is to be explained by the respective multi-component phase diagrams which are compiled in the appendix.

KfK received in mid 1987 altogether eighteen TMI-2 samples for post-irradiation studies which include metallography, autoradiography, density measurements, scanning electron microscopy, X-ray microanalysis and X-ray diffraction. The samples are listed below:

1. Fuel rod segment No. 5 from M2 fuel assembly
2. Core bore, core D8-P1, section A
3. Core bore, core G12-P1, section B
4. Core bore, core K9-P1, section F
5. Core bore, core K9-P2, section A
6. Core bore, core O7-P4, section B
7. Core bore, core debris D4-P1, section B
8. Core bore, core debris G8-P4, section A
9. Core bore, core debris G8-P5, section A
10. Core bore, core debris G12-P10, section C
11. Core bore, core debris K9-P3, section B
12. Core bore, core debris K9-P4, section C
13. Core bore, core debris N5-P1, section B
14. Core bore, core debris O7-P3
15. Core bore, core debris O7-P8, section B
16. Lower plenum core debris rock 11-1, section A
17. Lower plenum core debris rock 11-5, section A
18. Lower plenum core debris rock 11-7, section A

2. Experimental details

All samples were photographed in the as-received state. Density measurements were performed on selected samples by the immersion method in carbon tetrachloride. Specific areas of the samples were cut-off from the material where an optimum of information was suggested for further analysis. The samples were mounted in epoxy resin and ground in the final stage with 0.3 µm diamond paste to guarantee minimum surface roughness. Light-optical photography was complemented by α and β-γ autoradiography. The preparations of the samples were done in the metallography group of the hot cells at KfK.

The following shielded analytical instruments were available for further analysis:

- scanning electron microscope, Philips SEM 500X,
- X-ray microanalyzers, Cameca MS46 and Jeol JRXA 50,
- X-ray diffractometer, Siemens Kristalloflex, with a curved graphite monochromator to suppress the γ-radiation background.

The results of the quantitative elemental analysis were ZAF corrected to weight fractions. The detection limit of the elemental analysis is about 0.01 wt.%. As oxygen could not be quantitatively analyzed in all cases and the phases were multicomponent in character, the crystallographic investigations were a substantial support for the elemental analysis.

3. Density measurements

Density measurements were made by the immersion method in carbon tetrachloride on five samples of the core debris and on one sample of the lower plenum rock in the as-received state. For example, the view of the core debris O7-P3 is given in fig. 30. The mass and the density of the samples are compiled in table 2. The density ρ ranges between 6.7 and 8.3 Mg/m^3. The main phases are $(U,Zr)O_2$ (ρ_0 up to 10.96 Mg/m^3), $Zr(U, Fe)O_2$ ($\rho_0 \approx 6$ Mg/m^3), steel components ($\rho_0 \approx 8$ Mg/m^3) and absorber materials ($\rho_0 \approx 10$ Mg/m^3). It should be noted that the ceramic phase has up to 20 % porosity. Hence, the average of the densities of the components falls in between the experimentally determined density range.

Table 2: Immersion density measurements of selected as-received samples in CCl_4 at KfK.

sample	mass in mg	density in Mg/m^3
rock G8-P4-A-1	54810	7.84
rock G8-P4-A-2		7.77
rock G12-P10-C	28954	7.29
rock K9-P4-C	18593	6.70
rock N5-P1-B	5978	8.31
rock O7-P3-0	7395	7.82
lower plenum rock 11-1-A	905	8.19

4. X-ray microanalysis and X-ray diffraction results

The whole of the light-optical microstructures of eighteen samples was prepared by the hot cells of KfK. This material was the basis for the selection of seven samples for further investigations by X-ray microanalysis and X-ray diffraction. The selected samples are compiled in table 3, their positions in the TMI-2 end-state configuration are given in fig. 1.

Table 3: TMI-2 samples investigated at KfK by X-ray microanalysis (XMA) and X-ray diffraction (XRD).

sample, position	total mass before sectioning	XMA	XRD
fuel segment No. 5, core position M2	56.0 g	X	
core bore K9-P1-F, lower crust region	266.6 g	X	X
core bore D8-P1-A, lower crust region	90.1 g	X	X
lower plenum core debris rock 11-5-A	15.0 g	X	X
lower plenum core debris rock 11-7-A	25.1 g		X
previously molten rock O7-P3-1	112.3 g	X	
loose core debris O7-P8-B	21.8 g	X	

a. Fuel rod segment No. 5 from core position M2

A view of a broken pin end of the fuel rod segment No. 5 from the core position M2 fuel assembly of TMI-2 is given in fig. 2. A metallographic cross-section was prepared by cutting a cylindrical disk in a distance between 19 and 28 mm from the open end tip. Three complementary 120° sections, the light-optical microstructure, the α autoradiograph and the β-γ autoradiograph, of the polished surface 19 mm from the open end tip are assembled in fig. 3. The extremely high exposure times of the autoradiographs should be noted. A slight increase of the α activity was observed at the fuel rim. This is the result of the higher plutonium production due to neutron resonance absorption of U-238 in the eV energy range at the fuel surface. The quantitative analysis of the elements Pu, Nd, Cs and Xe as a function of the relative fuel radius r/r_0 is compiled in table 4. The cross-section averaged concentrations are 0.04 % PuO_2, < 0.01 % Nd and 0.01 % Cs. Xenon was not detected.

These values result in a local burnup of 900 MWd/t U which corresponds to 0.1 % of the heavy atoms. The light-optical and the scanning electron optical microstructures of the fuel in fig. 4 showed no difference of the pore distribution and the pore shape in the centre and the surface region of the fuel. Quantitative X-ray microanalysis of the Zircaloy-4 cladding revealed 1.5 wt.% tin and about 0.5 wt.% oxygen in the inner uneffected cladding region. The outer surface was covered by a 4 µm thick single-phase Zr-1.2 wt.% Sn oxide layer that is equivalent to $Zr_{0.99}Sn_{0.01}O_{2-x}$, see fig. 5. The inner Zircaloy surface incorporated up to about 12 wt.% oxygen. The oxygen profile in fig. 5 falls down to oxygen concentrations below 1 % within 5 µm distance from the inner surface. No oxide layer formation was observed on the inner clad surface. The oxygen diffusion coefficient in α-Zr was estimated from the period of increased core temperature (3 h) and the 4 µm thick ZrO_2 layer given in fig. 5. This results in $D_O = 7 \cdot 10^{-16}$ m²/s. By application of the known temperature dependence of the oxygen diffusion in α-Zr, the maximum cladding temperature in this area of the fuel pin assembly was estimated to be 650 °C.

Table 4: Quantitative analysis of Pu, Nd, Cs and Xe on a broken pin of fuel rod segment No. 5, section 1, from upper end of core position M2 fuel assembly of TMI-2, as a function of the relative fuel radius r/r_0.

r/r_0	Pu* in wt.% PuO_2	Nd in wt.% Nd	Cs in wt.% Cs	Xe in wt.% Xe
0.94	0.05 ± 0.01	< 0.01	< 0.01	0
0.98	0.04 ± 0.01	< 0.01	0.03 ± 0.02	0
0.999	0.02 ± 0.02	< 0.01	0.01 ± 0.02	0

* average value corresponds to 900 MWd/t U (≙ 0.1 %) burnup

b. Core bore K9-P1, section F, from the lower crust region

Section F of core bore K9-P1 was re-polished at KfK. The microstructure in fig. 6 shows the plate which was divided into two parts, parallel and perpendicular to the fuel pin remnants. The left hand part of the perpendicular section 1 was embedded (fig. 7) and was used for X-ray microanalysis and X-ray diffraction. The electron optical microstructures in fig. 11 and 15 as well as the congruent α autoradiograph in fig. 8 depict the (β radiation free) quadratic UO_2 particles about 50 to 100 µm in length, which were reprecipitated from the Zry-steel-UO_2 melt as primary crystals. The positions a, b, c and d in the enlarged light-optical microstructure in fig. 9a and b refer to the qualitative and quantitative microanalyis in the areas of the microstructure details indicated in fig. 10, 12, 14 and 16. The

qualitative analysis includes the absorbed and the secondary electron images (AEI + SEI) and the distribution images of the elements U, Zr, Fe, Cr, Ni, Sn, Ag, In, Al and O in 250 x 350 µm areas in fig. 11, 13, 15 and 16. The numbers in these images refer to the positions where quantitative point analyses were made. The quantitative analysis of the phases which were observed in the position a, b, c and d of fig. 9 are compiled in the tables 5, 6, 7 and 8.

Distinct families of phases could be identified in the lower crust region of core bore K9-P1, section F:

The Ag-In-Cd absorber material is very bright in appearance and mostly not well polished due to the low hardness. The isothermal section of the ternary Ag-In-Cd system at 315 °C which is illustrated in fig. E of the appendix characterizes the α-Ag(In,Cd) solid solution. The initial composition 80 % Ag - 15 % In - 5 % Cd (marked by a black dot in fig. E) is shifted to the Ag apex within the solid solution range. Typical compositions are 88 % Ag - 10 % In - 1 % Cd - 1 % Sn. The incorporated tin originates from the Zircaloy cladding during its melting.

Laves phases ZrM_2 are formed in the Zr-Fe and Zr-Cr systems, but not in the Zr-Ni system. Further, Zr_2M phases (t-Al_2Cu type or η-Ti_2Ni type) occur in the Zr-Fe and Zr-Ni systems, see fig. A and B of the appendix. The latter phases can be stabilized by oxygen resulting in the compositions Zr_6Fe_3O, Zr_3Cr_3O and $Zr_4Ni_2O_x$, see fig. C and D of the appendix. Both types of multi-component ZrM_2 and Zr_2M phases were observed in the lower crust region. The compositions of the two-phase Zr-Cr-(Fe + Ni-rest) couples are projected onto the isothermal section at 1000 °C of the ternary Zr-Cr-Fe system in fig. B of the appendix. The measured compositions are indeed located near those of the phases Zr_2Fe and $Zr(Cr,Fe)_2$. These phases are metallic in appearance. The Zr_2M phases have dark grey fringes along the cracks and contain in addition some at.% oxygen. This is attributed to the η-phase with the observed composition $Zr_3M_5O_2$. The intergranular and surface oxidation of this phase occurred in the later reflood stage of the accident when the reaction of these phases with water started.

Table 5: Quantitative analysis of phases in position a of core bore K9-P1, section F, sample 1, fig. 10 and 11.

position	element	conc. in wt.%	conc. in at.%	phase
13/14/17	Ag In Cd Sn	87 10 1.2 1.2	88 10 1.2 1.0	α-Ag (In) (bright)
15/16	U Zr Fe,Ni,In O	85 2 1 12	31 2 2 65	UO_2 (dark, squares)
18/23	Zr Fe Ni Cr U Al O	46/45 32/34 9/4 5/8 2/3 1/1 ≈ 4/5	30 36 7 8 0.6 2 16	ZrM_2 phase oxidized
19	Zr Ag In Ni U Fe O	78 6 5 5 2 2 ≈ 2	71 5 4 7 1 3 9	β-Zr (Ag,In)? (light grey)
20/21	Zr Ni Sn Fe Al,In,Ag O	60/73 1/5 0/4 1/2 ≈ 3 ≈ 20	35 2 1 1 1 60	m-ZrO_{2-x} (dark)
22	Zr Fe Cr Ni U Al,Ag,Sn,Mn,In	74 15 4 3 3 1	66 22 6 4 1 1	Zr_2(Fe,Cr) (light)

Table 6: Quantitative analysis of phases in position b of core boreK9-P1, section F, sample 1, fig. 12 and 13.

position	element	conc. in wt.%	conc. in at.%	phase
1/2/3	Ag In Cd Sn	87 - 89 9 - 10 0.8 - 1.4 0.7 - 1.4	89 9 1 1	α-Ag (In) (bright)
4/6	Zr Ni Fe U Ag Cr,In,Sn,Al O	67 - 69 13 8 - 9 4 2 2 - 3 2	56 17 12 1 1 4 9	β-Zr ?
5	Zr Fe Cr Ni U	44 34 9 8 3	34 43 12 10 1	$Zr(Fe,Cr,Ni)_2$ (Laves phase)
7/8	Zr In Ni Fe Ag,Sn,Al O	69 - 71 7 - 13 3 2 2 ≈ 20	34 4 2 2 1 57	m-$Zr(In)O_2$
9/10	Zr Fe Ni Cr Ag,In,Sn,Al,U	≈ 50 23 13 9 4	39 30 16 12 3	$Zr(Fe,Cr,Ni)_2$ (Laves phase)
12	Zr Ni Sn Ag Fe,In,Al,Cr O	≈ 54 < 10 ≈ 10 < 4 2 ≈ 20	27 < 8 4 < 2 2 58	$Zr(Ni,Sn)O_{2-x}$*

* possibly Ni_3Sn_2 is submicroscopically precipitated in the ZrO_2 matrix.

Table 7: Quantitative analysis of phases in position c of core bore K9-P1, section F, sample 1, fig. 14 and 15.

position	element	conc. in wt.%	conc. in at.%	phase
1/2	U	83	30	
	Zr	2.8 - 3.2	3	
	Ni	0.4		
	Fe	0.2		$U(Zr)O_2$
	In	0.2	2	(dark,
	Cr	0.1		squares)
	Mn	0.1		
	Ag	0.1 - 0.3		
	In,Sn	0 - 0.2	0	
	Al	0.1		
	O	< 12	65	
3/4/5	Ag	87	88	α-Ag(In)
	In,Ni,Fe,O, ...	13	12	(bright)
6/7	Zr	52 - 55	26	
	Sn	10	4	
	Ni	5 - 7	5	
	Cr	1 - 7	3	m-$Zr(Sn)O_2$*
	Ag	4	2	(dark)
	Fe	3	2	
	Al	1	2	
	O	≈ 20	56	
8/12/14	Fe	40 - 50	46	
	Zr	30 - 40	28	
	Ni	< 7	< 10	ZrM_2
	Cr	3 - 10	8	(Laves phase)
	U	2	1	
	O	2 - 3	< 10	
10/11	Zr	62/64	54	
	Sn	13/17	10	
	Ni	7	10	
	Ag	4	3	?
	In	2/3	2	
	Fe,Cr,Mn	4/3	5	
	O	3/4	17	
9/13	Zr	67	66	
	Ni	10	15	
	Fe	10	15	
	U	5	2	$Zr_2(Fe,Ni)$
	Ag	2	2	
	Cr,In,Sn,O	4	3	

* possibly Ni_3Sn_2 is submicroscopically precipitated in the ZrO_2 matrix.

Table 8: Quantitative analysis and structure of phases in the B,A and fuel region in position d of core bore K9-P1, section F, sample 1, fig. 16

element	conc. in wt.%			
	region B	region A		fuel region
	metallic phase	Zr oxide	absorber mat.	UO_2
U	0	0	0	88
Zr	47	60	0	0
Fe	35	8	0	0
Cr	9	1	0	0
Ni	5	7	0	0
Al	1	0.5	0	0
Ag	0	0	88	0
In	0	0	9	0
Cd	0	0	1	0
Sn	0	0	1	0
O	0.4	24	< 1	12
phase and structure	$Zr(Fe,Cr)_2$ Laves phase $MgCu_2$ type a = 707 pm ?	m-$Zr(Fe,Ni)O_{2-x}$ Baddeleyit ZrO_2 (III) type a = (514.5 ± 0.6) pm b = (520.9 ± 0.6) pm c = (533.1 ± 0.5) pm β = (99.2 ± 0.1)°	α-Ag(In) fcc. Cu type a = 409 pm	UO_2 fcc. CaF_2 type a = 545.9 pm*

* the measured lattice parameter is an average of the fuel pin remnants and the recrystallized $U(Zr)O_2$.

A further family of metallic phases is light in appearance and consists of 62 to 78 wt.% Zr as the host metal, appreciable amounts of absorber material components and some steel components. It is not clear from the available phase diagrams whether this phase is a β-Zr solid solution or a stoichiometric multi-component intermetallic phase.

Monoclinic m-ZrO_2 particles were observed which are dark grey in appearance. This phase contains minor amounts of iron and other steel components, very small amounts of the components of the absorber material and no uranium and was formed in equilibrium with the metallic melts (table 5, 6 and 7). m-ZrO_2 can dissolve up to 20 mol% Fe_2O_3. Furthermore, ZrO_2 layers were observed which contain steel components, but no absorber material components (table 8). These layers are direct remnants from the oxidized Zircaloy cladding.

Steel and zirconium form a multinary eutectic system. A liquid appearing first locally at 930 °C and above 1200 °C in higher amounts can dissolve UO_2. During cooling even from higher temperatures by crossing the liquidus line, Laves phases and quadratic UO_2 particles are reprecipitated. The latter contain 3 wt.% Zr, for precise quantitative analysis see table 7, positions 1/2. The observed low ZrO_2 fraction in the reprecipitated UO_2 and the $Zr_{1-y}O_y$-UO_2 sections of the ternary U-Zr-O system (one example of the series with y = 0 is presented in fig. F of the appendix) give evidence that the metallic melt is very oxygen poor; this is due to the presence of liquid steel and hence, due to a decreased affinity of zirconium to oxygen.

The UO_2 fuel pin remnants which contain no third components were not in direct contact with liquid phases during the transient, see table 8. Steel does not interact with UO_2 (see fig. J of the appendix).

The X-ray diffraction work on core bore K9-P1, section F resulted in the identification of four phases:

- UO_2 (CaF_2 type) with the observed lattice parameter a = 545.9 pm which is smaller than that for pure stoichiometric UO_2 with a = 547.0 pm. The elemental analysis has shown (table 5 and 7) that about 10 mol % ZrO_2 is dissolved in the quadratic primary crystals which results in a lattice contraction, see fig. H of the appendix. 10 mol% ZrO_2 in UO_2 reduces the lattice paramter to a = 543.4 pm. The observed lattice parameter is an average of those for pure UO_2 from the pin remnants and for the reprecipitated $(U,Zr)O_2$.
- Monoclinic ZrO_2 (ZrO_2 (III) type) with the observed lattice parameters a = 514.5 pm, b = 520.9 pm, c = 533.1 pm, β = 99.2° which are higher than those for pure ZrO_2 with a = 513.8 pm, b = 520.4 pm, c = 531.3 pm, β = 99.2°. The

elemental analysis has shown that iron and nickel are dissolved in ZrO_2. This is in agreement with phase studies in the ZrO_2-Fe_2O_3 system: The maximum Fe_2O_3 solubility corresponds to the formula m-$Zr_{0.65}Fe_{0.35}O_{2-x}$ with the lattice parameters a = 514.6 pm, b = 519.3 pm, c = 532.3 pm, β = 99.3°.

- Absorber material (Cu type) with the observed lattice parameter a = 409 pm which is slightly higher by the indium dissolution than the lattice parameter of pure silver with a = 408.6 pm.
- Laves phase $Zr(Fe,Cr)_2$ with the observed lattice parameter a ≈ 707 pm which is similar to that of the pure Lave phases $ZrFe_{2\pm x}$, a = 701.5 - 708.7 pm, and $ZrCr_2$, a = 720.8 pm.

c. Core bore D8-P1, section A, from the lower crust region

Section A of core bore D8-P1 was re-polished at KfK for general metallographic documentation. A smaller area was cut-off and was selected for X-ray microanalysis, the microstructure is documented in the upper half of fig. 17. The β-γ autoradiograph after 40 seconds exposure time in the lower half of the figure shows the fuel pin remnants and two metallic areas one of which is free of β-γ activity. An enlarged composited microstructure is shown in fig. 18 where the positions a, b and c are marked, which were selected for qualitative and quantitative X-ray microanalysis. The microstructure details are given in fig. 19, 21 and 22. The secondary and absorbed electron images and the elemental distribution images in fig. 20 (area a in fig. 18 and 19) are characterized by a metallic plug in a crack of the fuel remnant and give already qualitatively evidence of different phases: UO_2, $Zr(U)O_2$, Fe, Ag-In, Ni-Sn. The same holds for area b in fig. 21 where Fe and Cr as well as Zr and Cr are associated to form oxide phases; further, steel, absorber material and the Ni-Sn precipitates can be recognized.

The quantitative analysis of the positions a, b and c in fig. 18 are compiled in table 9, 10 and 11, resp. The following phases were observed:

- absorber material, Ag with In contents up to 18 wt.%
- $Ni_3(Sn,In)_2$ precipitated dendritically from the Ag matrix
- γ-Fe-Ni-Cr with Ni contents up to 25 wt.%
- UO_2 fuel pin remnants
- Mo base alloy, possibly $Mo_2(Fe,Cr)_3$
- Zr rich $(Zr,U,Fe)O_2$
- in minor amounts: FeO, Cr_2O_3

Table 9: Quantitative analysis of phases in position a of core bore D8-P1, section A, fig. 19 and 20.

position	element	conc. in wt.%	conc. in at.%	phase
1	Zr U Fe O	52 28 0.2 ≈ 20	29 6 0.2 ≈ 65	$Zr_{0.82}U_{0.17}Fe_{0.01}O_{2-x}$
2	Ag In Sn Cd	85 13 2 0.3	86 12 2 0.3	α-Ag (In, Sn,Cd)
3	Sn Ni In Ag Fe	51 41 7 0.5 0.4	36 58 5 0.4 0.5	$Ni_3(Sn,In)_2$
4	Fe O	≈ 78 ≈ 22	≈ 50 ≈ 50	FeO
5	U Zr O	88 0 12	34 0 66	UO_2

Table 10: Quantitative analysis of phases in position b of core bore D8-P1, section A, fig. 18 and 21.

position	element	conc. in wt.%	conc. in at.%	phase
6	Zr U Fe O	61 16 0.5 ≈ 22	31 3 0.4 ≈ 65	$Zr_{0.90}U_{0.09}Fe_{0.01}O_{2-x}$
7	Zr U Fe O	38 - 44 31 - 35 4 - 7 ≈ 21	23 7 5 ≈ 65	$Zr_{0.66}U_{0.20}Fe_{0.14}O_{2-x}$
8	Ag In Sn Cd	80 13 6 0.4	82 12 6 0.4	α-Ag (In, Sn,Cd)
9	Ni Sn In Fe Ag	44 51 4 0.8 0.5	60 35 3 1.2 0.4	$Ni_3(Sn,In)_2$
10	Fe Ni Cr Mo Ru	65 25 7 2.2 0.4	66 24 8 1.3 0.2	γ-Fe(Ni,Cr)
11	Zr Cr U Fe O	49 15 13 1.4 ≈ 21	24 13 3 1 59	probably multi-phase ZrO_2-Cr_2O_3?
12	Mo Fe Cr Ni Nb	53 21 20 2 4	40 27 27 3 3	α-Mo(Fe,Cr)? $Mo_2(Fe,Cr)_3$?

Table 11: Quantitative analysis of phases in the region of position c of core bore D8-P1, section A; fig. 22 is similar to the region of X-ray microanalysis .

appearance	element	conc. in wt.%	conc. in at.%	phase
dark grey	Zr U Fe O	60 16 4 ≈ 20	29 3 3 ≈ 65	$Zr(U,Fe)O_{2-x}$
bright matrix	Ag In Fe Sn Cd	77 18 3 1.2 0.8	77 17 3 2.4 0.8	α-Ag (In, Sn)
precipitates in α-Ag	Ni Sn In Ag Fe	42 51 6 0.9 0	59 36 4 0.7 0	$Ni_3(Sn,In)_2$
yellow matrix	Fe Ni Cr Mo In Al Ru	68 16 8 3 3 0.6 0.5	70 16 9 2 1.5 1.3 0.3	γ-Fe(Ni,Cr)
incompletely precipitated in γ-Fe	Ni Sn In Ag,Fe,Ru	39 54 7 0	57 38 5 0	$Ni_3(Sn,In)_2$
light grey precipitates	Mo Fe Cr Nb Ni Ru	57 21 16 4 1.6 0.2	44 28 22 4 2.0 0.1	$Mo_2(Fe,Cr)_3$?

ZrM_2 and Zr_2M phases (M = Fe, Cr, Ni) were not observed in the investigated sample core bore D8-P1-A, compared to core bore K9-P1-F from the same lower crust region. The β autoradiograph in fig. 17 gives evidence of β-γ active components in the metallic phases. This correponds to position 10 in fig. 21 where up to 0.4 wt.% Ru were observed in the γ-steel matrix. The β autoradiograph gives further evidence of β-γ activity in the $Ni_3(Sn,In)_2$ precipitates; however, no fission products were found. The radioactivity is possibly due to a Ni-62-63 activation or to the presence of Sb-125 which could not be unequivocally detected by X-ray microanalysis in this phase.

X-ray diffraction analysis was made on the whole area of the section. The results yield a multiplicity of crystal structures which could be attached to the various phases with the outcome of the elemental analysis. The separation of the peaks and the calculation of the lattice parameters are summarized in table 12.

The following phases could be identified:

- m-ZrO_2 with the lattice parameters a = (516.1 ± 0.2) pm, b = (522.6 ± 0.4) pm, c = (532.7 ± 0.2) pm, β = (99.1 ± 0.1)°; this phase has incorporated the elements Fe and Cr. Especially Fe_2O_3 stabilizes the monoclinic structure to higher temperatures.
- UO_2 with the lattice parameter a = (546.4 ± 0.3) pm which is attributed to c-$(U,Zr)O_2$ at the maximum ZrO_2 solubility at 1300 °C, see fig. G of the appendix. The lattice parameter corresponds to the composition $U_{0.98}Zr_{0.02}O_2$ according to fig. H of the appendix.
- α-Ag with the lattice parameter a = 414.5 pm which is In rich and Cd depleted absorber material.
- γ-Fe-Ni-Cr with the lattice parameter a = 358 pm originating from AISI 304 steel and Inconel 718.
- the hexagonal Ni_3Sn_2 phase which has incorporated In in minor concentrations with the lattice parameters a = 408.1 pm and c = 512.3 pm.

Some X-ray diffraction lines could not be unequivocally attributed to specific phases; the 2θ values are: 24.25; 40.15; 41.44; 45.35.

Table 12: X-ray diffraction pattern of section A of core bore D8-P1 (Cu Kα).

phase	2θ	d in pm	hkl	lattice parameters
m-$Zr(U,Fe)O_2$	28.23	316.1	- 111	interference with UO_2
	31.36	285.2	111	
	34.09	263.0	002	
	35.25	254.6	200	a = (516.1 ± 0.2) pm
	40.69	221.7	- 211	b = (522.6 ± 0.4) pm
	49.15	185.4	022	c = (532.7 ± 0.2) pm
	50.00	182.4	- 220	β = (991. ± 0.1)°
	50.49	180.8	- 122	
	53.95	170.0	202	
	55.25	166.3	013	
$U(Zr)O_2$	28.23	316.1	111	(a = 547.5 pm) interference with ZrO_2
	32.80	273.0	200	a = 546.1 pm }
	47.04	193.2	220	a = 546.4 pm } $\bar{a}$ = (546.4 ± 0.3) pm
	55.76	164.9	311	a = 546.8 pm }
Ag(In,Sn)	37.60	239.2	111	a = 414.3 pm
	43.65	207.4	200	a = 414.7 pm
	63.50	146.5	220	a = 414.4 pm
γ-steel	43.65	207.4	111	(a = 359.1 pm) interference with Ag
	51.09	178.8	200	a = 357.5 pm
$Ni_3(Sn,In)_2$	30.70	291.2	101	hexagonal
	43.65	207.4	102	a = (408.1 ± 0.3) pm
	44.4	203.9	110	c = (512.3 ± 0.6) pm
	24.25	367.0		possibly { $Zr_2(Fe,Cr,Ni)O$
	40.15	224.6		{ α-Mo-Cr-Fe
	41.44	217.9		{ ε-Fe_7Mo_6
	45.35	200.0		{ σ-FeMo

d. Lower plenum core debris rock 11-5, section A

The material was removed from the surface of the loose debris bed in the lower plenum prior to the defuelling of the reactor vessel. Section A of the lower plenum core debris rock 11-5 was repolished at KfK. A view of three surfaces of the parallelepiped is given in fig. 23. The material is characterized by a foamy structure. The upper left area denoted sample 2a was prepared for X-ray microanalysis and X-ray diffraction. The light-optical microstructure and a detail are illustrated in fig. 24. The black frames in the detail refer to the investigated areas in fig. 26 and 27. The α autoradiograph in fig. 25 is congruent with the upper microstructure of fig. 24. Two phases can be recognized in the α autoradiograph. The high active phase is in essential a UO_2-ZrO_2 solid solution with different U/Zr ratios. The lower active region is two-phase, eutectic in appearance with $(U,Zr)O_2$ as the primary crystals and a Fe-Cr-Al spinel in the eutectic. The eutectic character of the pseudobinary $(U,Zr)O_2$-spinel system is illustrated in the secondary electron images and the element distributions of U, Cr, Fe and Al in fig. 26 and 27. The eutectic temperature is estimated to be 1500 °C. The quantitative analysis of the two phases in this range is compiled in table 13 resulting in $U_{0.63}Zr_{0.33}Fe_{0.04}O_2$ and

Table 13: Quantitative analysis of the phases in sample 2a, section A of lower plenum core debris rock 11-5 (figs. 18 - 21).

element	primary recrystallization		2nd phase in eutectic melt	
	wt.%	at.%	wt.%	at.%
U	70	21	0	0
Zr	14	11	9	3
Fe	1	< 2	24	13
Cr	< 1	< 1	22	12
Ni	< 0.1	0	6	3
Al	0	0	8	9
O	15	66	31	59
phases	$U_{0.63}Zr_{0.33}Fe_{0.04}O_2$ CaF_2 type		$Fe(Cr,Ni,Zr)_{1.3}Al_{0.7}O_4$ FeM_2O_4 spinel type	
lattice parameters	a = (539.8 ± 0.5) pm a = (531.7 ± 0.3) pm		-	

$Fe(Cr,Ni,Zr)_{1.3}Al_{0.7}O_4$. The given composition of the CaF_2 type structure is fortuitous in this region and fluctuates in other areas.

The X-ray diffraction analysis covers a larger area of the sample. A bimodal shape of each diffraction line was detected. The respective maxima result in two lattice parameters, a = (539.8 ± 0.5) pm and a = (531.7 ± 0.3) pm, for the suggested $(U,Zr)O_2$ phase regions which have a different brightness in the α autoradiograph (fig. 25). The compositions can be deduced from fig. H of the appendix which would lead to $U_{0.80}Zr_{0.20}O_2$ and $U_{0.57}Zr_{0.43}O_2$, the former phase in abundance. The $U_{1-x}Zr_xO_2$ solid solutions and the spinel phase were formed via the liquid state. However, the movement of this material to the lower plenum could be effected by a solid-liquid two-phase mass transport, the liquid spinel being the lubricant.

e. Lower plenum core debris rock 11-7, section A

Section A of the lower plenum core debris rock 11-7 was repolished at KfK and was prepared as sample 0 for X-ray diffraction. The light-optical microstructure and a detail are represented in fig. 28. The sample seemed not to be gainful for X-ray microanalysis because the microstructure is very similar to that of sample 11-5-A in fig. 24. However, part of sample 11-7-A was prepared for scanning electron microscopy and X-ray diffraction. The secondary electron and absorbed electron images are illustrated in fig. 29. Two phases can be distinguished in the X-ray diffraction pattern which yield a = (543.3 ± 0.2) pm for the CaF_2-type structure (see table 14) and a' = (513.3 ± 0.2) pm and c = (522.1 ± 0.2) pm for the tetragonal phase (see table 15) and are attributed to cubic $(U,Zr)O_2$ and tetragonal $(Zr,U)O_2$. The lattice parameters of the UO_2-ZrO_2 system in fig. H of the appendix indicate that the compositions are c-$U_{0.90}Zr_{0.10}O_2$ and t-$Zr_{0.86}U_{0.14}O_2$ if no further cations are dissolved in the lattice. However, EDX analysis elucidate the presence of very small amounts of chromium and iron in both the phases. They are nearly not discernible in the light-optical microstructure. It can be inferred from the phase diagram of the UO_2-ZrO_2 system in fig. G of the appendix that the material had a temperature of about 2700 °C for a short time. The phase diagram suggests further a long-time thermal arrest at 1600 °C because the compositions of c-$(U,Zr)O_2$ and t-$(Zr,U)O_2$ correspond to the positions of the solvus lines at this temperature. The light-optical microstructure detail in fig. 28 and the electron-optical images in fig. 29 point to a further phase in the grain boundaries of the c-$(U,Zr)O_2$ particles. The EDX analysis evidenced the presence of aluminium in this area. It is indeed a c-$(U,Zr)O_2$-spinel eutectic as it was found already in sample 11-5-A. One diffraction peak was left in the X-ray diffraction pattern at $2\theta = 36.05°$ which is attributed to

the most intensive (113) reflex of the $Fe(Al,Cr,Ni,Zr)_2O_4$ phase yielding a = 826.3 pm. This lattice parameter is between a = 813.5 pm and a = 836.1 pm of the end members $FeAl_2O_4$ and $FeCr_2O_4$, resp., of the continuous series of the $Fe(Al,Cr)_2O_4$ solid solutions. The relevant homogeneity range results from the isothermal section of the Al_2O_3-Cr_2O_3-FeO system at 1760 °C in fig. I of the appendix.

Table 14: X-ray diffraction pattern of the cubic $(U,Zr)O_2$ phase of sample 0, section A of lower plenum core debris rock 11-7 (Cu Kα).

2θ	d in pm	hkl	a in pm	
28.39	314.4	111	(544.5)	
32.96	271.7	200	543.5	
47.32	192.1	220	543.3	
56.14	163.8	311	543.4	
58.90	156.8	220	543.1	$\bar{a}$ = (543.3 ± 0.2) pm
69.17	135.8	400	543.2	
76.42	124.6	331	543.2	
78.74	121.5	420	543.5	
88.06	110.9	422	543.4	

Table 15: X-ray diffraction pattern of the tetragonal $(Zr,U)O_2$ phase of sample 0, section A of lower plenum core debris rock 11-7 (Cu Kα).

2θ	d in pm	hkl	lattice parameters
30.00	297.8	101	a = (362.9 ± 0.1) pm
34.35	261.0	002	$a' = a\sqrt{2}$ = (513.3 ± 0.2) pm
34.96	256.6	110	c = (522.1 ± 0.2) pm
49.8	183	112	

f. Previously molten rock O7-P3-1

The previously molten rock contains mainly ceramic material and is located in between the upper and the lower crust of the core material. A view of sample O7-P3 in the as-received state is illustrated in fig. 30. A piece was cut-off and was prepared as sample O7-P3-1 for X-ray microanalysis. The microstructure and the long-time exposed α autoradiograph (2 hours) are shown in fig. 31. The frames in the microstructure marked by 1, 2 and 3 characterize the positions of the X-ray microanalysis. Three types of metallic and three types of ceramic phases can be distinguished in the microstructure and in the element distribution images in fig. 32, 33 and 34 which refer to the positions 1, 2 and 3, resp. The qualitative analysis can be quantified on the basis of the results of the preceding analysis. Two immiscible metallic regions were observed: a chromium depleted Fe-Ni steel phase and the absorber material Ag(In,Cd,Sn) in which the $(Ni,Fe)_3(Sn,In)_2$ phase is precipitated dendritically during cooling. Ni_3Sn_2 melts congruently at 1264 °C. The ceramic phases are composed of $(U,Zr)O_2$, Fe oxide and Al-Cr-Fe-Zr oxide which both have probably a spinel type structure.

The quantitative analysis of the three metallic phases is compiled in table 16. The austenitic steel matrix appears grey in the unetched microstructure. It is enriched in nickel; tin and molybdenum are present, chromium is absent (pos. 3 in fig. 32). The β-γ autoradiography of this area indicates already a β-γ active nuclide which was identified by X-ray microanalysis to be ruthenium (Ru-106); up to 0.9 wt.% Ru was found in the steel matrix. The surface is nickel enriched up to 52 wt.% Ni; the concentrations of tin and ruthenium are decreased (pos. 4 in fig. 32). The second metallic matrix appears yellow in the unetched surface and is composed of the absorber material components silver, indium, cadmium with the initial concentration ratios, but with about 10 % tin added. According to the monotectic silver-steel system some tenths of steel components are dissolved in silver (pos. 1 in fig. 32). Antimony could be identified just above the X-ray intensity background which corresponds to less than 0.01 % Sb and is reason for the active areas in the β-γ autoradiograph. The intermetallic compound $(Sn,In)_2(Ni,Fe)_3$ is precipitated in the silver matrix (pos. 2 in fig. 32). It is noteworthing that the concentration of the volatile cadmium is higher in this region within the crust region than in the crust itself. Ruthenium was observed in the austenitic steel phases, however, in higher concentrations in this region than in the crust.

Table 16: Quantitative analysis of metallic phases in position 1 of previoulsy molten rock O7-P3, section 1, fig. 32.

position	element	conc. in wt.%	conc. in at.%	phase
1 yellow matrix	Ag In Cd Sn Ni Fe Mo Sb Ru	75 - 78 9 - 11 3 10 - 11 0.04 ≤ 0.06 ≤ 0.08 > 0 0	76 - 79 9 - 11 2.8 - 3.2 9 - 10 0.08 ≤ 0.1 ≤ 0.09 > 0 0	α-Ag (In, Sn)
2 dendrites	Sn In Ag Ni Fe Ru Sb	52.7 3.4 0.5 41.6 1.7 0.1 0	36.5 2.5 0.4 58.1 2.5 0.1 0	$(Sn,In)_2(Ni,Fe)_3$
3 light grey matrix	Fe Ni Sn Mo Ag In Ru	61.4 31.4 3.4 2.8 0.03 0.02 0.9	64.6 31.4 1.7 1.7 0.02 0.01 0.6	γ-Fe(Ni)
4 Ni enriched steel matrix	Ni Fe Mo Sn In Ru	52 45 3.1 0 0.2 0.1	51 47 1.9 0 0.1 0.07	Ni(Fe) from Inconel

Table 17: Quantitative analysis of oxide phases in positions 2 and 3 of previoulsy molten rock O7-P3, section 1, fig. 33 and 34.

position	element	conc. in wt.%	conc. in at.%	phase
5	Fe Al Cr Zr O	62.5 1.5 1.0 6.3 28.8	36.6 1.8 0.6 2.3 58.8	$(Fe,M)_3O_4$
6	Fe Cr Al Zr O	31.4 30.1 7.2 1.1 30.2	17.0 17.5 8.1 0.35 ≈ 57	FeM_2O_4
7	U Zr O	64 20 16*	18 15 67*	$U_{0.55}Zr_{0.45}O_2$
8	U Zr O	83 4 13*	29 4 67*	$U_{0.88}Zr_{0.12}O_2$
9	U Zr O	84 3 13*	30 3 67*	$U_{0.90}Zr_{0.10}O_2$

* rest

The quantitative analysis of the oxides is compiled in table 17. The phases are $(U,Zr)O_2$ with different U/Zr ratios (pos. 5 and 6 in fig. 33 and 34) and FeM_2O_4 spinels with M = Fe, Cr, Zr, Al (pos. 7 to 9 in fig. 33). The oxygen analysis was difficult and therefore not very reliable due to the tiny precipitates. The character of the microstructure of the $(U,Zr)O_2$-spinel system is eutectic with $(U,Zr)O_2$ primary crystals which decompose into two $(U,Zr)O_2$ phases during further cooling.

g. Loose core debris O7-P8, section B

The loose core debris is located between the core cavity and the upper crust (see fig. 1). The microstructure of the selected section B is illustrated in fig. 35. The congruent α autoradiograph (exposure time 3 hours) of this section is given in fig. 36. These two figures are characterized by α free grey stripes which are identified as isolated oxidized Zircaloy sheets, 150 µm in thickness. Further, rectangular zirconium oxide phases contain uranium in low concentrations. Higher uranium containing phases are associated with metallic phases which are in most cases silver absorber material. Light-optical and electron optical microstructural details as well as element distribution images are given in fig. 37 to 42. The compositions of the phases are semi-quantitatively compiled in the following:

1. α-Ag(In,Cd,Sn), metallic absorber
2. $(Sn,In)_2(Ni,Fe)_3$, precipitates in the silver matrix
3. ZrO_2, uranium free, tin depleted
4. $(Zr,U)O_2$ with 2 mol% UO_2
5. Fe-Cr-Zr oxide, aluminium free
6. $U(Zr)O_2$, sharp edges ,less than 15 µm in diameter

The silver matrix and the $(U,Zr)O_2$ phase have a very fine two-phase structure as it can be seen from the overmodulated secondary image (SEI) in fig. 42. A quantitative analysis was not possible. The less pronounced crystalline state and the partly unmolten structure of the phases are indicators for a lower temperature in the loose core debris than in the region within the crust.

5. Discussion

The approach is the understanding of the sequence of the reactions of the different core materials during the temperature increase of the reactor core and the contribution of oxygen which is available by water vapour reactions in a later stage. The different core material reactions are summarized in table 18.

It has been shown by metallography that the main constituents of the so-called upper and lower crust, each about 10 cm in thickness, are metallic phases (samples D8-P1-A and K9-P1-F) whereas the inner region is ceramic with low fractions of metallic material (O7-P3-1). The first local reaction can take place between Inconel, steel and Zircaloy above the lowest multi-component eutectic temperature near the Zr apex at about 930 °C to give an Fe-Cr-Ni-Zr-Sn melt. However, the rate of liquefaction is hindered by superficial ZrO_2 layers and by an instantaneous $Zr(Fe,Cr,Ni)_2$ phase formation (congruent melting point 1675 °C). Hence, the $Zr(Fe,Cr,Ni)_2$-steel eutectic at about 1200 °C is of relevance for the further liquefaction process. It is further continued by the monotectic reaction of solid steel with the liquid absorber at 1435 °C. There is rather good compatibility between steel and absorber below the monotectic temperature if no premature steel-Zircaloy guide tube interaction occurs in the absorber pins. Some percent nickel are dissolved in the liquid absorber. The metallic hexagonal Mo-Tc-Ru-Rh-Pd fission product inclusions are dissolved in the steel above the solidus temperature at 1433 °C. An exchange reaction of Sn occurs between the metallic melts. This element originally dissolved in liquid steel-Zircaloy is changed predominantly to the absorber melt. During cooling, Ni and part of Sn are precipitated as $Ni_3(Sn,In)_2$ dendrites within or on the surface of the absorber surface at 1264 °C. Ag-Zr alloys were not observed.

A second principal reaction starts at about 1300 °C by dissolution of UO_2 in the steel-Zircaloy eutectic. The liquid is formed first at the interface between UO_2 and steel-Zircaloy. UO_2 is largely dissolved at 1900 °C by formation of an oxygen containing steel-Zircaloy-uranium melt. The Zr rich melt of the UO_2-Zr system does not pass a phase field where primary UO_2 crystallization occurs on cooling. The presence of Fe in the melt makes possible the existence of a $U(M)O_2$ phase field in the total concentration region and, hence, $U(M)O_2$ primary recrystallization. Quadratic UO_2 particles containing about 9 mol% ZrO_2 are reprecipitated during cooling of the oxygen containing steel-Zircaloy-uranium melt below 2200 °C by passing the liquidus surface. The remaining steel-Zircaloy is oxygen depleted. The oxygen content in the Zr-steel melt is low because the affinity between oxygen and zirconium is diminished due to the presence of steel components. At lower temperatures the Laves phase $Zr(Fe,Cr,Ni)_2$ with a melting point at 1675 °C is precipitated. Finally $Zr_2(Fe,Cr,Ni)$ and zirconium are precipitated, the latter containing minor amounts of nickel and absorber material.

In a later stage (reflood phase 3 after 3 hours), the surface oxidation of the $Zr_2(Fe,Cr,Ni)$ phases is initiated by the reaction with water. As a consequence, the

Table 18: TMI-2 core material reaction schemes. The given temperatures are based on the thermodynamic equilibria irrespective of the kinetics of the reactions which are enhanced at higher temperatures.

Type A melting reactions	
<absorber> = {Ag,In,Cd}	T_{sol} = 760 °C
<Inconel,steel> + <Zry> = {Fe,Cr,Ni,Zr,Sn}	$T_{eut} \cong$ 1200 °C*
<steel> + {absorber} = {Fe,Cr,Ni} + {Ag,In,Cd}	T_{mon} = 1435 °C
<steel> + <Mo,Tc,Ru,Rh,Pd> = {Fe,Ru,...}	T_{sol} = 1433 °C
Exchange reaction in the liquid	
{Fe,Cr,Ni,Zr,Sn} + {Ag,In,Cd} = {Fe,Cr,Ni,Zr} + {Ag,In,Ni,Sn} + (Cd)	T > 1435 °C
Side reaction during cooling	
{Ag,In,Ni,Sn} = {Ag,In,Sn} + <Ni_3Sn_2>	T_m = 1264 °C
Type B melting reactions	
{Fe,Cr,Ni,Zr} + <UO_2> = {Fe,Cr,Ni,Zr,U,O}	T ≥ 1300 °C
Main metallic reactions during cooling (St = Fe,Cr,Ni)	
{Fe,Cr,Ni,Zr,U,O} = <$U(Zr)O_2$> + {St,Zr; U,O depleted}	T < 2200 °C
{St,Zr; U,O depleted} = {St,Zr,U,O} + <$ZrSt_2$>	T_m = 1675 °C
{St,Zr,U,O} = <$U(Zr)O_2$> + <$StZr_2O_x$>	T ≥ 1600 °C
Type C melting reactions	
<UO_2> + <ZrO_2> → <$(U,Zr)O_2$> = {$(U,Zr)O_2$}	T_m = 2550 °C
<Al_2O_3> + <Zr> = {Zr,Al,O}	T_{eut} ≥ 1350 °C
<$FeAl_2O_4$> = {$FeAl_2O_4$}	T_m = 1770 °C
<$FeCr_2O_4$> = {$FeCr_2O_4$}	T_m = 2150 °C
Main ceramic reactions during cooling	
{$(U,Zr)O_2$} = <$(U,Zr)O_2$>	T_{sol} ≥ 2550 °C
<$(U,Zr)O_2$> = <$U(Zr)O_2$> + <$Zr(U)O_2$>	T ≥ 1600 °C
{U,Zr,Al,Fe,Cr,O} = <$(U,Zr)O_2$> + <$Fe(Al,Cr,Zr)_2O_4$>	T_{eut} = 1500 °C
Oxidation at higher oxygen potentials	
<$StZr_2O_x$> + O_2 = <St_3Zr_3O>	

* a further invariant point in the pseudo-ternary exists at 930 °C which may give rise to local liquefaction; it is masked by fast $Zr(Fe,Cr,Ni)_2$ Laves phase formation.

grain boundaries and the grain surfaces are oxidized up to the composition $Zr_2(Fe,Cr,Ni)O_{0.3}$ which corresponds to the known η-Zr_6Fe_3O phase. Some of the

β-Zr(Fe) which did not form an intermetallic compound with steel components in the first stage is oxidized to monoclinic $Zr(Fe)O_2$. The fraction of the binary oxides FeO and Cr_2O_3 is low.

A third, locally separated reaction sequence is the formation of a $(U,Zr)O_2$ melt which requires temperatures above 2550 °C. However, it is not clear at the moment whether other ceramic phases will decrease this temperature limit, see table 18. However, the formation of the solid solution is possible in the solid state. The Zircaloy cladded burnable poison Al_2O_3-B_4C starts to react to a liquid at about 1350 °C [1]. Further, the spinels $FeAl_2O_4$ and $FeCr_2O_4$ which are formed from the binary oxides melt congruently at 1770 °C and 2150 °C, resp. The cooling period is characterized by two reactions. The decomposition of $(U,Zr)O_2$ into two phases $U(Zr)O_2$ and $Zr(U)O_2$ occurs at about 1600 °C during a long-time thermal arrest because the observed uranium and zirconium solubilities of the two conjugate phases correspond to this temperature according to the phase diagram of the UO_2-ZrO_2 system. A second reaction within this sequence is a eutectic solidification of the U-Zr-Al-Fe-Cr-O melt to $U(Zr)O_2$ primary crystals and an $Fe(Al,Cr,Ni,Zr)_2O_4$ spinel with a eutectic temperature at about 1500 °C. This melt can be responsible for a two-phase solid-liquid mass transport above this temperature, the liquid spinel phase acting as the lubricant (see samples 11-5-A and 11-7-A). Further phase studies in these systems will elucidate the phenomenon which could be responsible for the presence of the high amounts of $(U,Zr)O_2$ in the lower plenum.

6. Reactions and phases observed by other authors

Samples from the damaged TMI-2 reactor core were analyzed also by other laboratories, the results were published in Nuclear Technology [2] and were presented at the CNSI TMI-2 Sample Examination Group Meeting, Tokyo, 1990 [3]. In most cases, there is full agreement between their results and those presented in this report. However, some of their results are singularities or violate the phase rule or the principles of the heterogeneous equilibria.

UO_2 and ZrO_2 form a continuous series of a solid solution with a congruent melting point minimum, the tangents on the solidus and the liquidus in this point are horizontal. The system is not a eutectic one. A second, tetragonal phase is precipitated from the cubic solid solution with decreasing temperatures by crossing the solvus line of the solid solution region.

Ag and Zr do not form a eutectic system. There is a degenerate eutectic on the Ag side with no considerable temperature decrease. On the Zr side $AgZr_2$ is observed

which has a peritectic melting point at 1191 °C. Binary Ag-Zr phases were not observed in the present investigation.

Provided the temperatures are high enough, Al_2O_3 does not exist in an isolated state. Eutectic Al_2O_3-ZrO_2 formation (T_e = 1710 °C) is unlikely. Al_2O_3 reacts with other oxides to multi-component spinels.

Cd-U phases were not observed in the present investigation. UCd_{11} is the only compound in this system and decomposes peritectically at 473 °C. The heat of formation ${}^f\Delta H°$ = - 5 kJ/g-atom makes the reaction unlikely in the reactor core.

An increase of the O/U ratio of the fuel, i.e. an oxdiation was suggested from the lattice parameter measurements. However, the UO_2 lattice contraction should be correlated with the observed dissolution of the oxides of Zr, Fe and Cr in the UO_2 lattice. 1 at.% ZrO_2 dissolved in UO_2 corresponds to a lattice parameter decrease Δa = - 0.34 pm. An oxidation of the fuel was not observed. Gravimetric O/M ratio measurements of UO_2 fragments gave values ranging from 1.998 to 2.009 [4].

The chemical potential of oxygen in the damaged reactor core was estimated on the basis of the oxidation state of the components: $\Delta\bar{G}_{O_2}$ = - 500 kJ/mol at 1473 K and $\Delta\bar{G}_{O_2}$ = - 150 kJ/mol at 2273 K. This would result in oxygen partial pressures of $p_{O_2} = 10^{-18}$ bar and $p_{O_2} = 10^{-4}$ bar and water/hydrogen ratios p_{H_2O}/p_{H_2} = 0.01 and p_{H_2O}/p_{H_2} = 12 at 1473 K and 2273 K, resp. The steep oxygen concentration gradients should have become equalized across the damaged reactor core after some time.

7. Conclusions

a. The first local core melting can happen between the Zircaloy and steel/Inconel interface at 930 °C; this is the eutectic temperature between Zircaloy and the high melting intermetallic phase $ZrSt_2$ (St = Fe, Cr, Ni). However, the formed liquid interface is instantaneously consumed for the $ZrSt_2$ formation. The second eutectic appears on the steel side between $ZrSt_2$ and steel/Inconel at about 1200 °C. This is the relevant temperature of enhanced melting of the metallic core materials. The dissolution of UO_2 in the metallic Zr-Fe-Cr-Ni melt is possible at 1300 °C with an increased rate above 1900 °C. The absorber material with the initial composition 81 at.% Ag - 14 at.% In - 5 at.% Cd and the solidus temperature 760 °C forms a monotectic with steel at about 1435 °C. Hence, two free flowing metallic melts exist above this temperatures. The fraction of the absorber material phase decreases by evaporation with increasing temperatures. The liquid ceramic

with other oxides, e.g. with Al_2O_3, CrO_2, FeO_x, $Fe(Al,Cr,Ni,Zr)_2O_4$ far below this temperature.

b. The metallic phases were observed mainly in the lower crust and to minor extent in the hotter upper crust. These phases are resolidified Cd depleted α-Ag absorber material as well as $ZrSt_2$ and Zr_2StO_x ($x < 0.3$, St = Fe, Cr, Ni) from the Zircaloy-Inconel-steel melt. The observed phases contain nearly no oxygen by reason of the reduced affinity of Zr to this element in the presence of the steel components in the liquid Zr-steel phase.

c. The dominant phases in the core centre were observed as $(U,Zr)O_2$, c-$U(Zr)O_2$ and t-$Zr(U)O_2$. A cubic $(U,Zr)O_2$ solid solution can occur by direct solid UO_2-ZrO_2 interdiffusion. However, an increase above the melting temperature minimum of this solid solution at 2550 °C is probable. In the cooling period, a high fraction remained cubic by quenching; a longer thermal arrest appeared in the reactor core centre within the crust at about 1600 °C because the composition of the observed two conjugate phases c-$(U,Zr)O_2$ and t-$(Zr,U)O_2$ correspond to this temperature. Monoclinic ZrO_2 is formed by direct oxidation of Zircaloy which had not reacted with UO_2 in the liquid.

d. The precipitation of square $U(Zr)O_2$ particles from the Zr-steel-U-O melt is made possible by the presence of steel in the liquid. The small UO_2 particles do not originate from mechanical fuel disruptions.

e. The solid Mo-Tc-Ru-Rh-Pd fission product phases are dissolved in the molten steel, antimony is probably dissolved in the absorber material after liquefaction. Hence, the thermodynamic activities and partial pressures, respectively, of the elements including their radioactive isotopes Mo-99, Tc-99, Rh-103, Ru-106 and Sb-125 are reduced in the light of source term considerations.

f. Some of the $(U,Zr)O_2$ material was transported down to the lower plenum. This is explained by the presence of the observed $Fe(Al,Cr,Ni,Zr)_2O_4$ spinel. The phases form a eutectic system. The spinel can act as the lubricant in the two-phase flow above the eutectic temperature of about 1500 °C.

References

[1] P. Hofmann, M. Markiewicz, J. Spino, J. Nucl. Mater. 166 (1989) 287

[2] Special issue of Nuclear Technology, vol. 87, August 1989

[3] D.W. Akers (Ed.), EGG-OECD-9168 (1990)

[4] A.J. Manley, S. Whillock, J.F.W. Thompson, R. Williamson, S.A. Beetham, in ref. [3]

Acknowledgements

The handling of the TMI-2 core material submitted to KfK was managed by the staff of the Hot Cells of the department HVT. Thanks are rendered to the head, Dipl.-Ing. H. Enderlein, and to his coworkers for the preparation of the samples used for density measurements, metallography, scanning electron microscopy, and X-ray diffraction. The X-ray microanalysis of the samples was performed by Mr. R. Fritzen and Mr. H.D. Gottschalg, IMF I. Many helpful discussions with Dr. P. Hofmann, IMF I, during the preparation of this report are gratefully acknowledged.

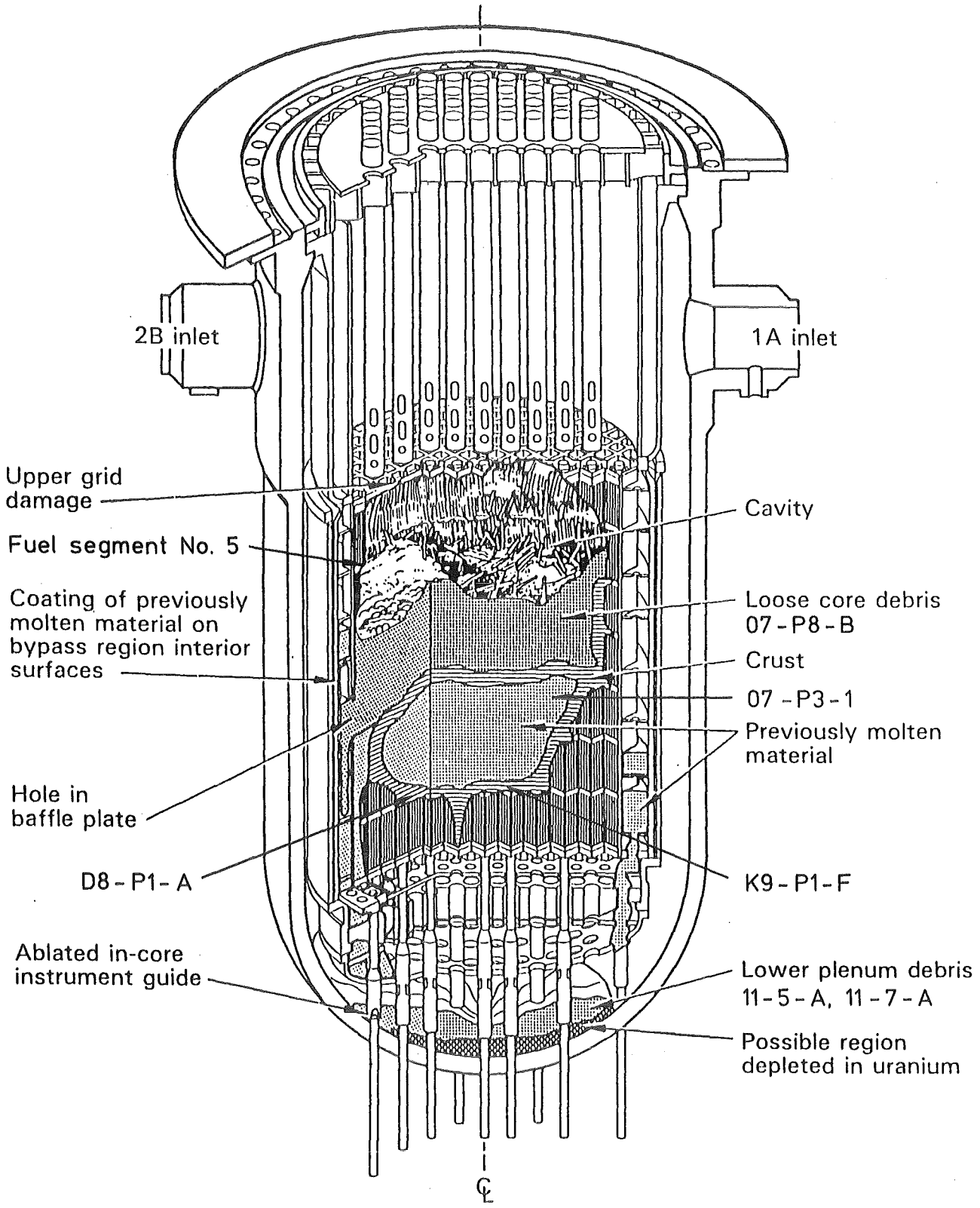

Fig. 1: TMI-2 end-state configuration and position of seven samples investigated by X-ray microanalysis and X-ray diffraction .

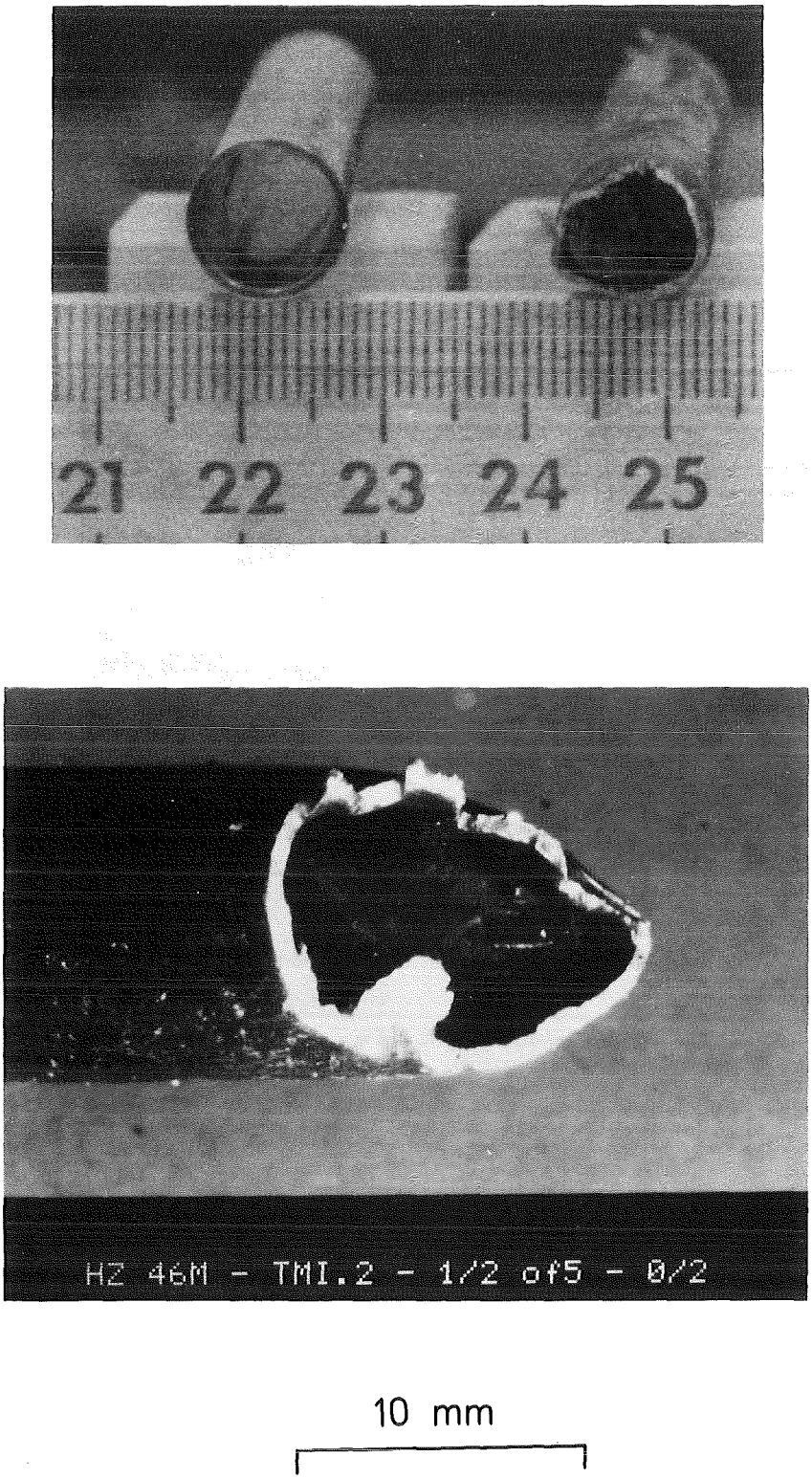

Fig. 2: View of fuel segment No. 5 from upper end of core position M2.

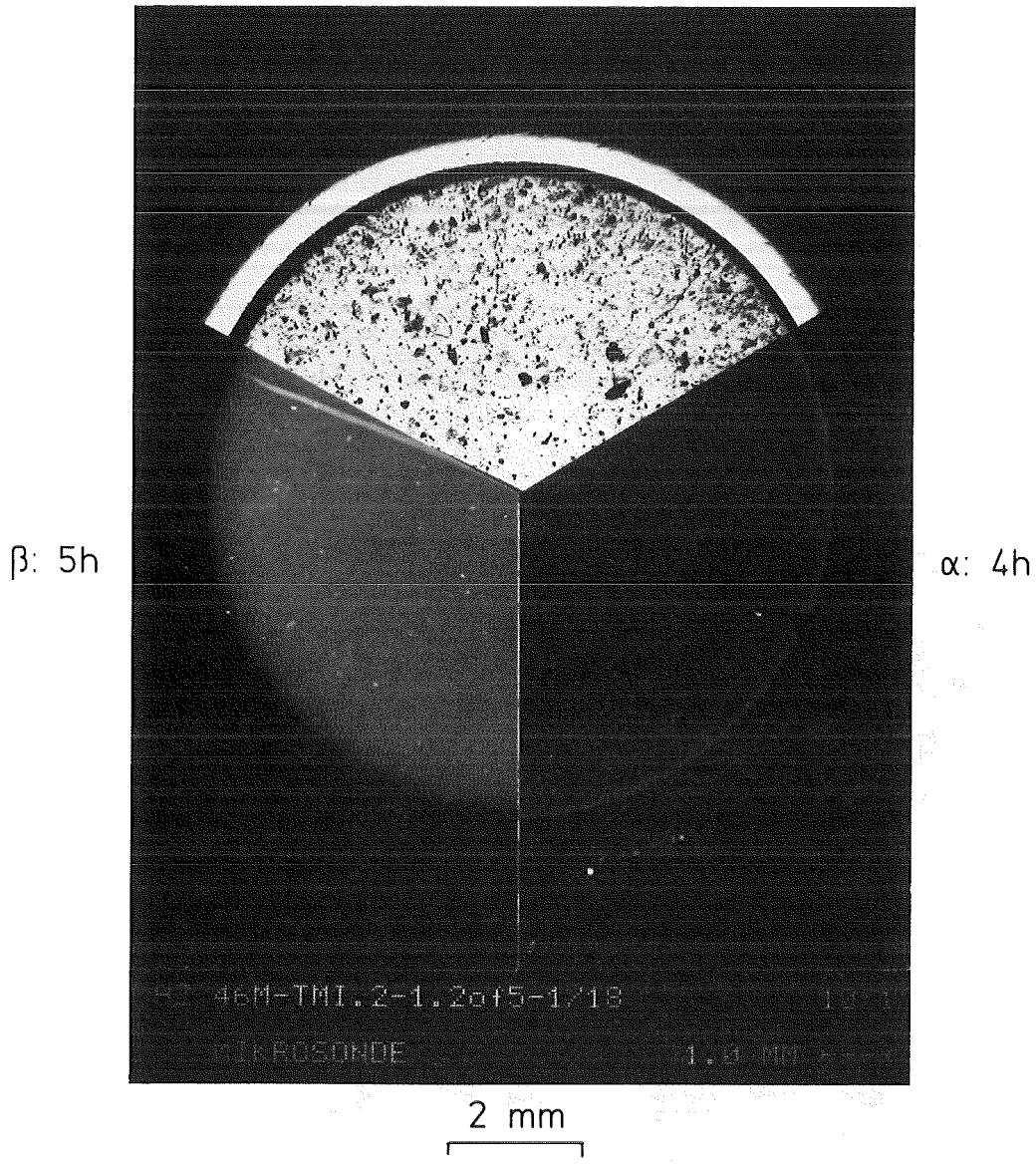

Fig. 3: Light-optical microstructure, α and β-γ autoradiographs (exposure time) of fuel segment No. 5, cross-section 1.

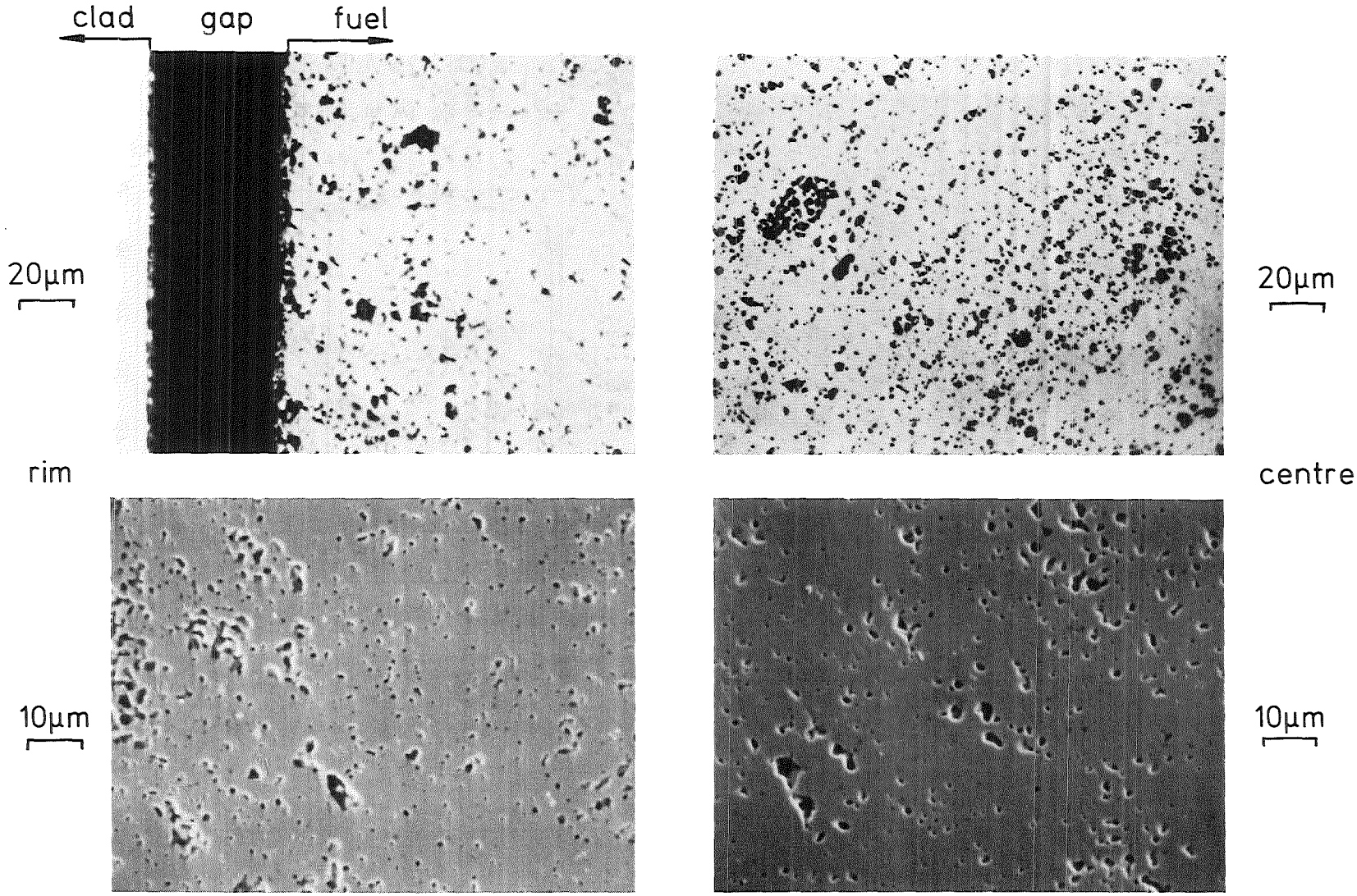

Fig. 4: Light-optical (top) and electron-optical microstructure (bottom) of the fuel centre (right) and the surface region (left) from fuel rod segment No. 5, cross-section 1.

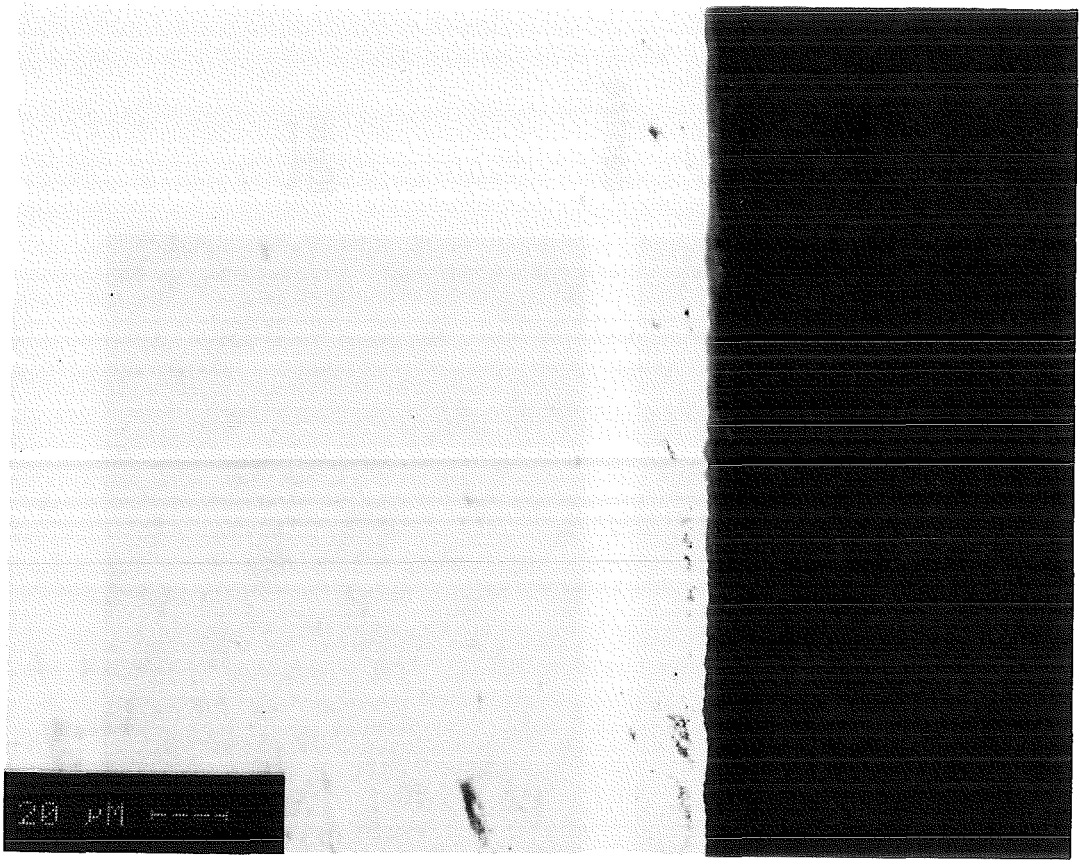

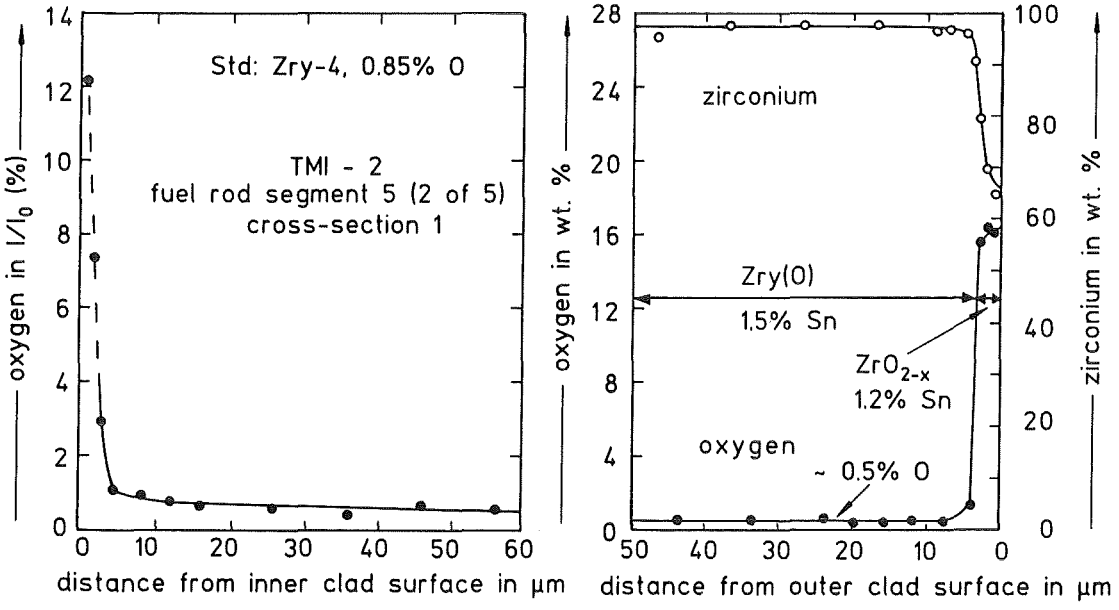

Fig. 5: Inner and outer Zircaloy-4 clad oxidation of fuel segment No. 5, cross-section 1; top: microstructure of the outer 4 µm oxide scale $Zr_{0.99}Sn_{0.01}O_{2-x}$.

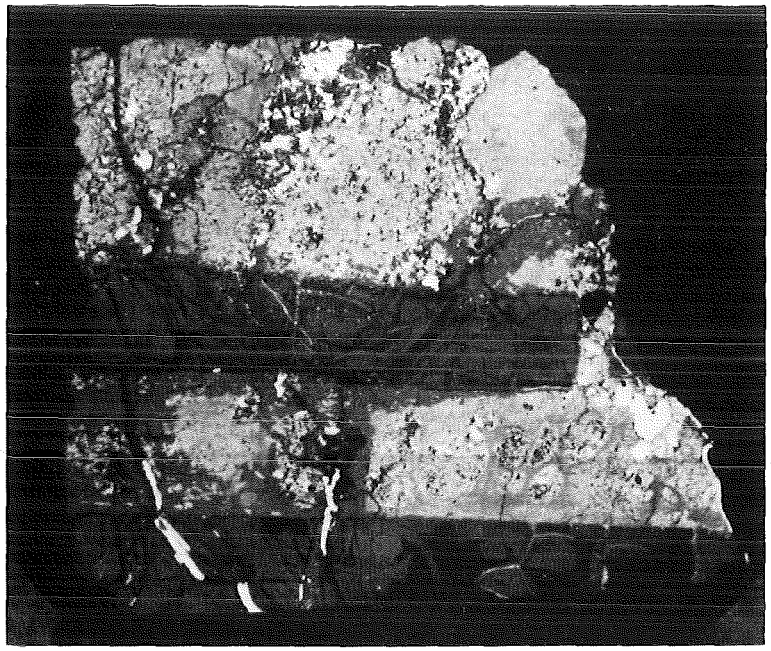

10 mm

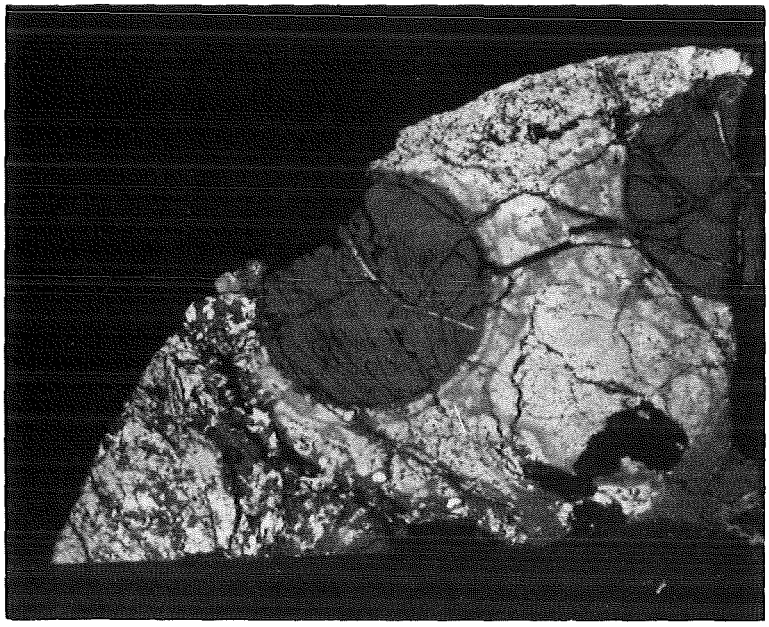

10 mm

Fig. 6: View of an axial and radial cut of core bore K9-P1, section F, lower crust region.

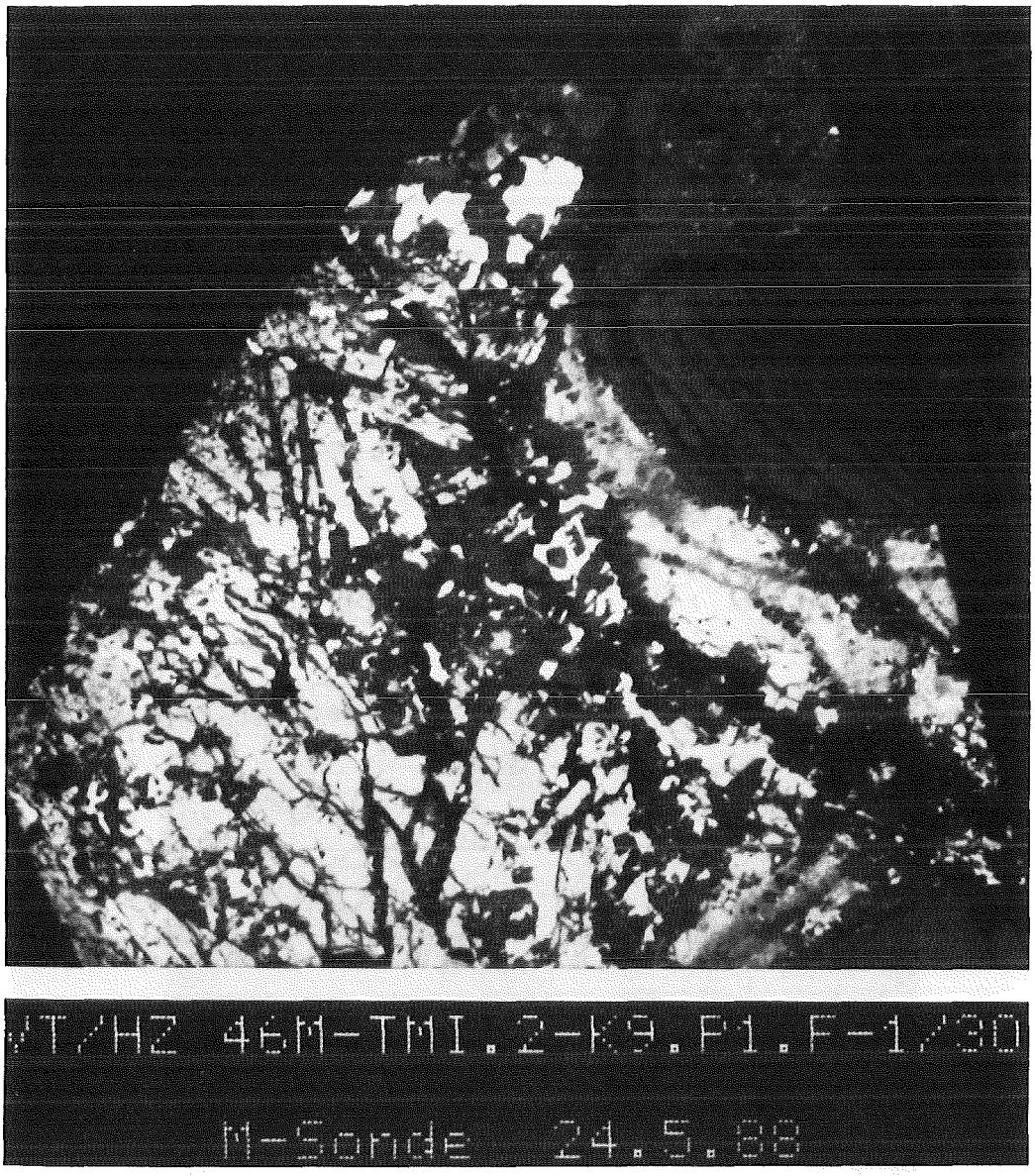

Fig. 7: Light-optical microstructure of core bore K9-P1, section F, sample 1 for X-ray microanalysis which originates from the left hand side of the radial section in fig. 6.

Fig. 8: α autoradiograph (2 h exposure time) of the sample in fig. 7.

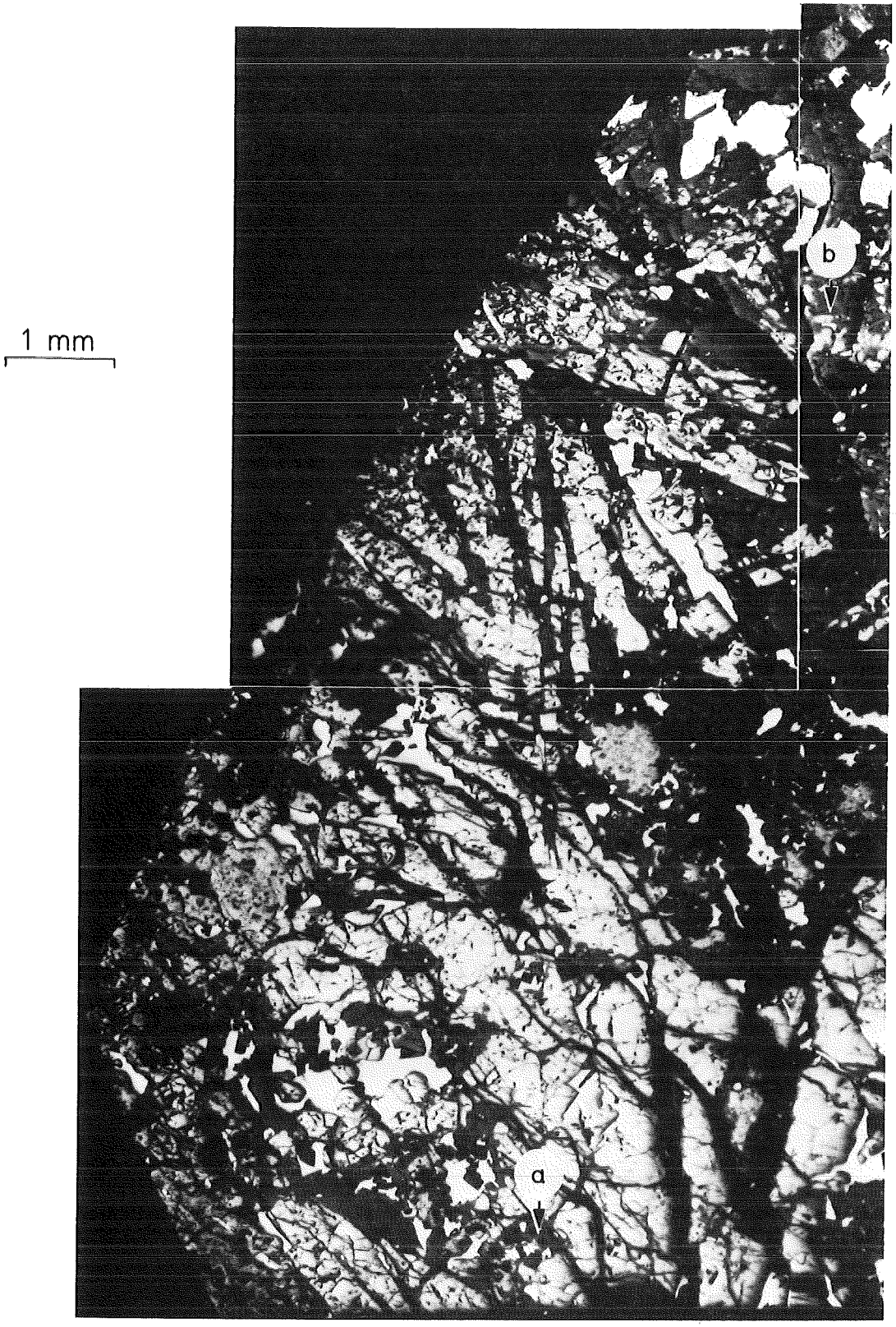

Fig. 9: Enlarged version of the light-optical microstructure of core bore K9-P1, section F, sample 1 in fig. 7; the arrows in the figure mark the positions a to d which were investigated by X-ray microanalysis.

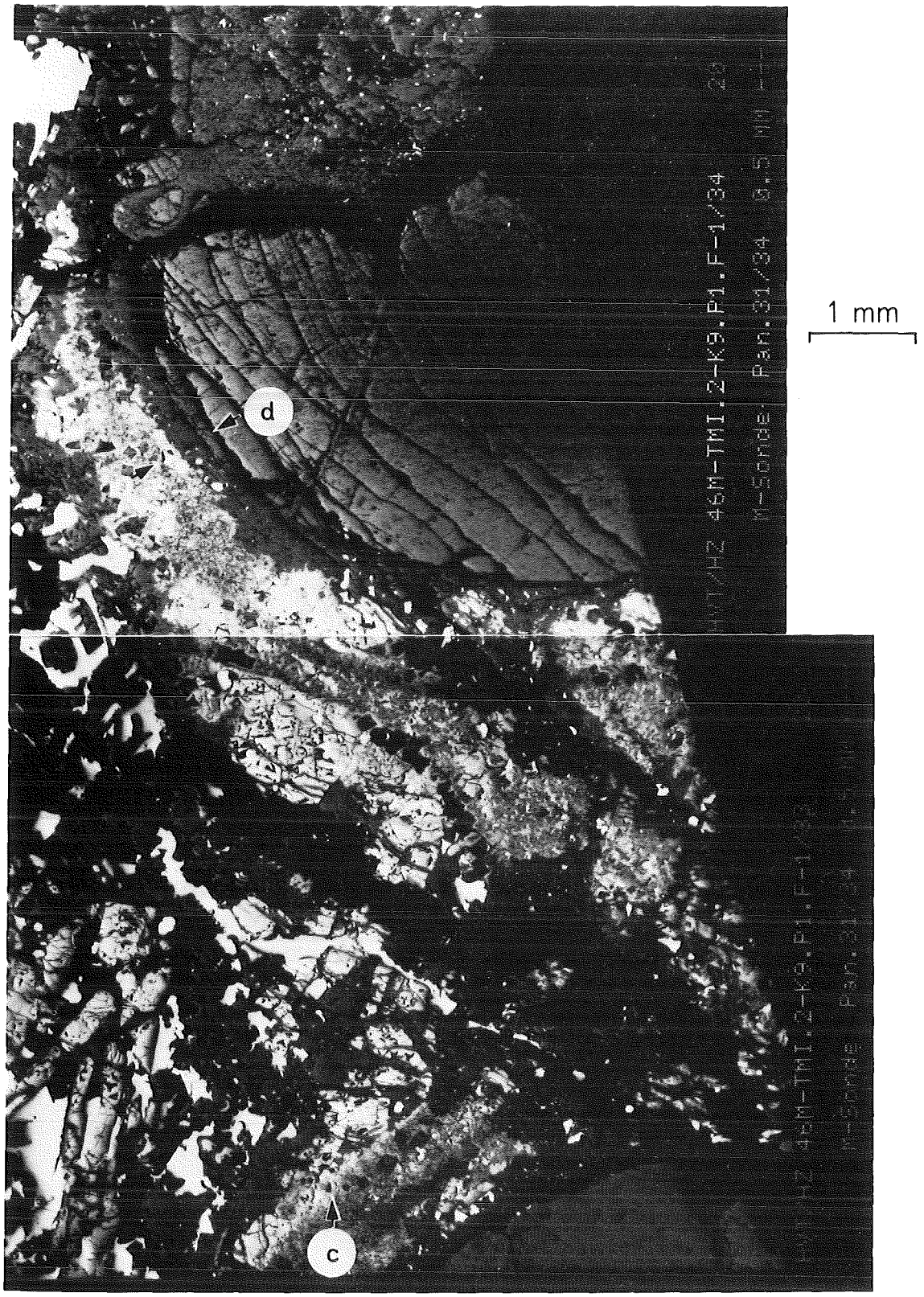

Fig. 9: continued: right hand side of the enlarged version of the light-optical microstructure in fig. 7.

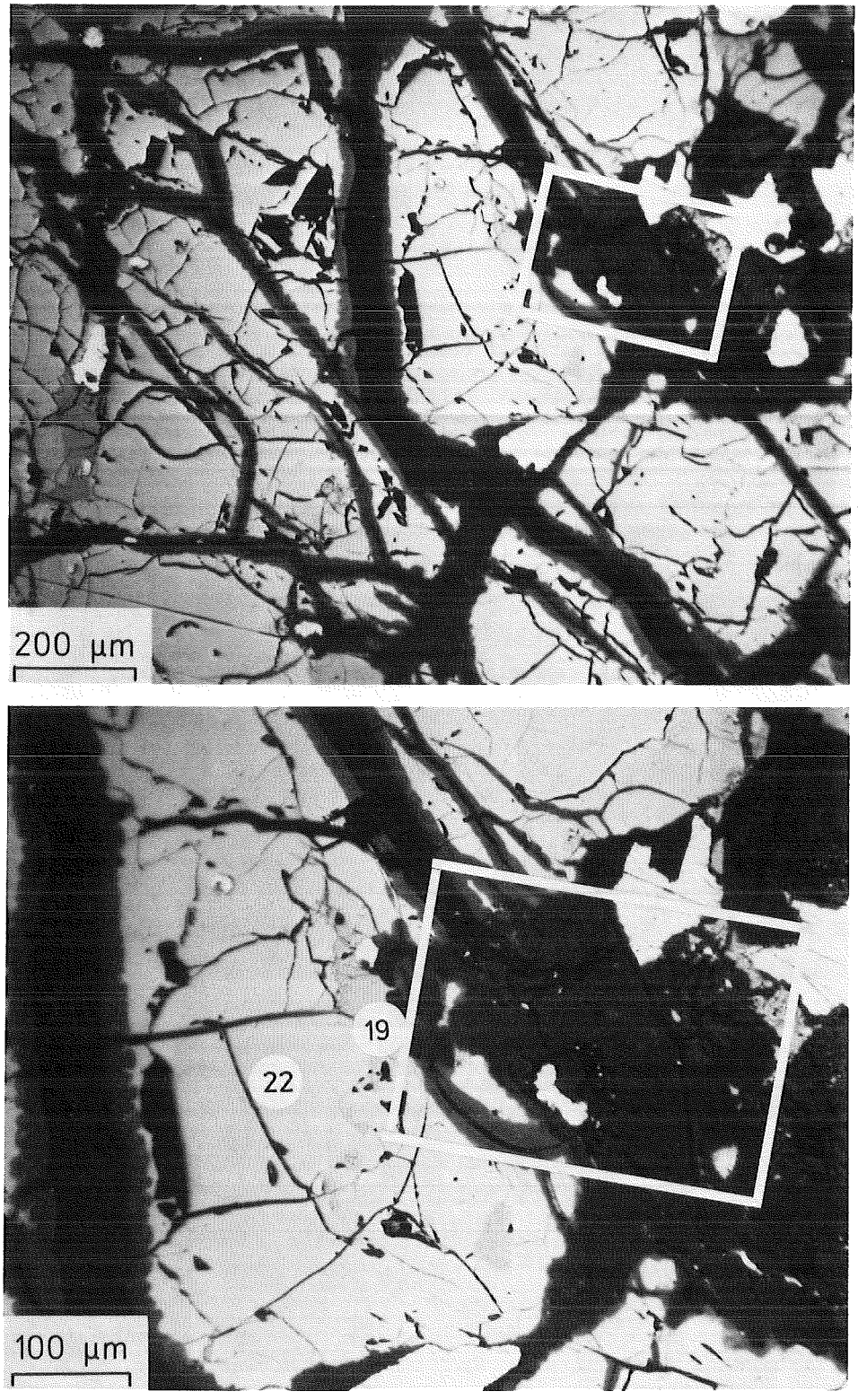

Fig. 10: Light-optical microstructure of core bore K9-P1, section F, sample 1, position a; the numbers refer to the quantitative analysis given in the tables; the frame refers to the section in fig. 11.

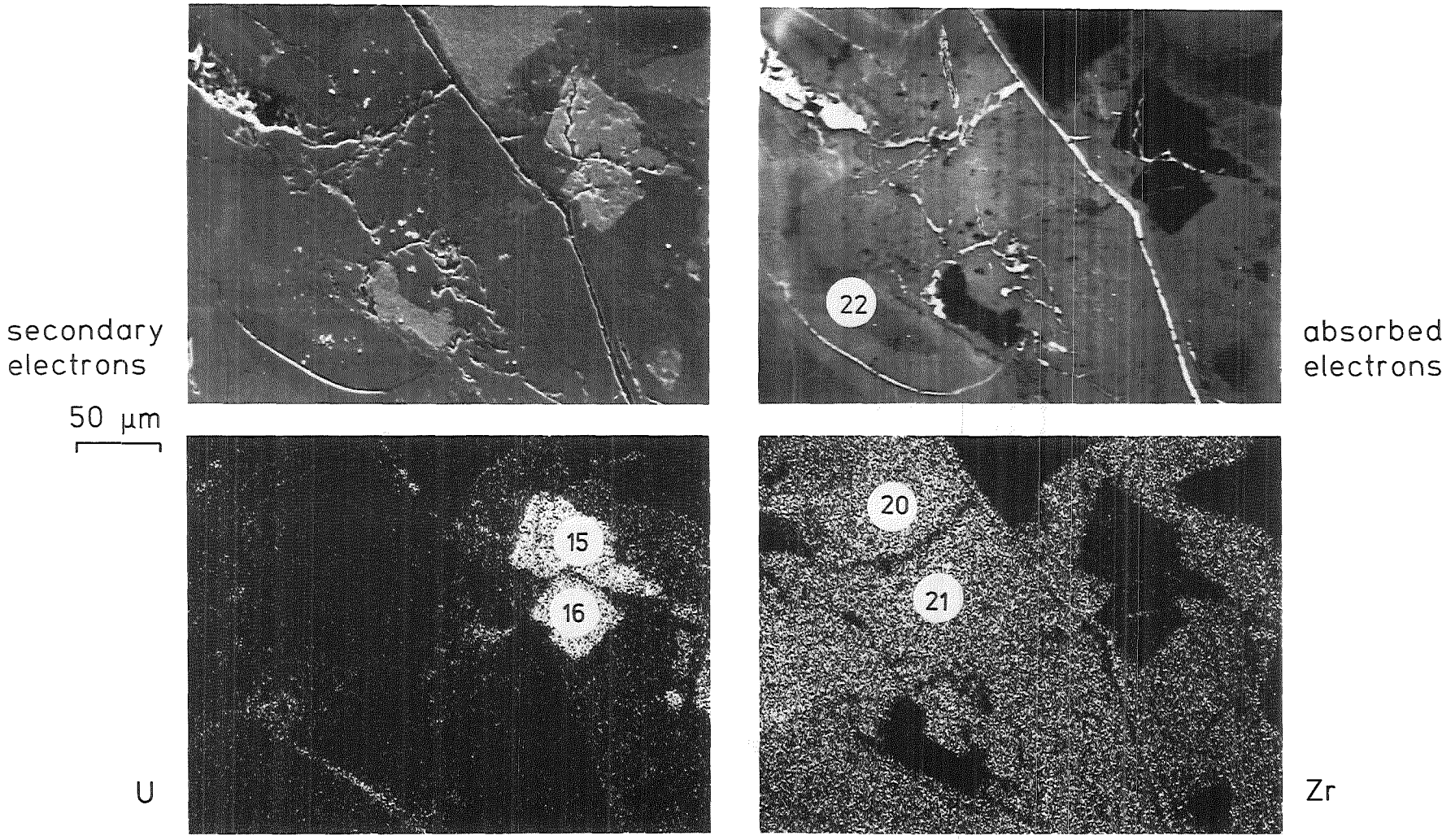

Fig. 11: Secondary electron image, absorbed electron image and element distribution of U, Zr, Fe, Cr, Ni, Sn, Ag, In, Al and O of core bore K9-P1, section F, sample 1, position a; the numbers refer to the quantitative analysis given in the tables.

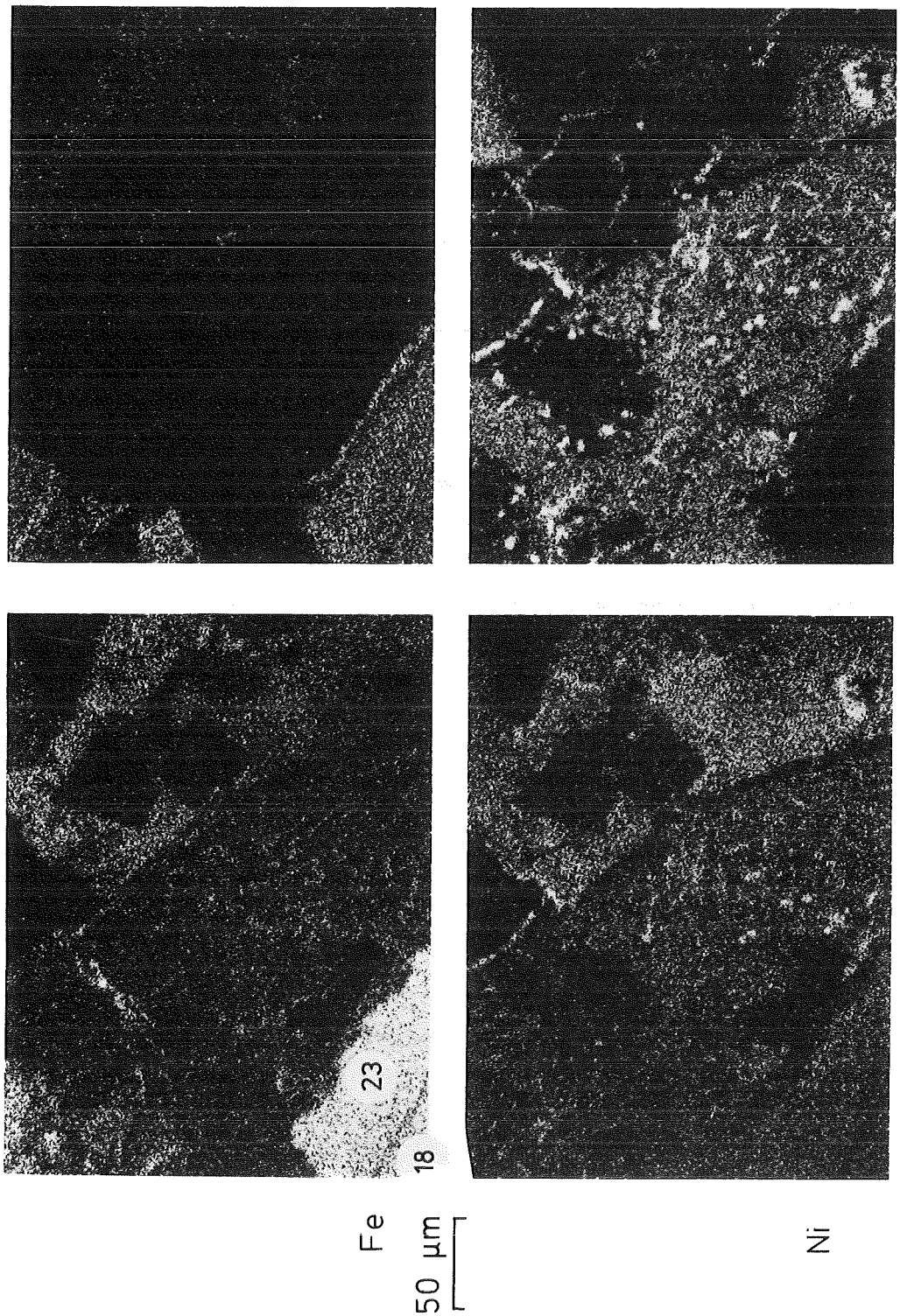

Fig. 11: continued.

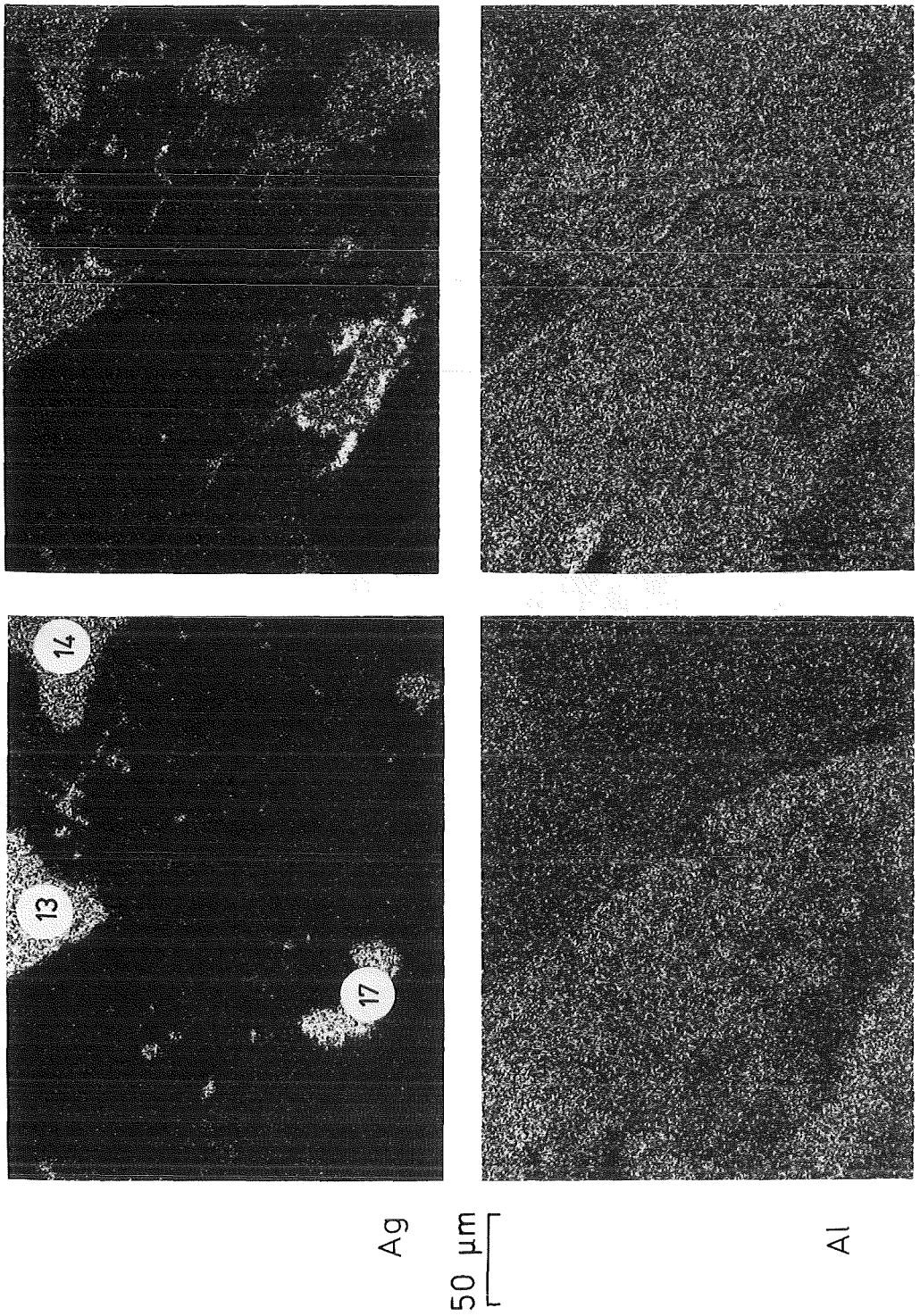

Fig. 11: continued.

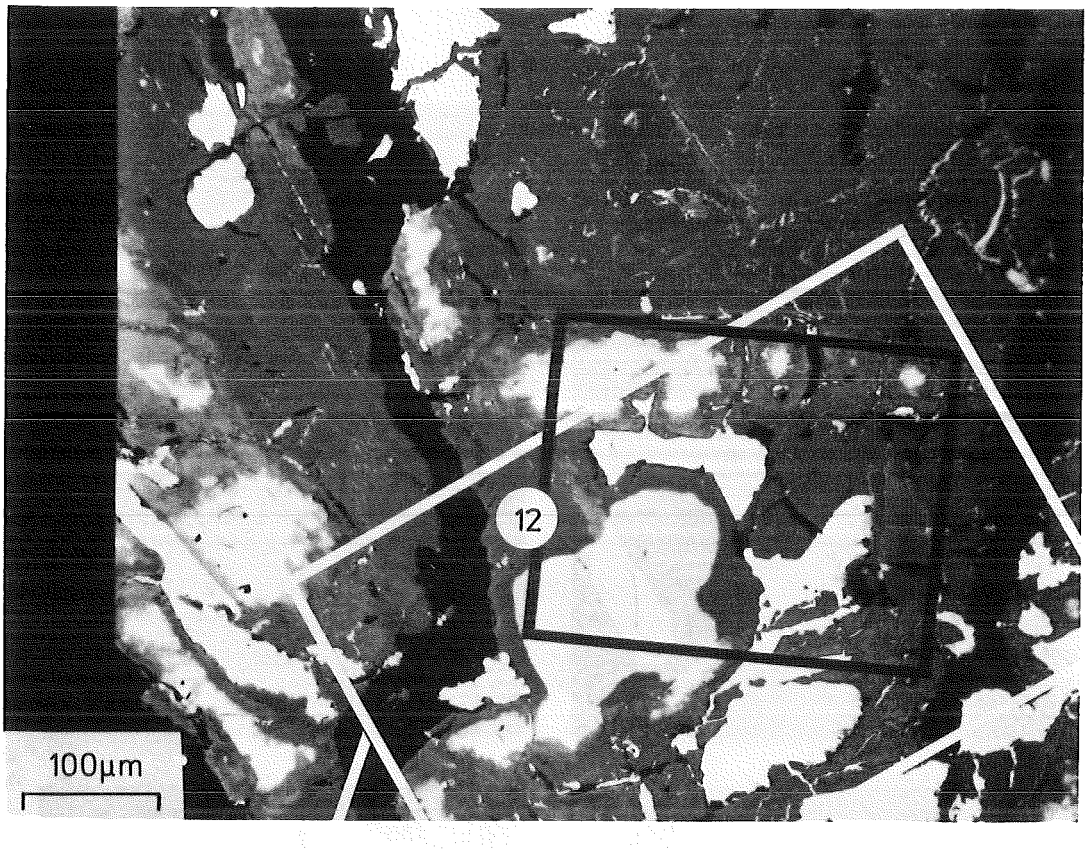

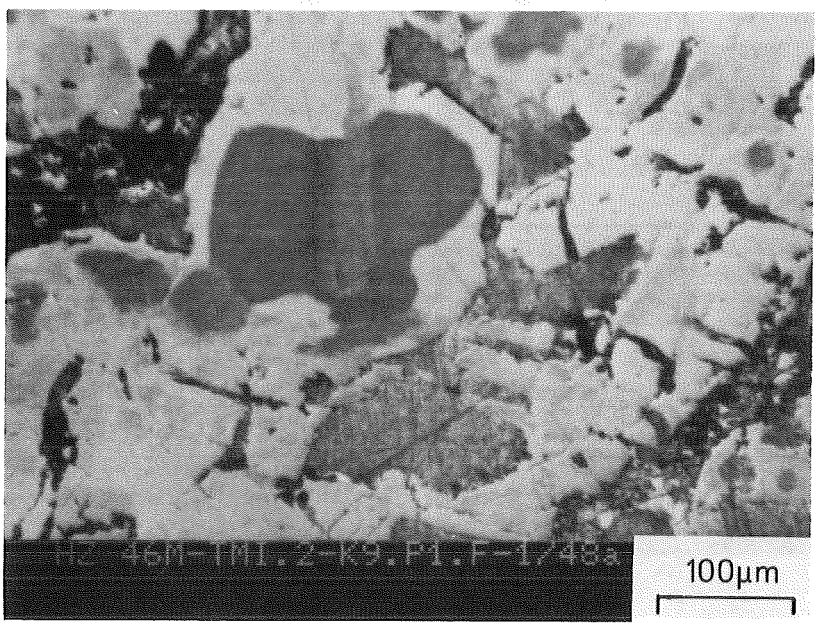

Fig. 12: Light-optical microstructure of core bore K9-P1, section F, sample 1, position b; the numbers refer to the quantitative analysis given in the tables; the black frame refers to the section in fig. 13.

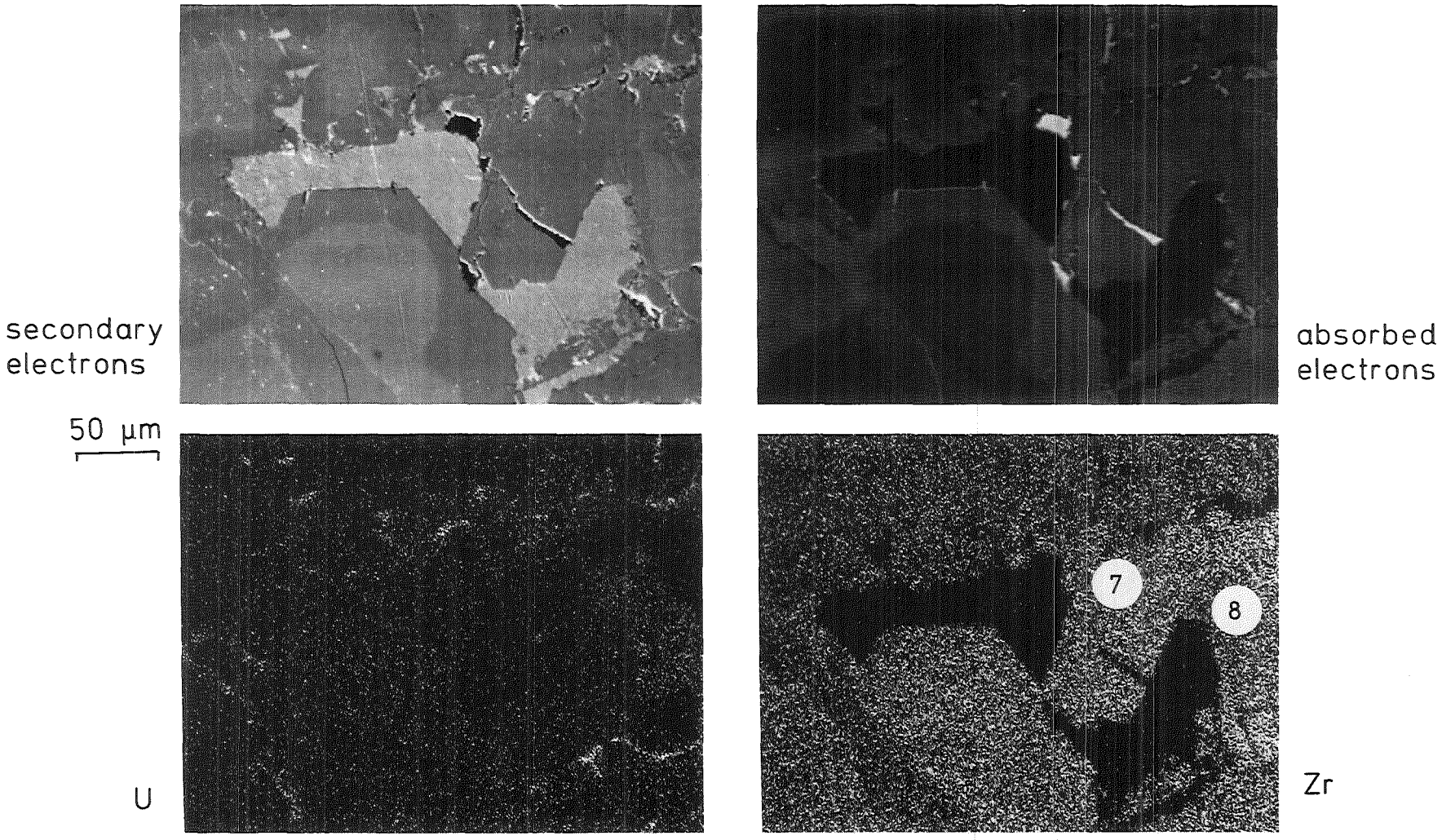

Fig. 13: Secondary electron image, absorbed electron image and element distribution of U, Zr, Fe, Cr, Ni, Sn, Ag, In, Al and O of core bore K9-P1, section F, sample 1, position b; the numbers refer to the quantitative analysis given in the tables.

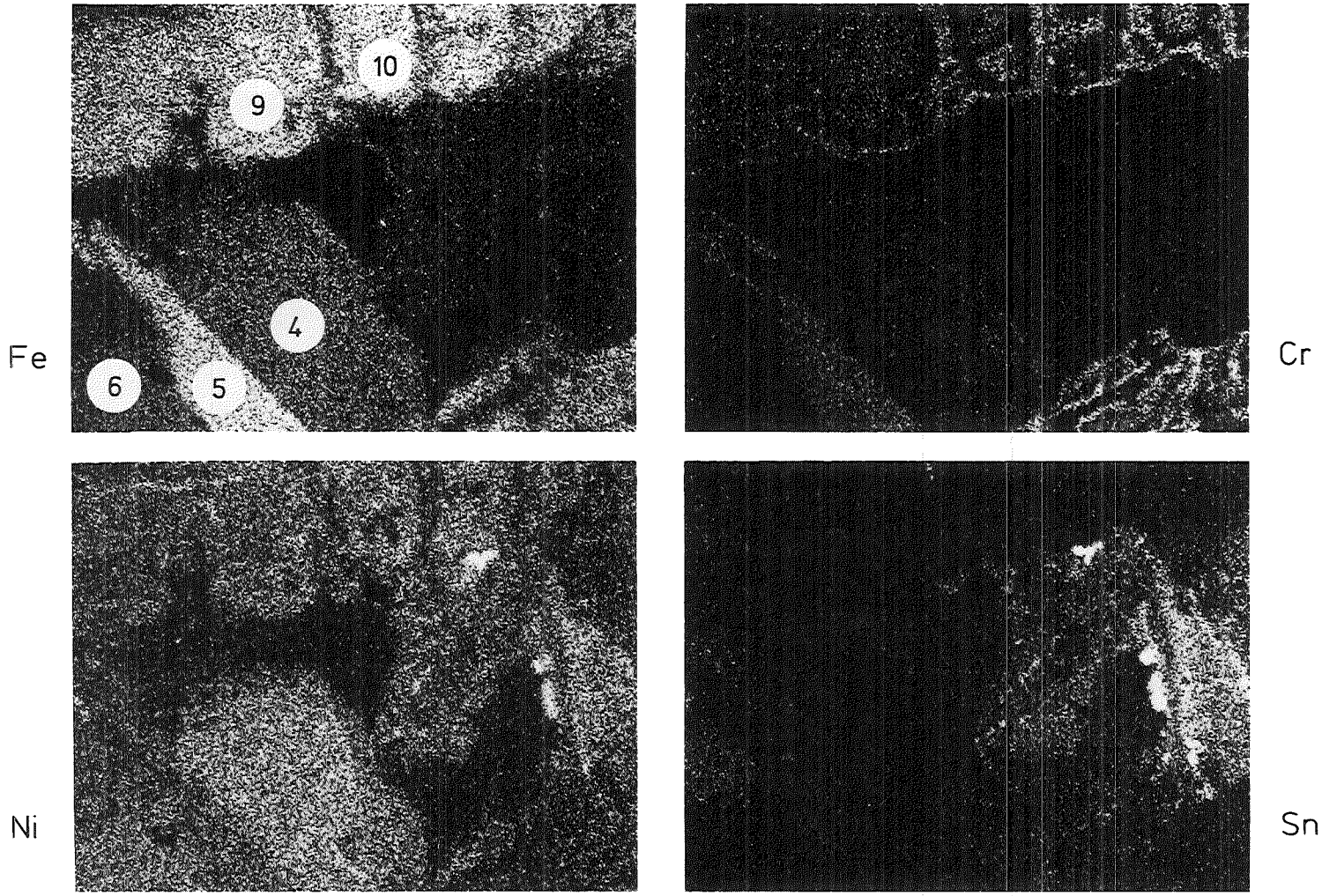

Fig. 13: continued.

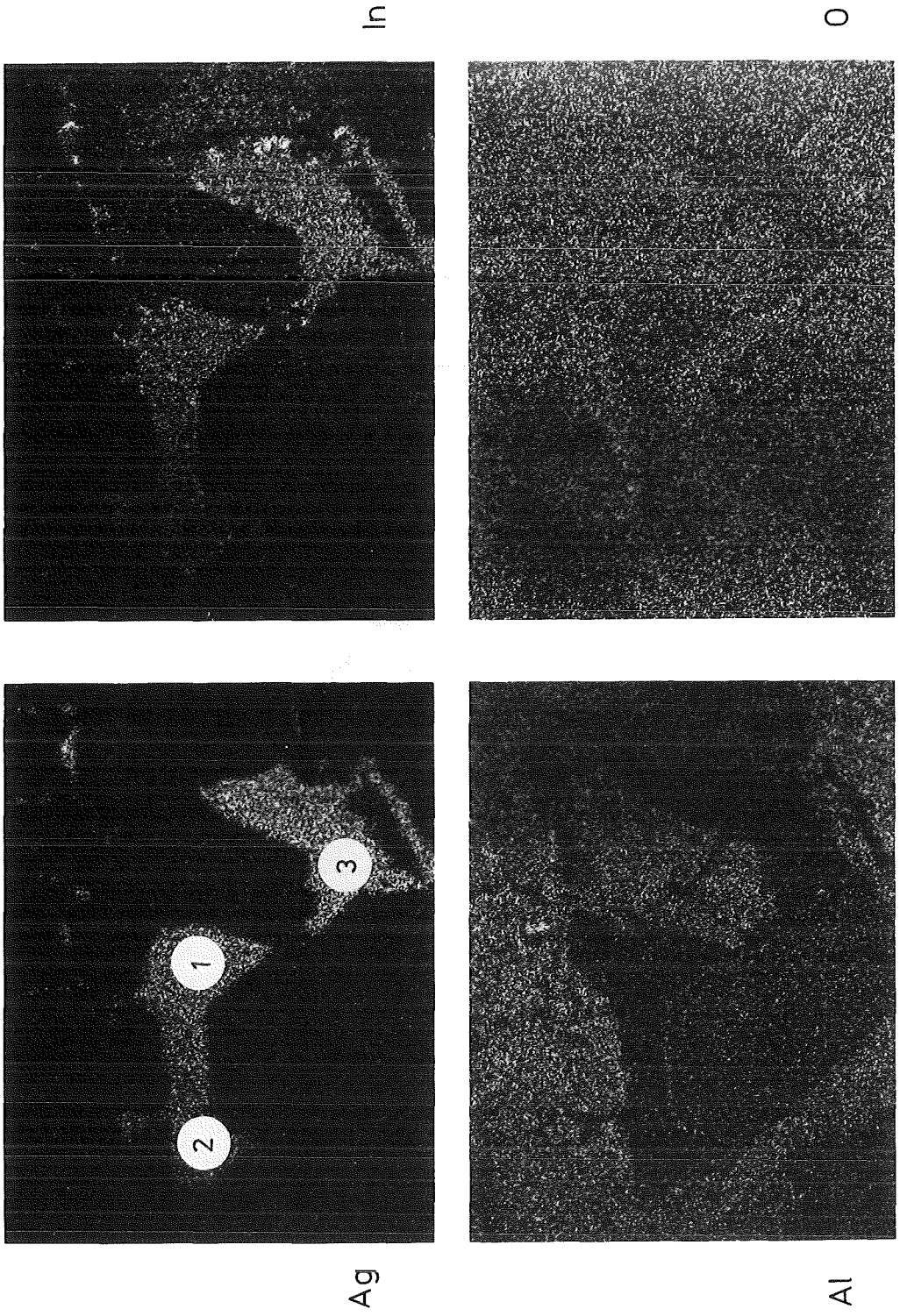

Fig. 13: continued.

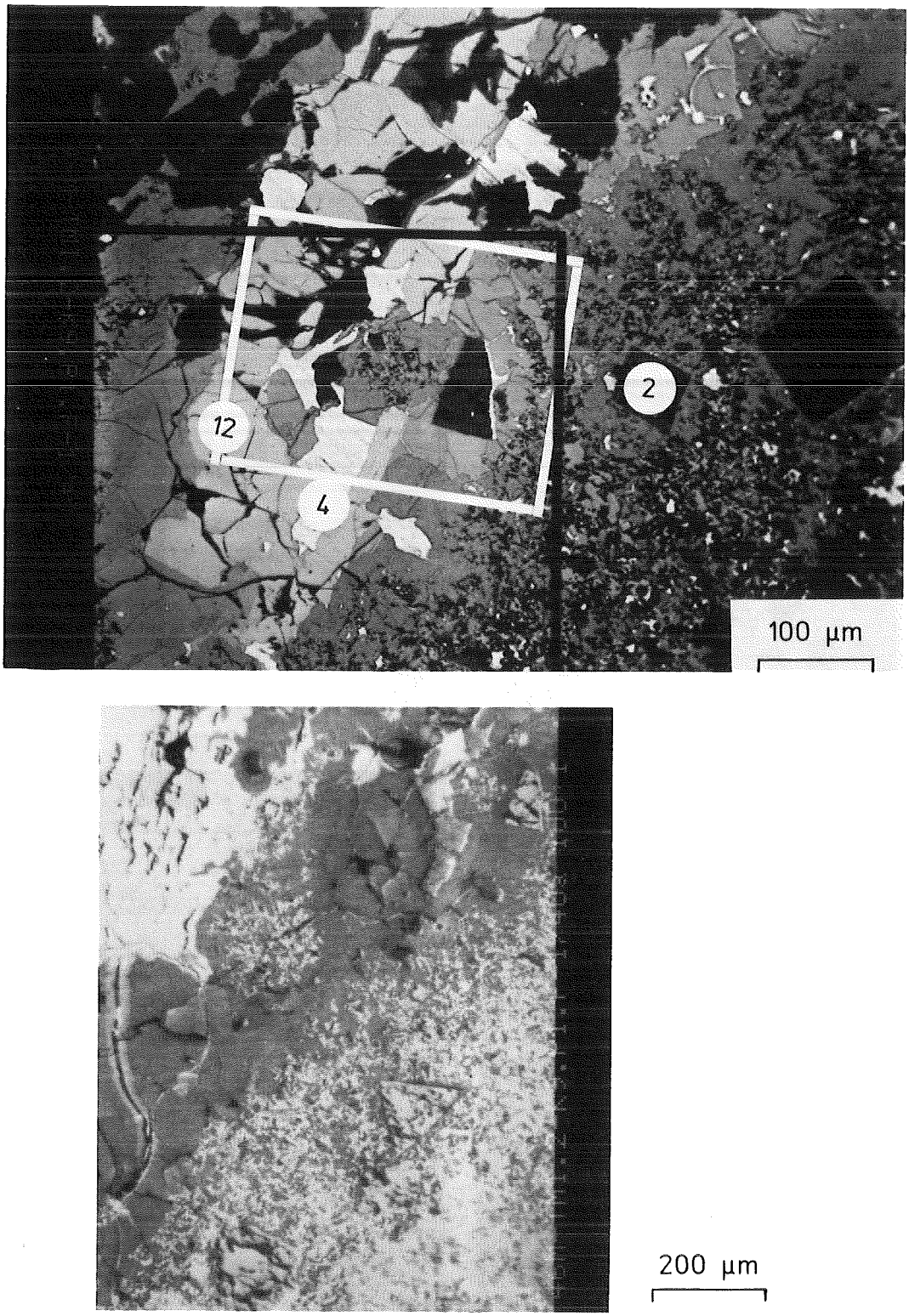

Fig. 14: Light-optical microstructure of core bore K9-P1, section F, sample 1, position c; the numbers refer to the quantitative analysis given in the tables; the white frame refers to the section in fig. 15.

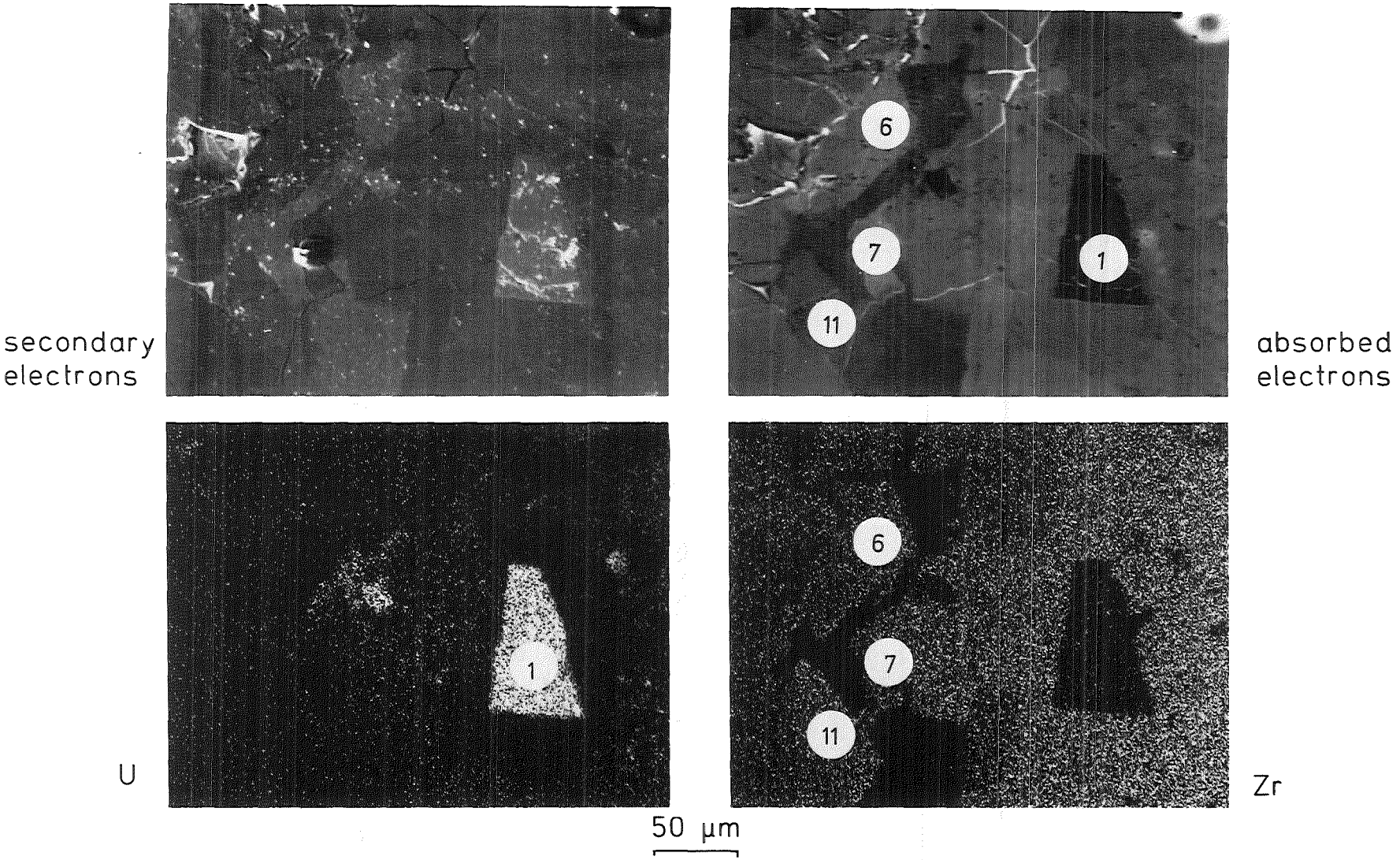

Fig. 15: Secondary electron image, absorbed electron image and element distribution of U, Zr, Fe, Cr, Ni, Sn, Ag, In, Al and O of core bore K9-P1, section F, sample 1, position c; the numbers refer to the quantitative analysis given in the tables.

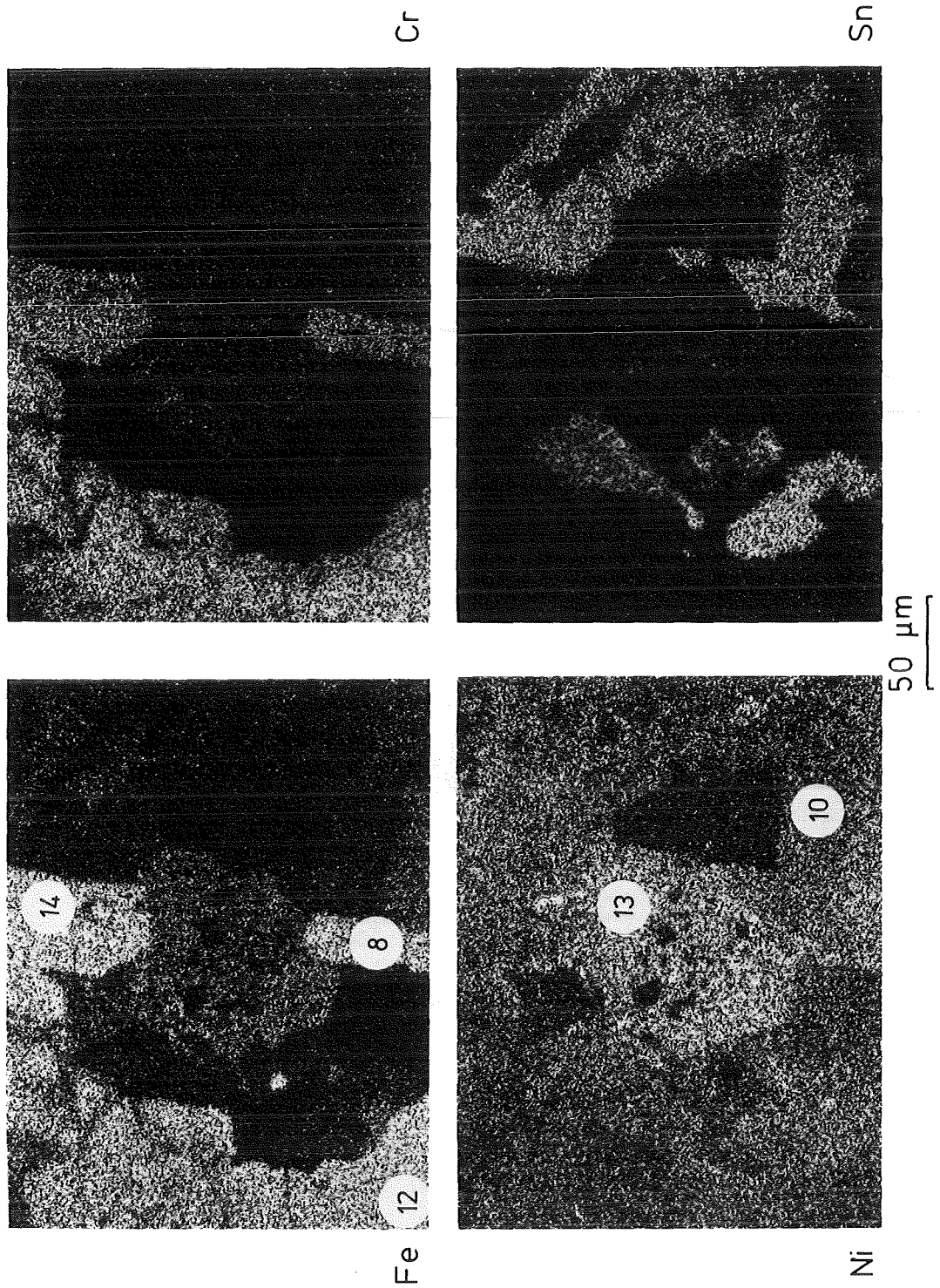

Fig. 15: continued.

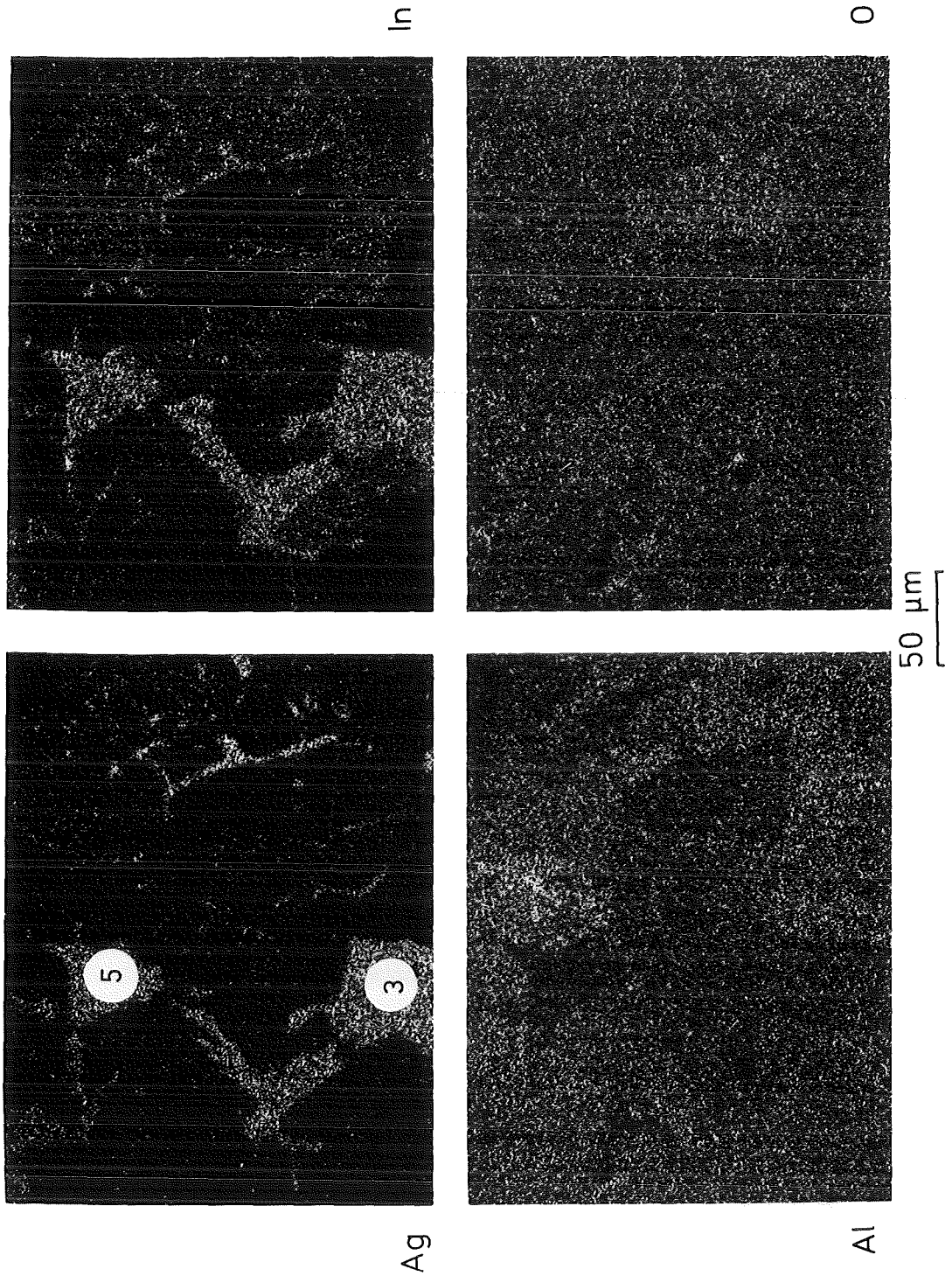

Fig. 15: continued.

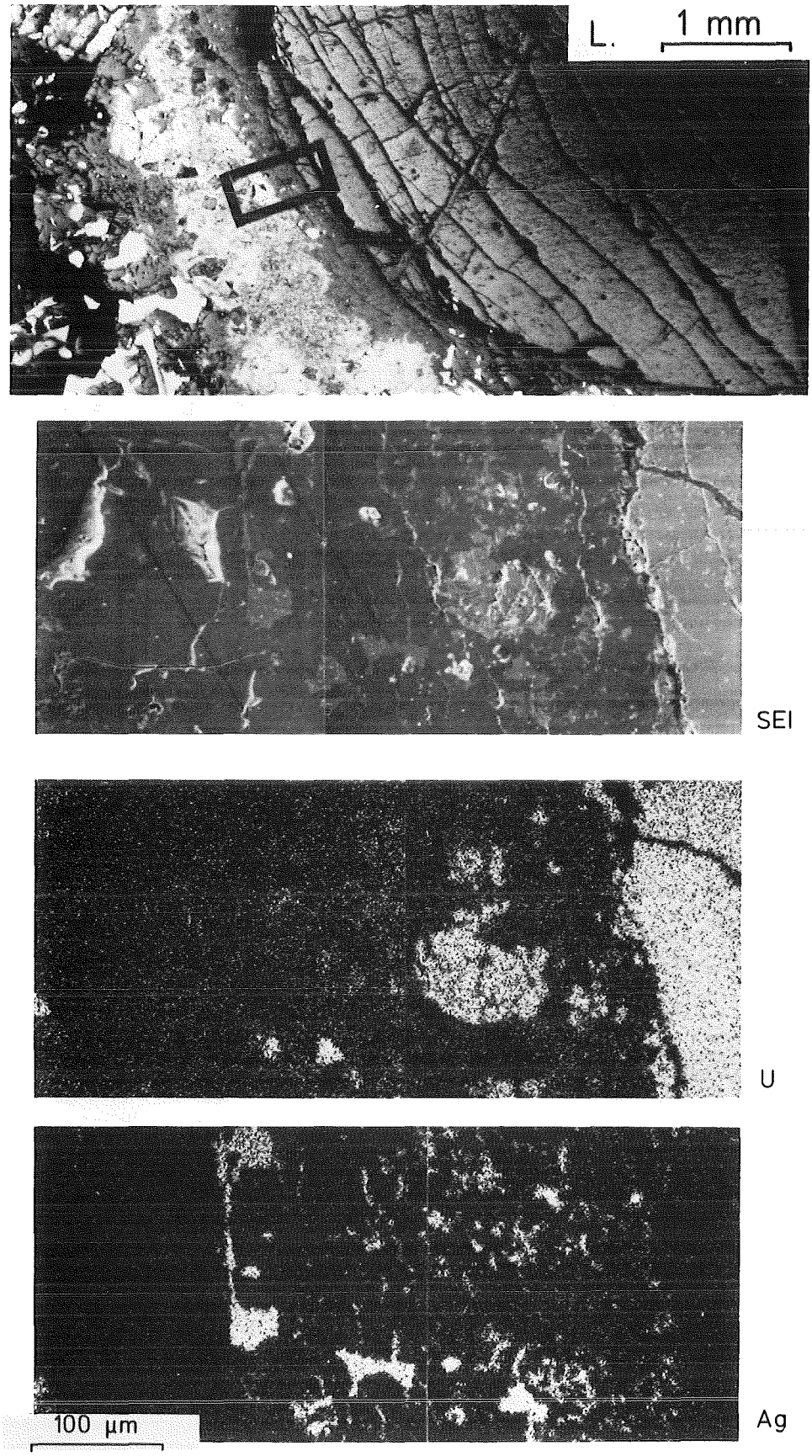

Fig. 16: Light-optical microstructure, secondary electron image, element distribution of Fe, Cr, Ni, U, Zr, Ag and Al and line scans of Zr and O of core bore K9-P1, section F, sample 1, position d, between the residue of a fuel pellet, oxidized Zircaloy-iron-nickel and precipitated $Zr(Fe,Cr)_2$ Laves phase.

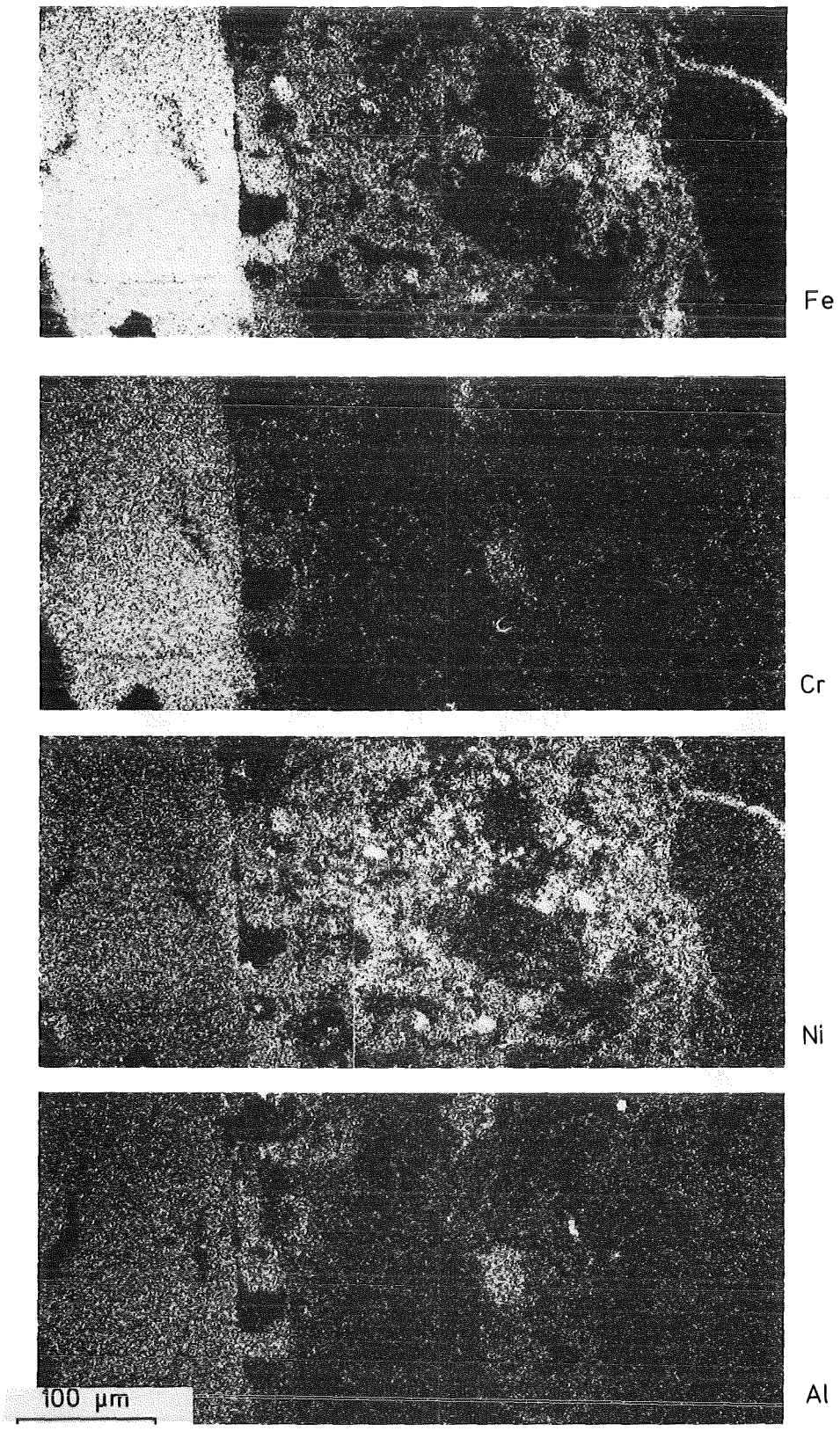

Fig. 16: continued.

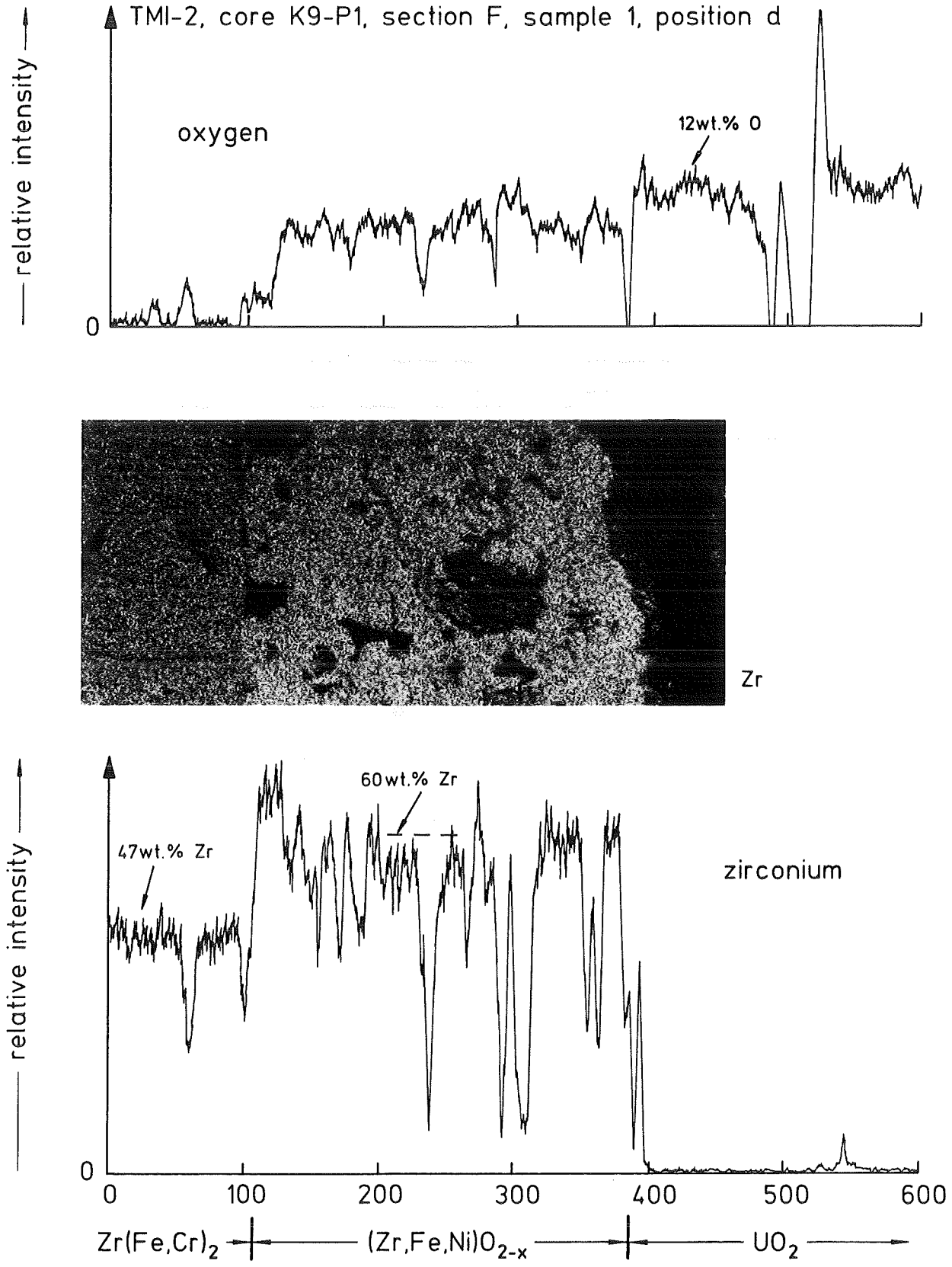

Fig. 16: continued.

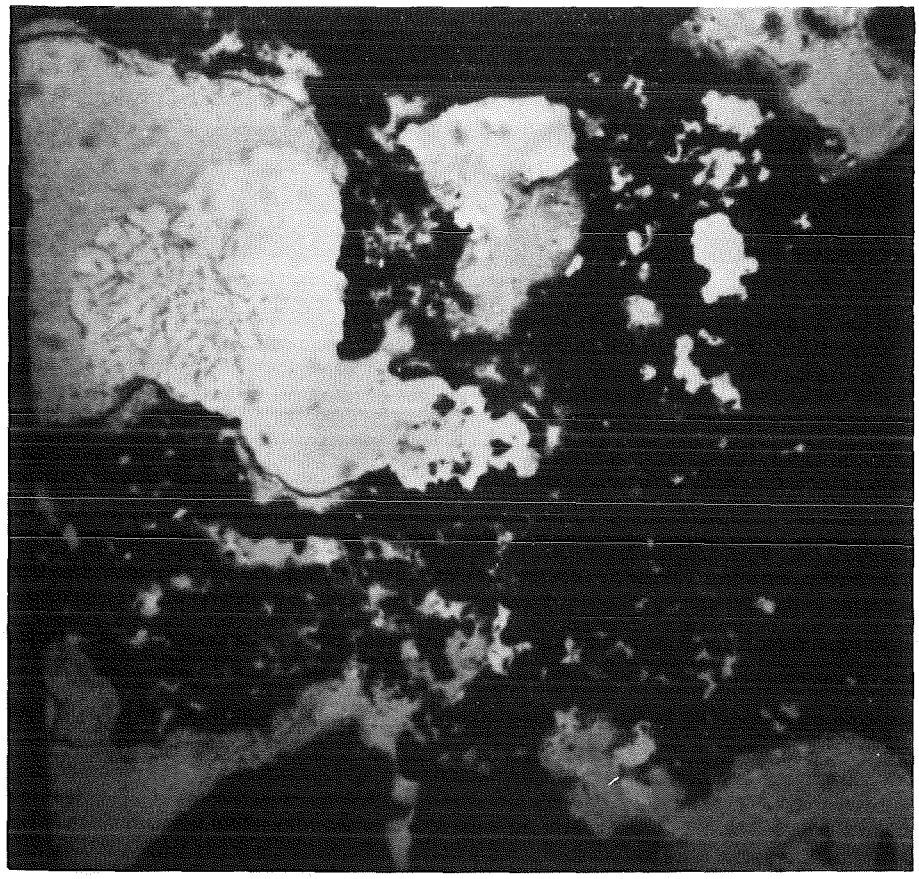

200 µm

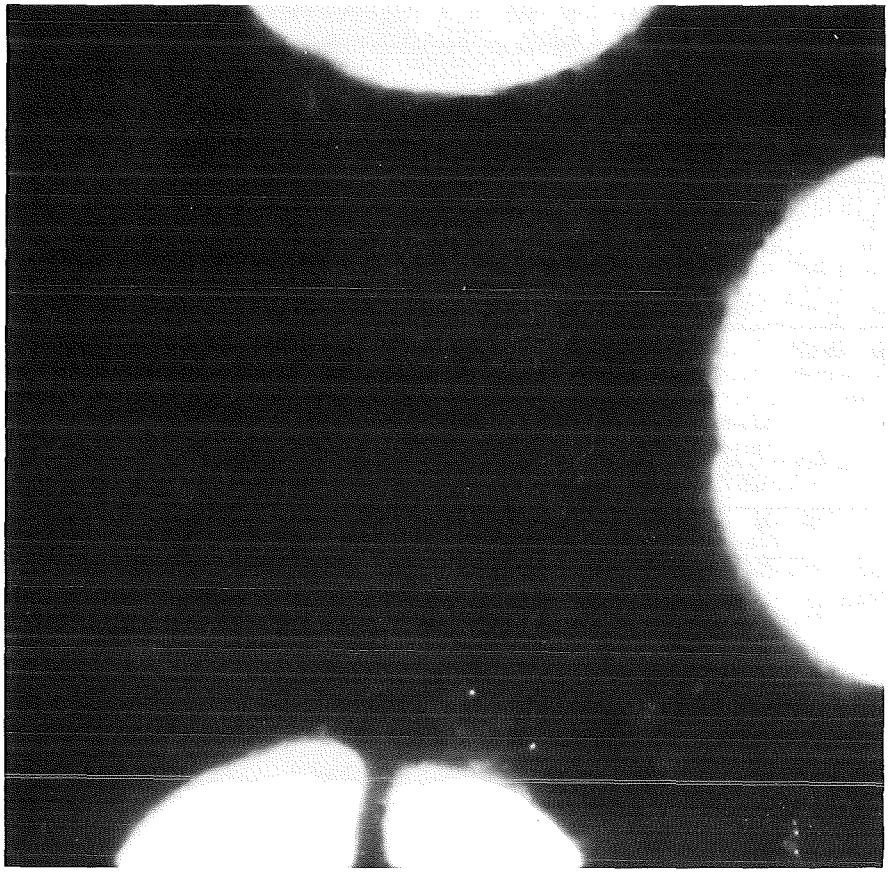

β : 40 s

Fig. 17: Light-optical microstructure and β autoradiograph (exposure time 40 s) of core bore D8-P1, section A, in the lower crust region showing the fuel pin remnants and the β-γ free regions.

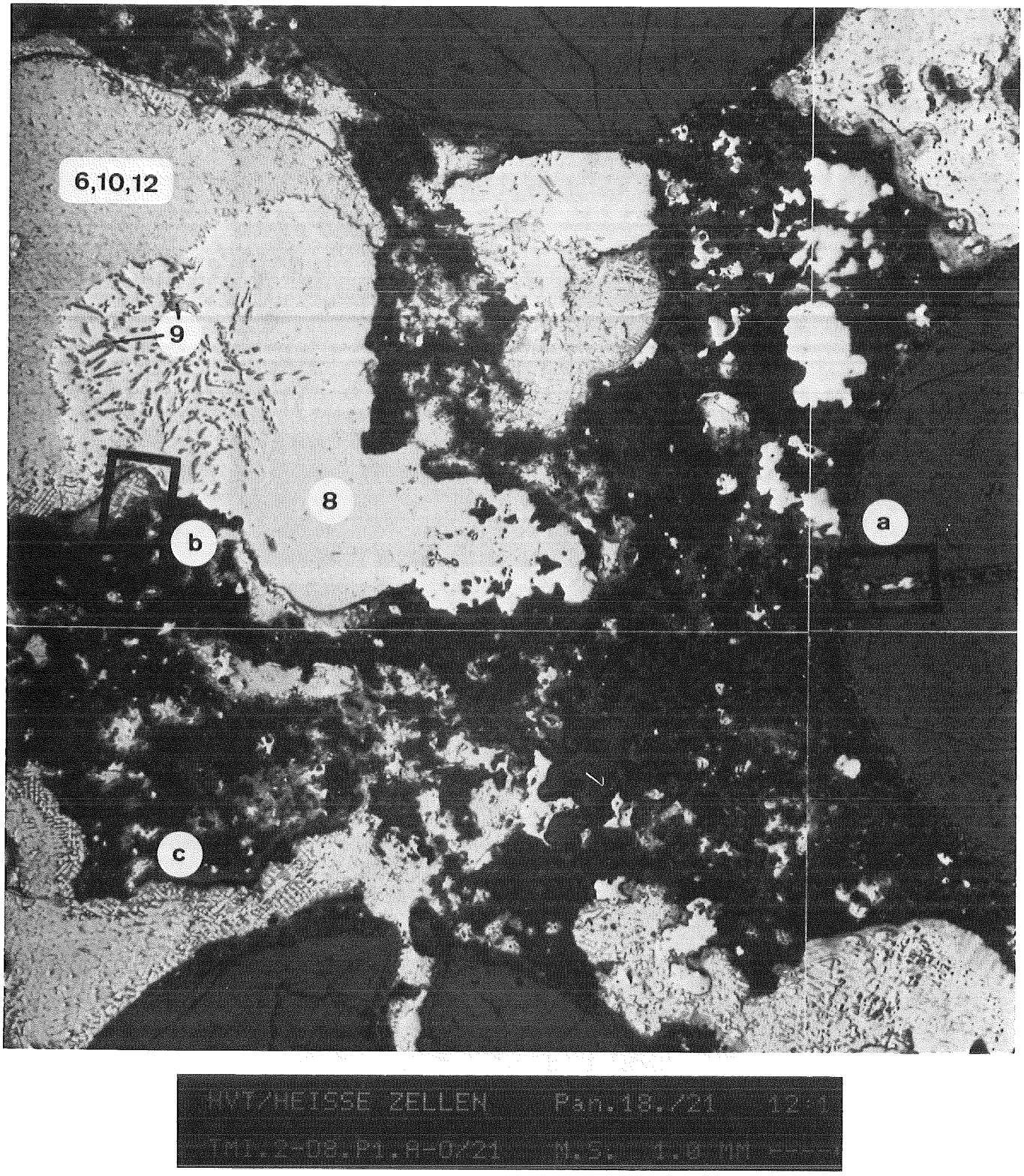

Fig. 18: View of the polished surface of core bore D8-P1, section A, lower crust region; the frames a and b refer to the light-optical microstructure details in fig. 19 and fig. 21.

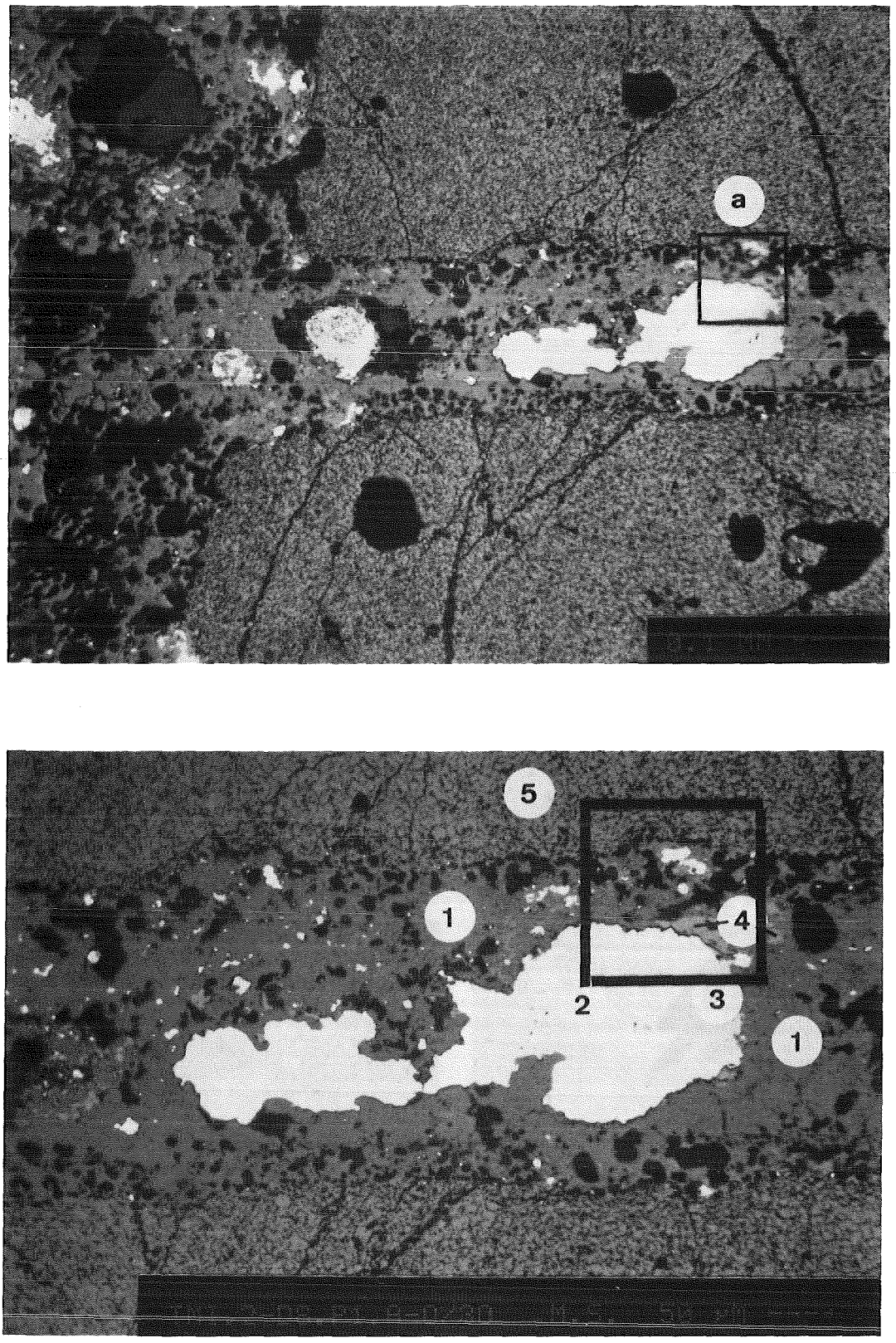

Fig. 19: Light-optical microstructure of core bore D8-P1, section A, detail a in fig. 18; frame a refers to the analyzed area in fig. 20.

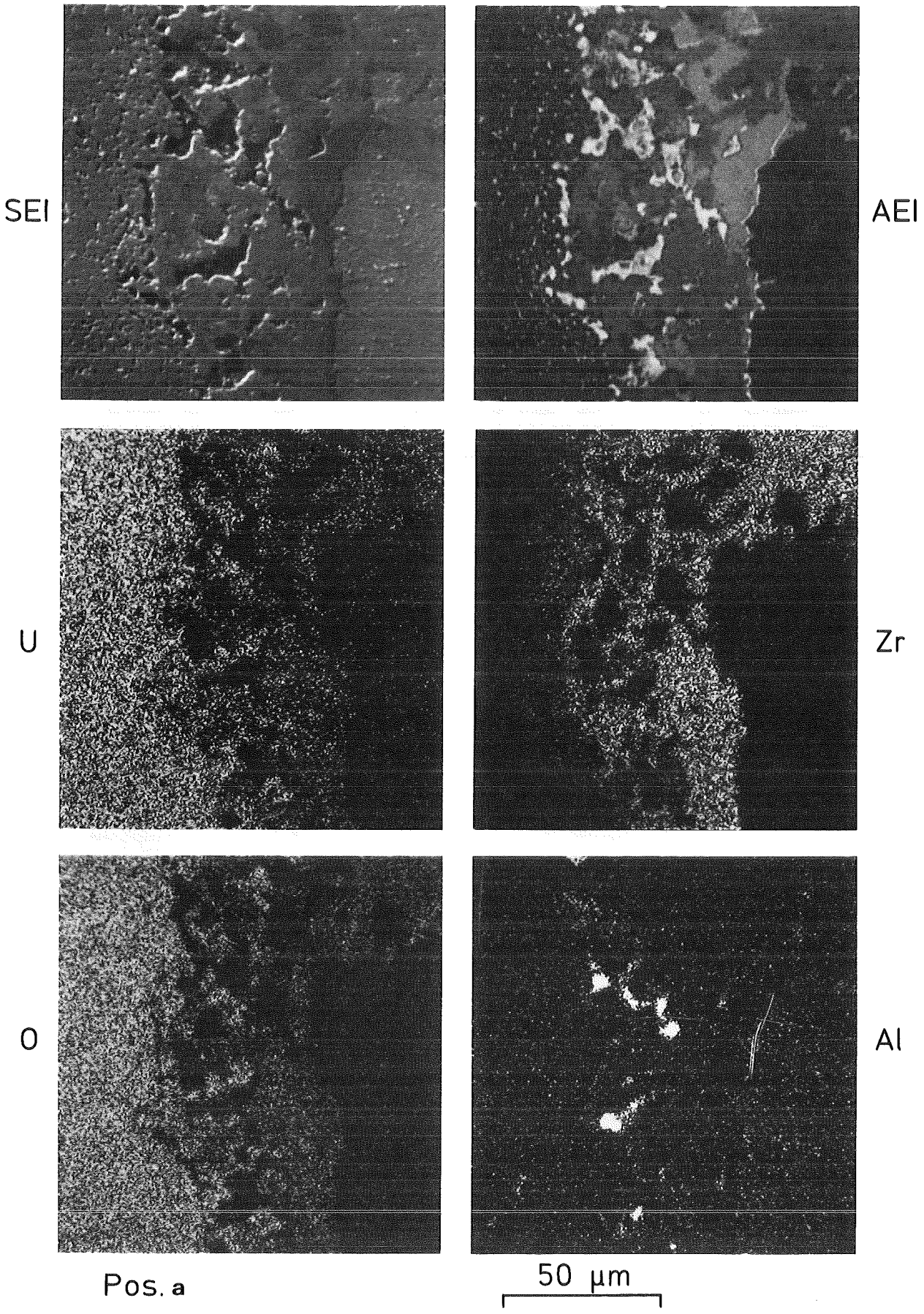

Fig. 20: Secondary and absorbed electron image and U, Zr, O, Al, Fe, Ni, Cr, Sn, Ag and In element distribution of core bore D8-P1, section A, detail a in fig. 19.

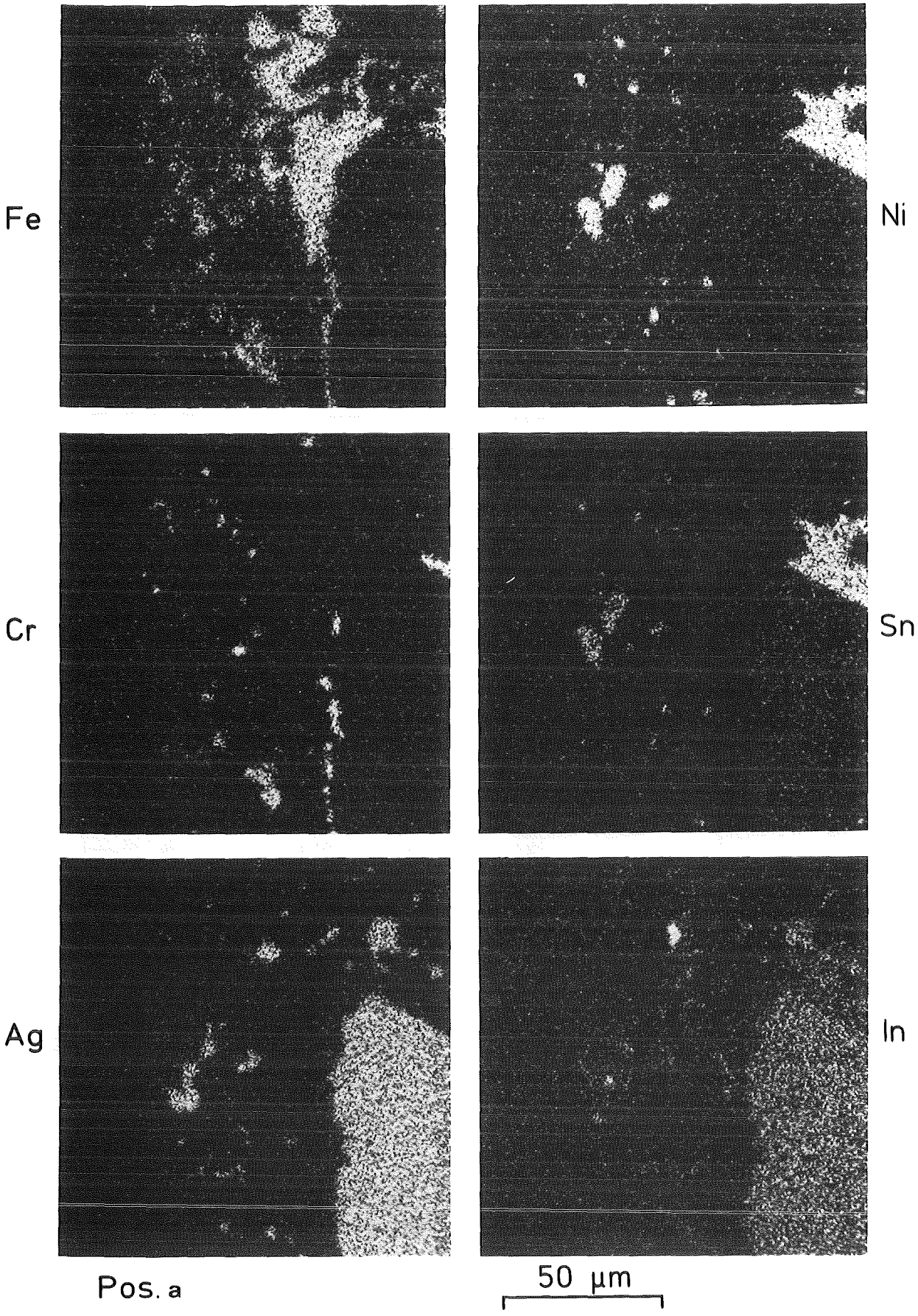

Fig. 20: continued.

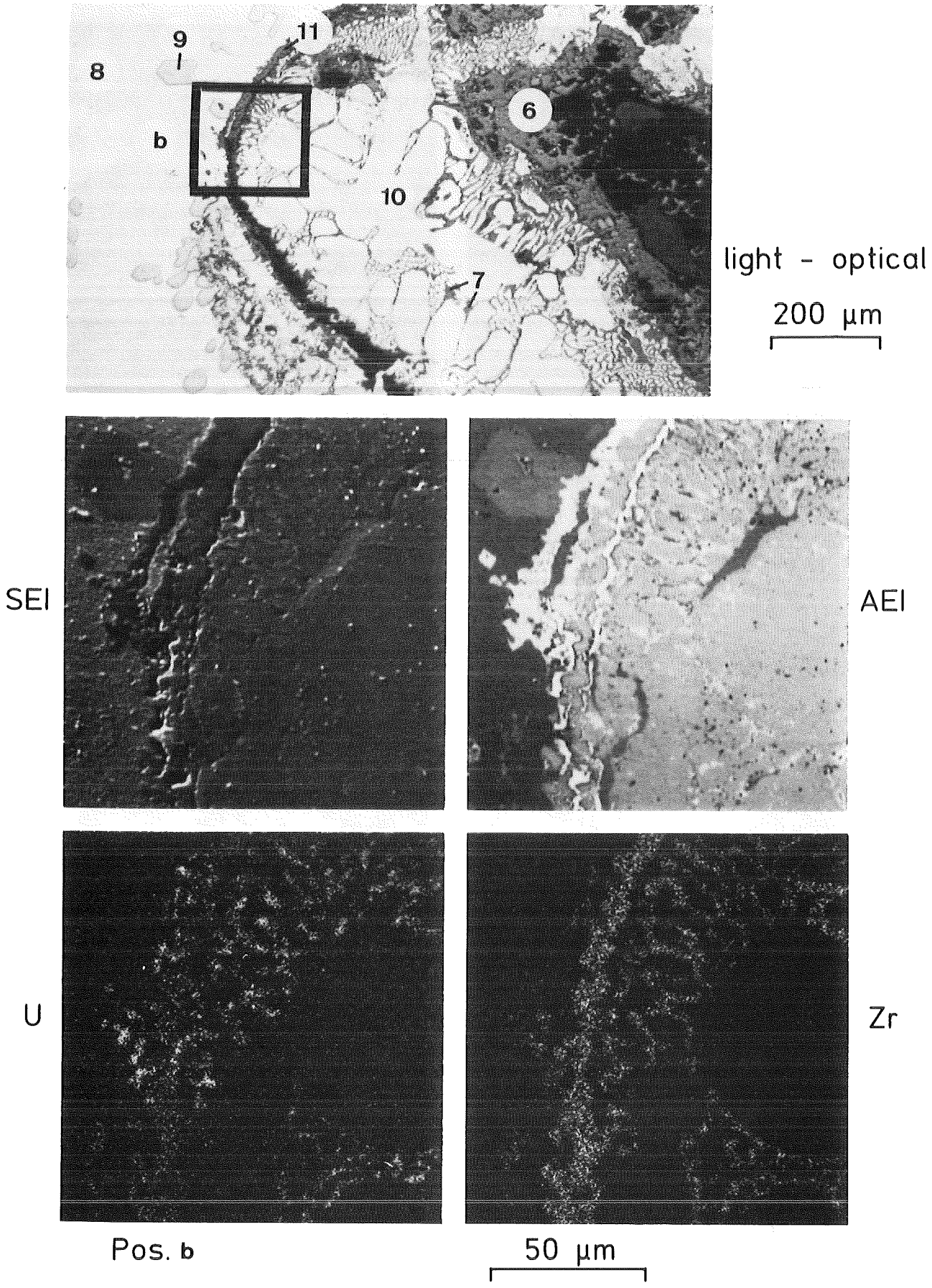

Fig. 21: Light-optical microstructure, secondary and absorbed electron image and U, Zr, Fe, Ni, Cr, Sn, Ag and In element distribution of core bore D8-P1, section A, detail b in fig. 18; frame b refers to the analyzed area in this figure.

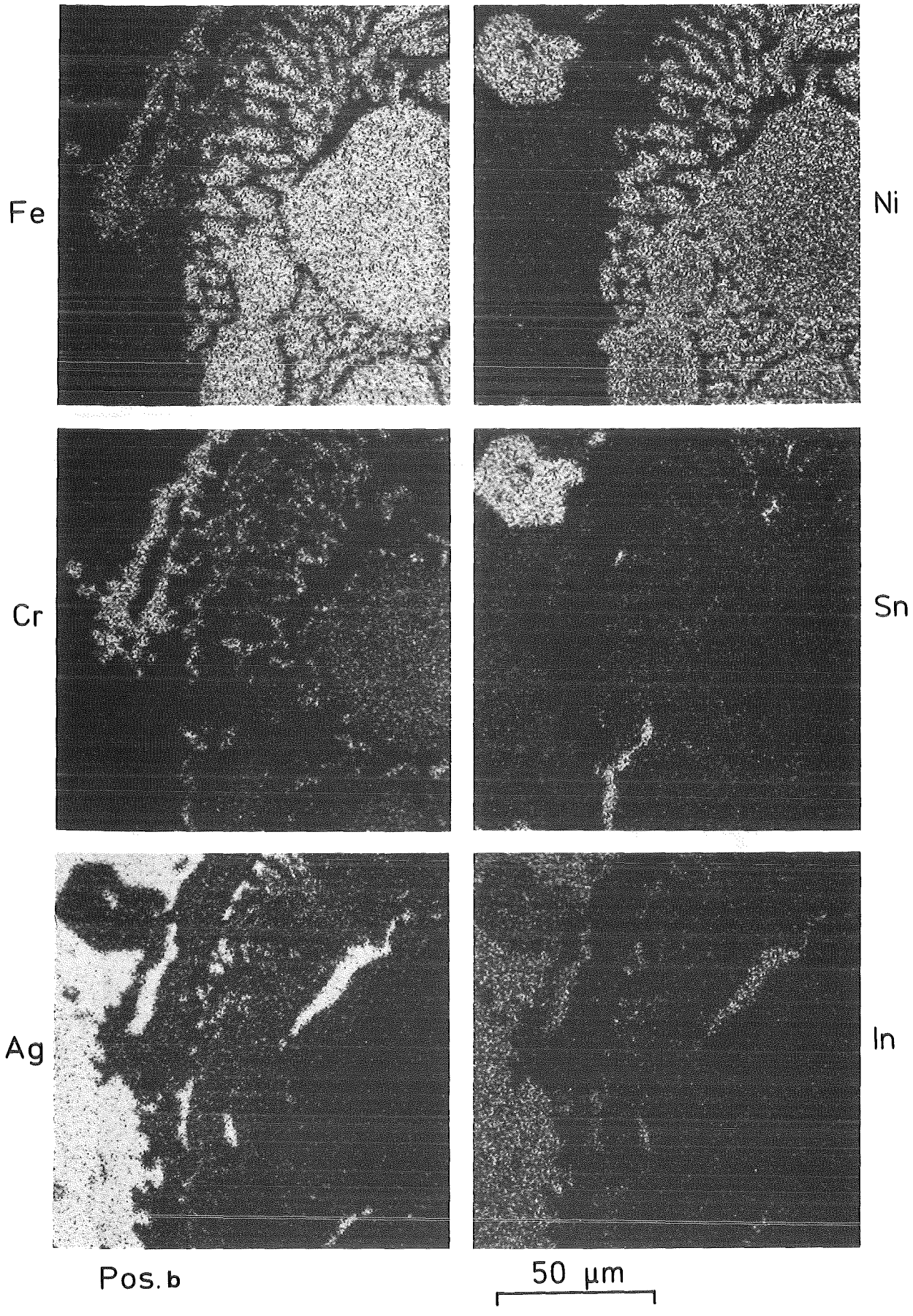

Fig. 21: continued.

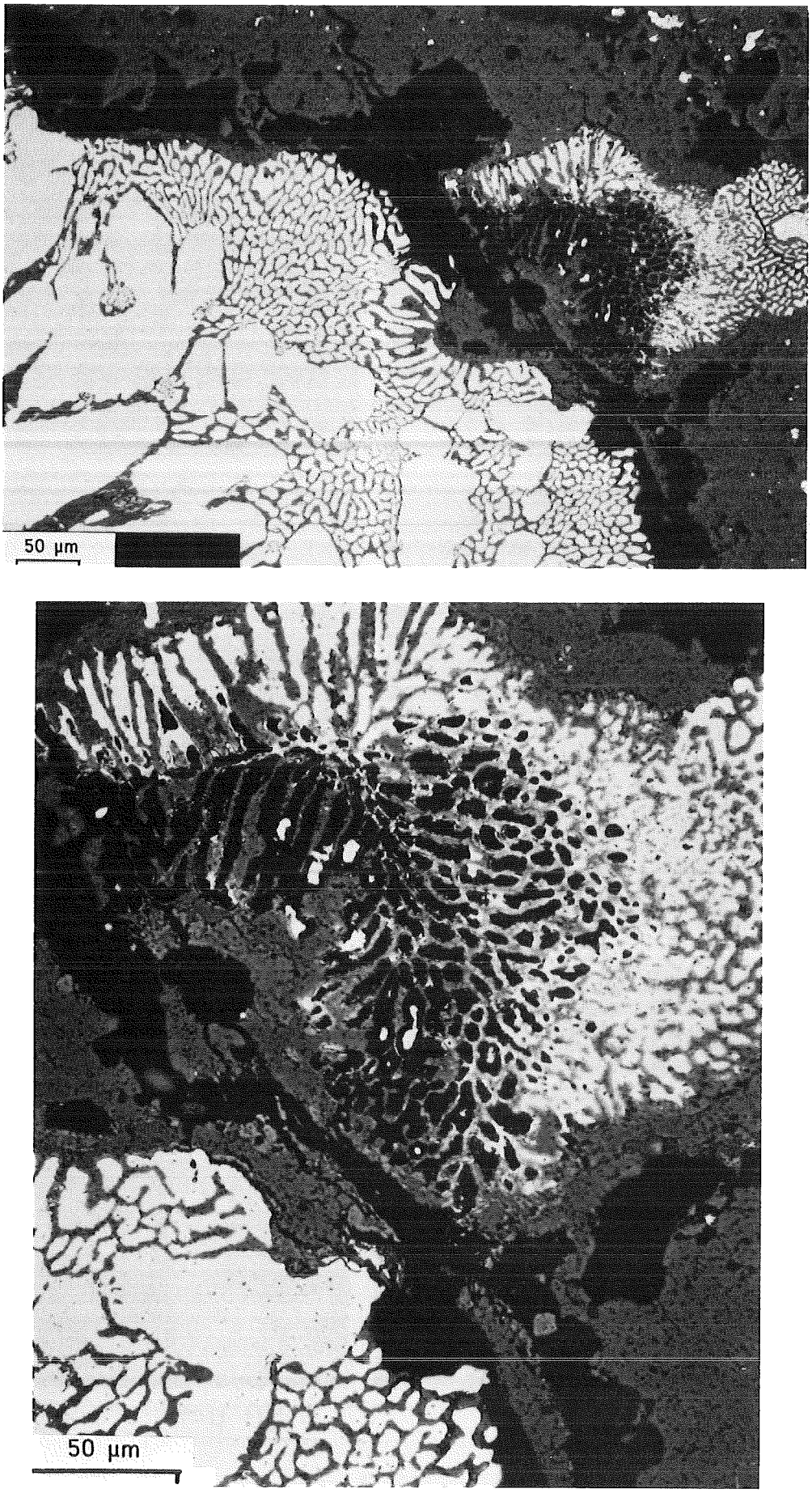

Fig. 22: Light-optical microstructure detail of core bore D8-P1, section A.

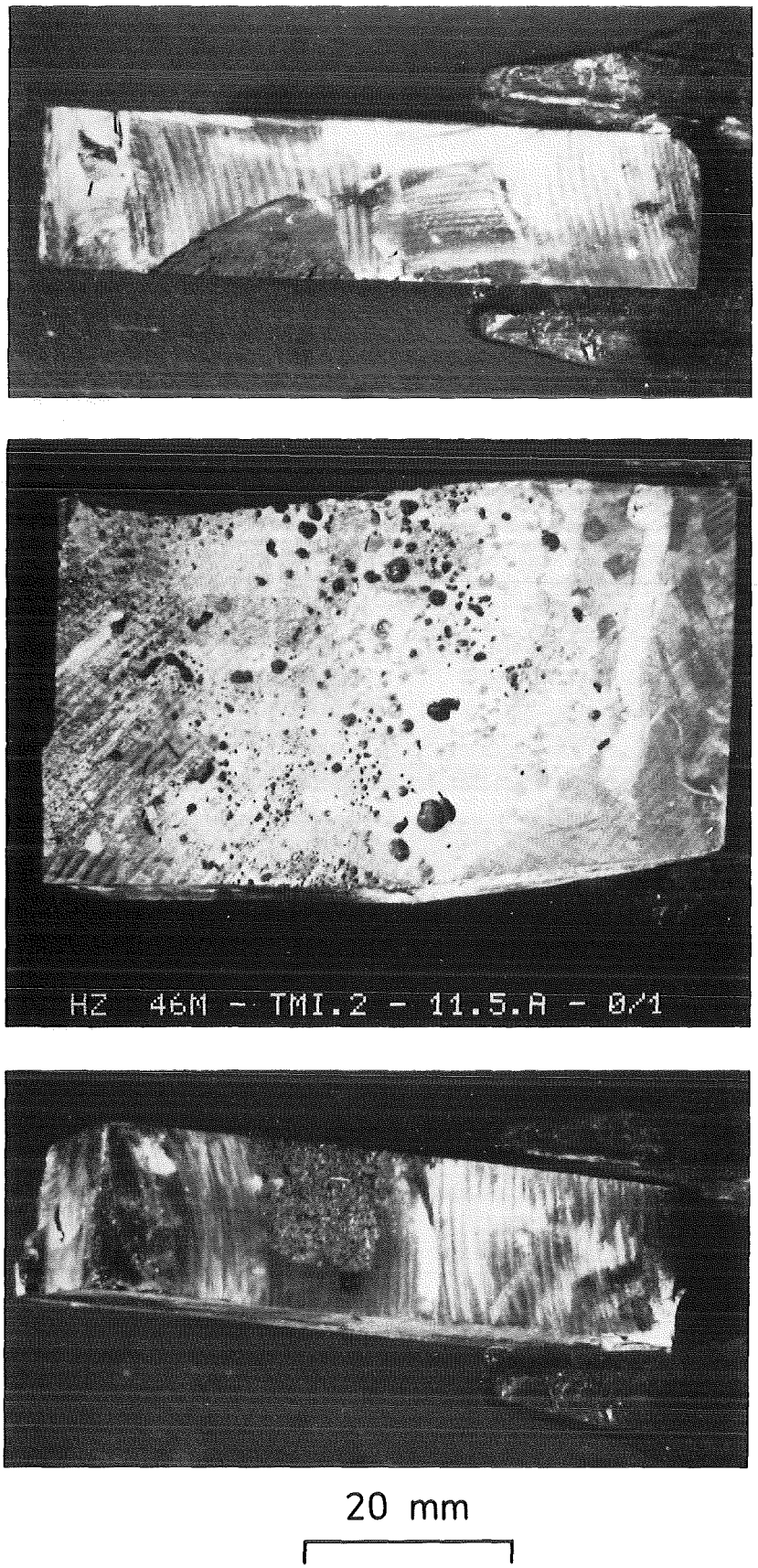

Fig. 23: View of a slice of the lower plenum core debris rock 11-5, section A.

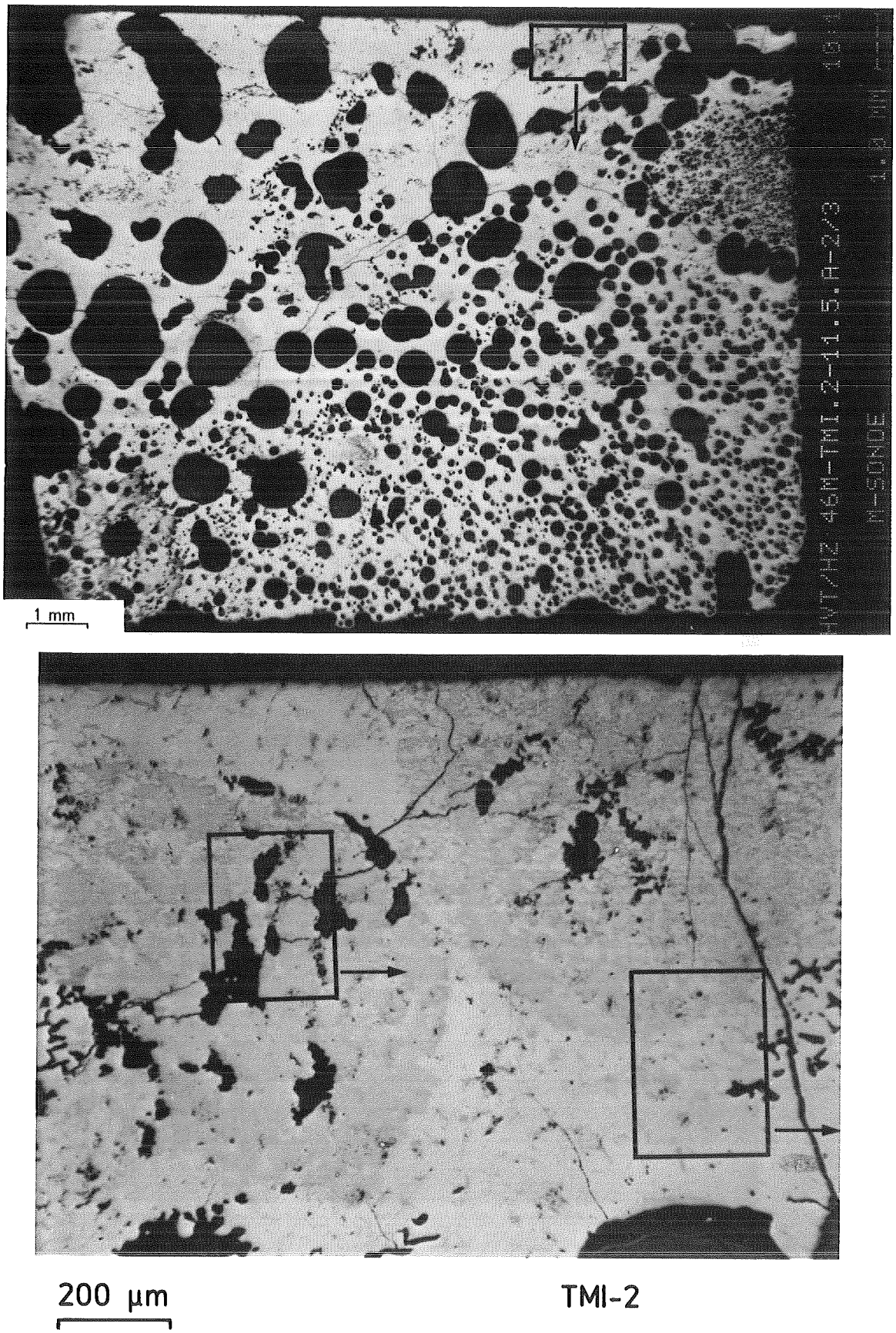

Fig. 24: Light-optical microstructure and detail of the lower plenum core debris rock 11-5, section A, sample 2a; the black frames in the lower microstructure refer to the investigated areas in figs. 26 and 27.

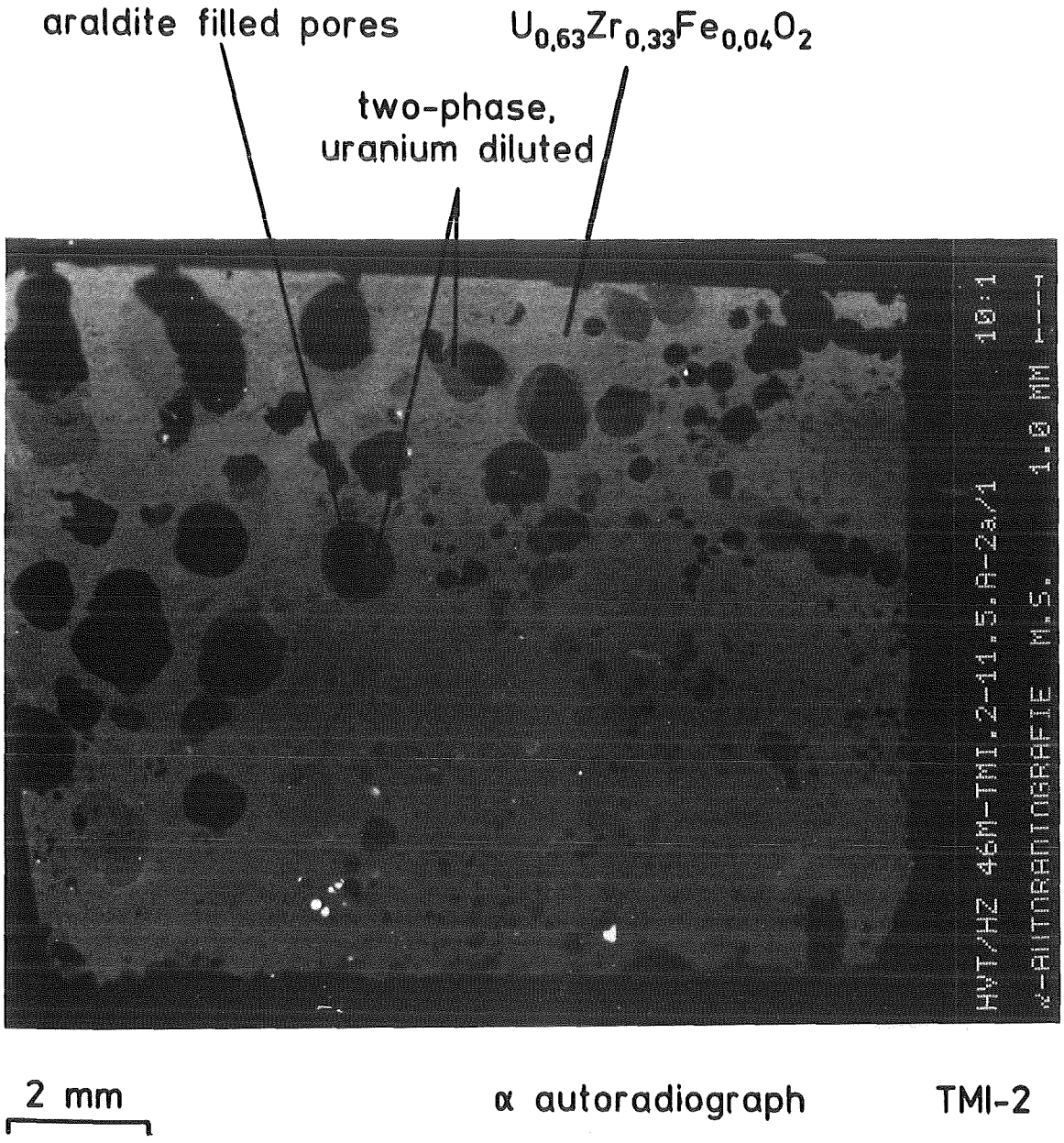

Fig. 25: α autoradiograph of the upper microstructure in fig. 24; light: $U_{0.63}Zr_{0.33}Fe_{0.04}O_2$; medium: two-phase $(U,Zr)O_2$-$Fe(Al,Cr,Ni,Zr)_2O_4$; dark: pores.

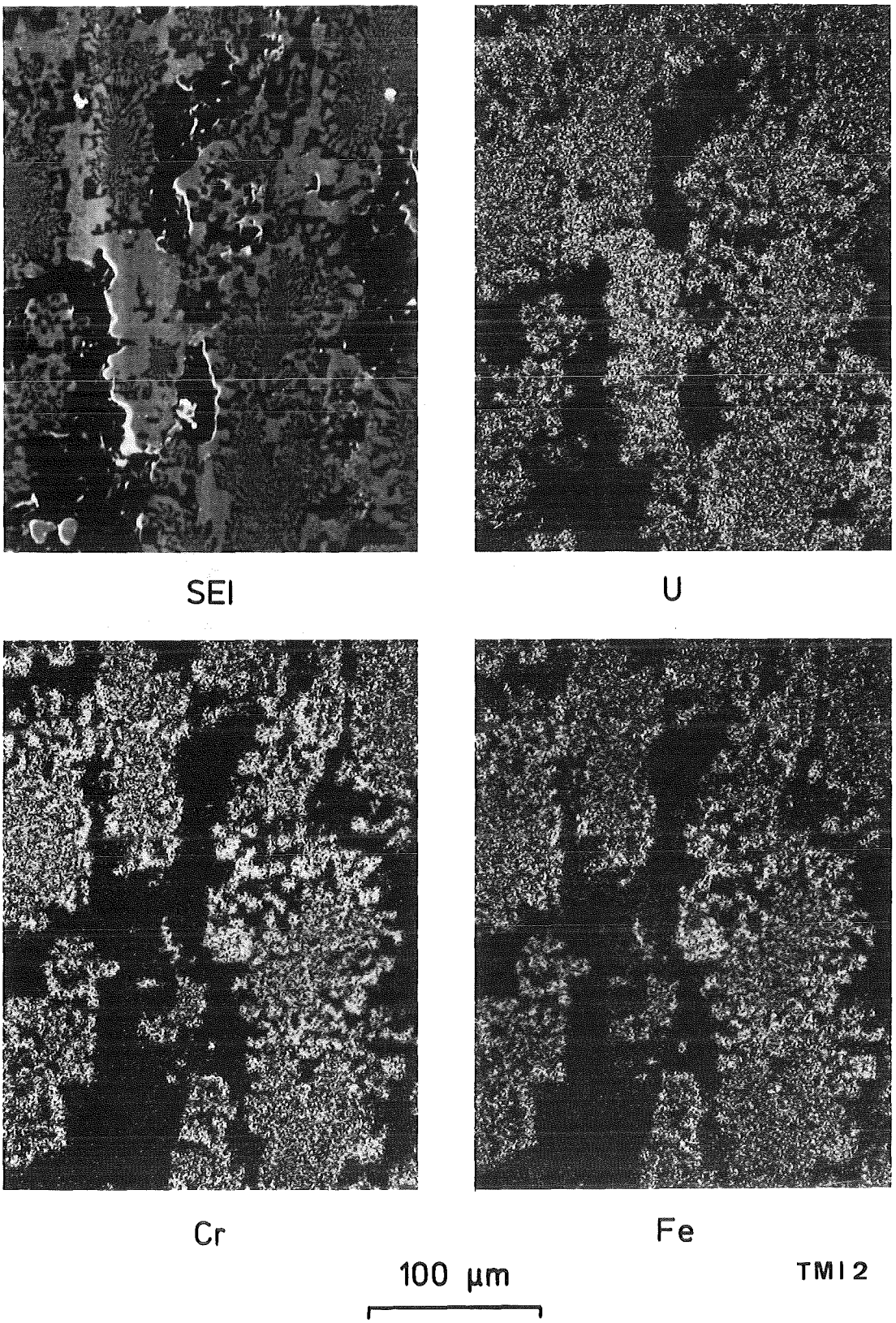

Fig. 26: Secondary electron image and U, Cr and Fe element distribution of the lower plenum core debris rock 11-5, section A, sample 2a showing the $(U,Zr)O_2$-$Fe(Al,Cr,Ni,Zr)_2O_4$ eutectic structure.

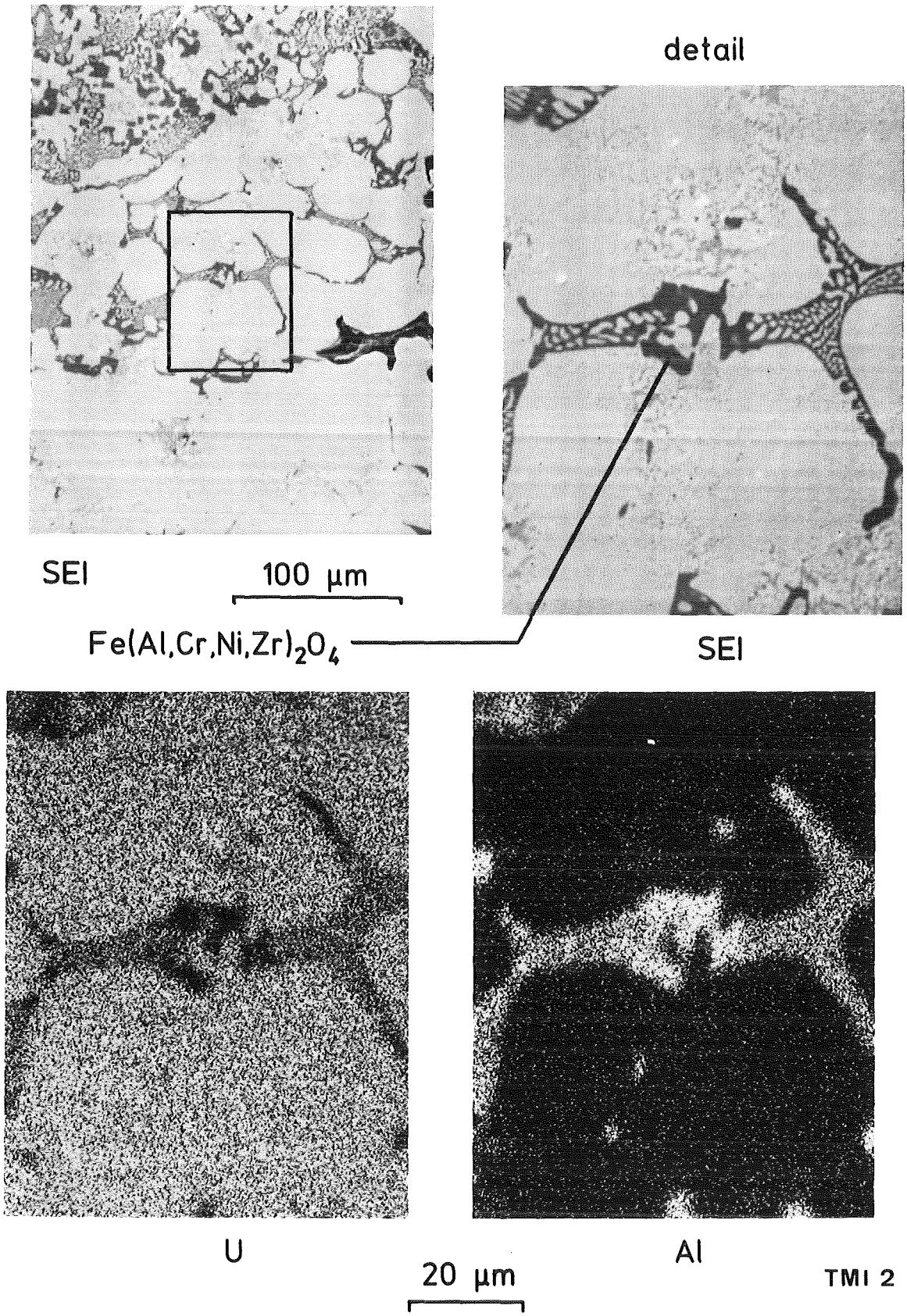

Fig. 27: Secondary electron images and U and Al element distribution of the lower plenum core debris rock 11-5, section A, sample 2a showing the $(U,Zr)O_2$-$Fe(Al,Cr,Ni,Zr)_2O_4$ eutectic structure.

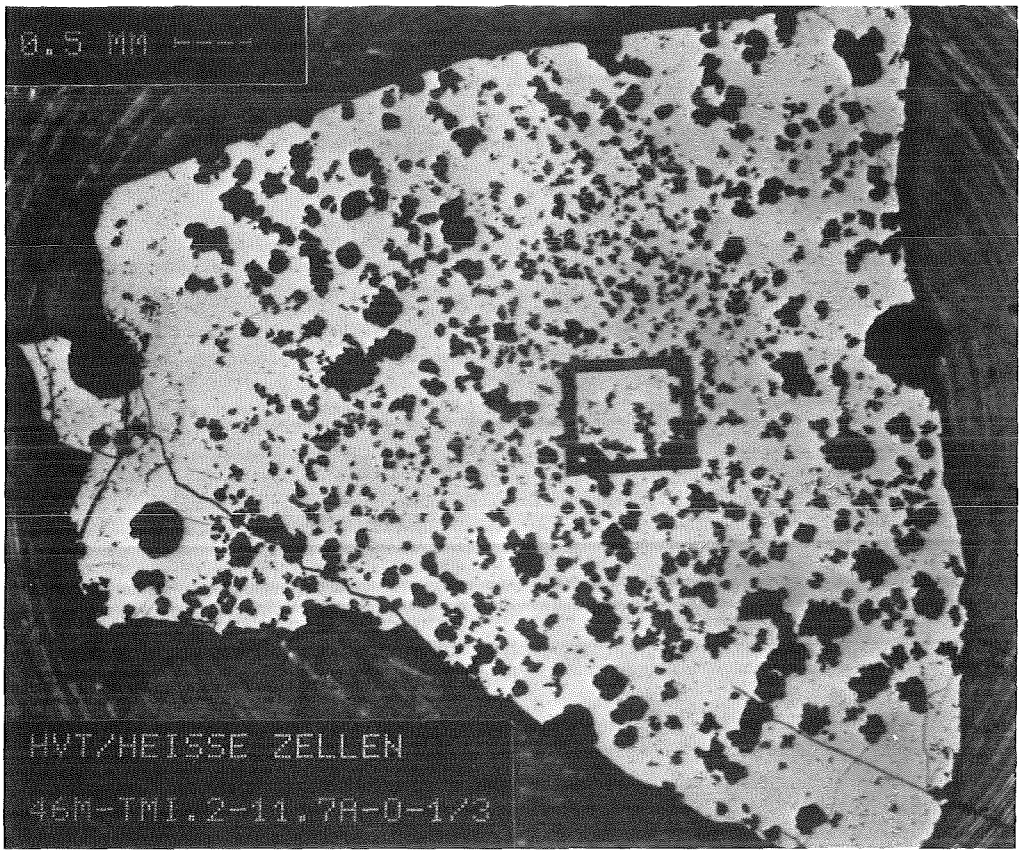

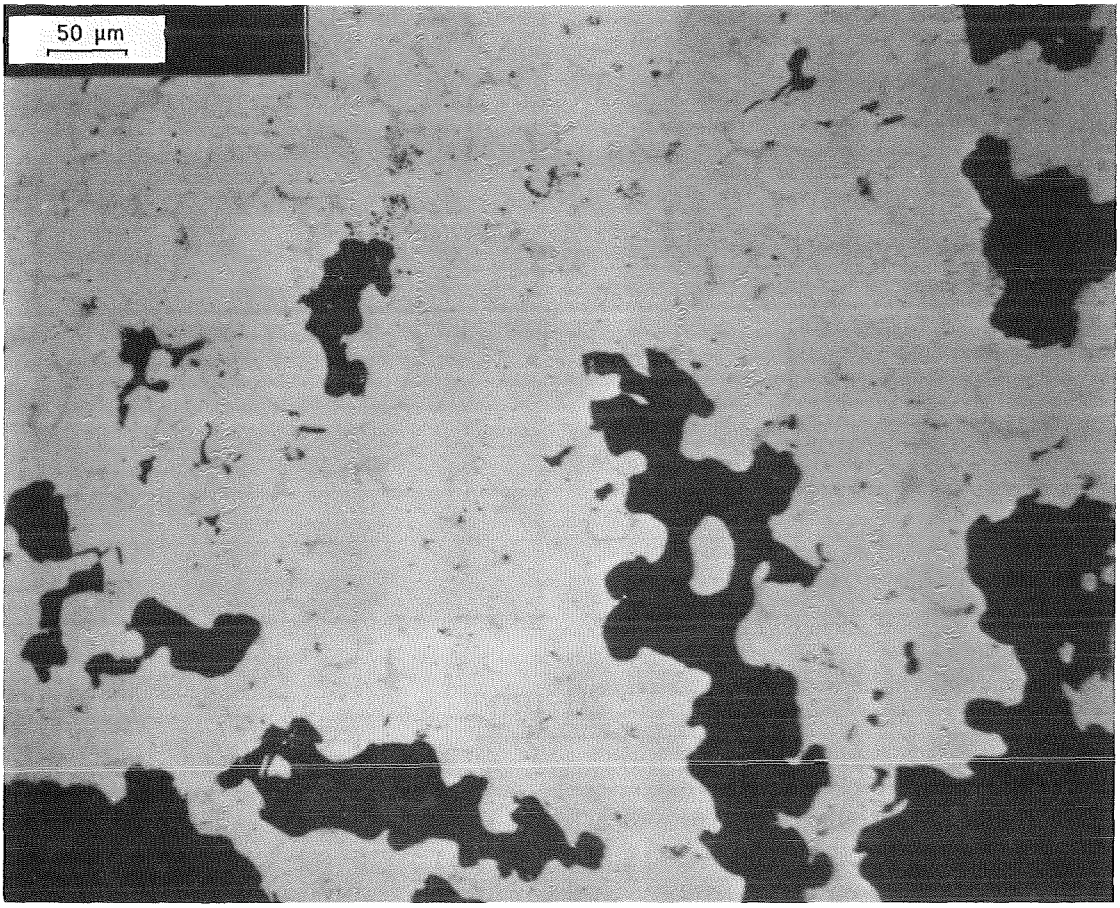

Fig. 28: Light-optical microstructure and detail of a cut of the lower plenum core debris rock 11-7, section A; light: c-$(U,Zr)O_2$ and t-$(Zr,U)O_2$, grey: $(U,Zr)O_2$-spinel eutectic, dark: pores.

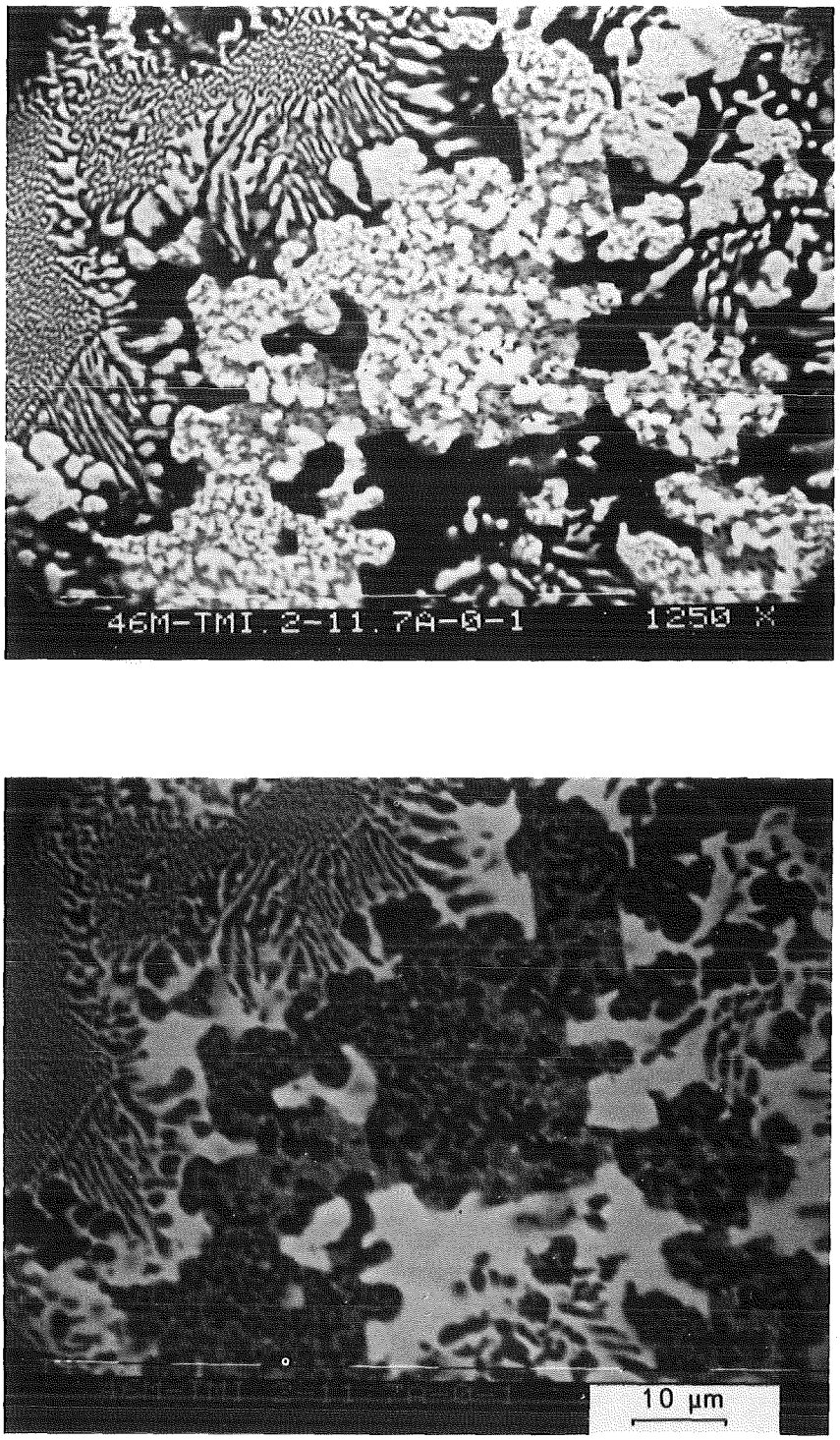

Fig. 29: Secondary electron (top) and absorbed electron images of a smaller area of the lower plenum core debris rock 11-7, section A, showing three phases: $U(Zr)O_2$ (light), $Zr(U)O_2$ (grey) and the spinel $Fe(Al,Cr,Ni,Zr)_2O_4$ (black) in the AEI.

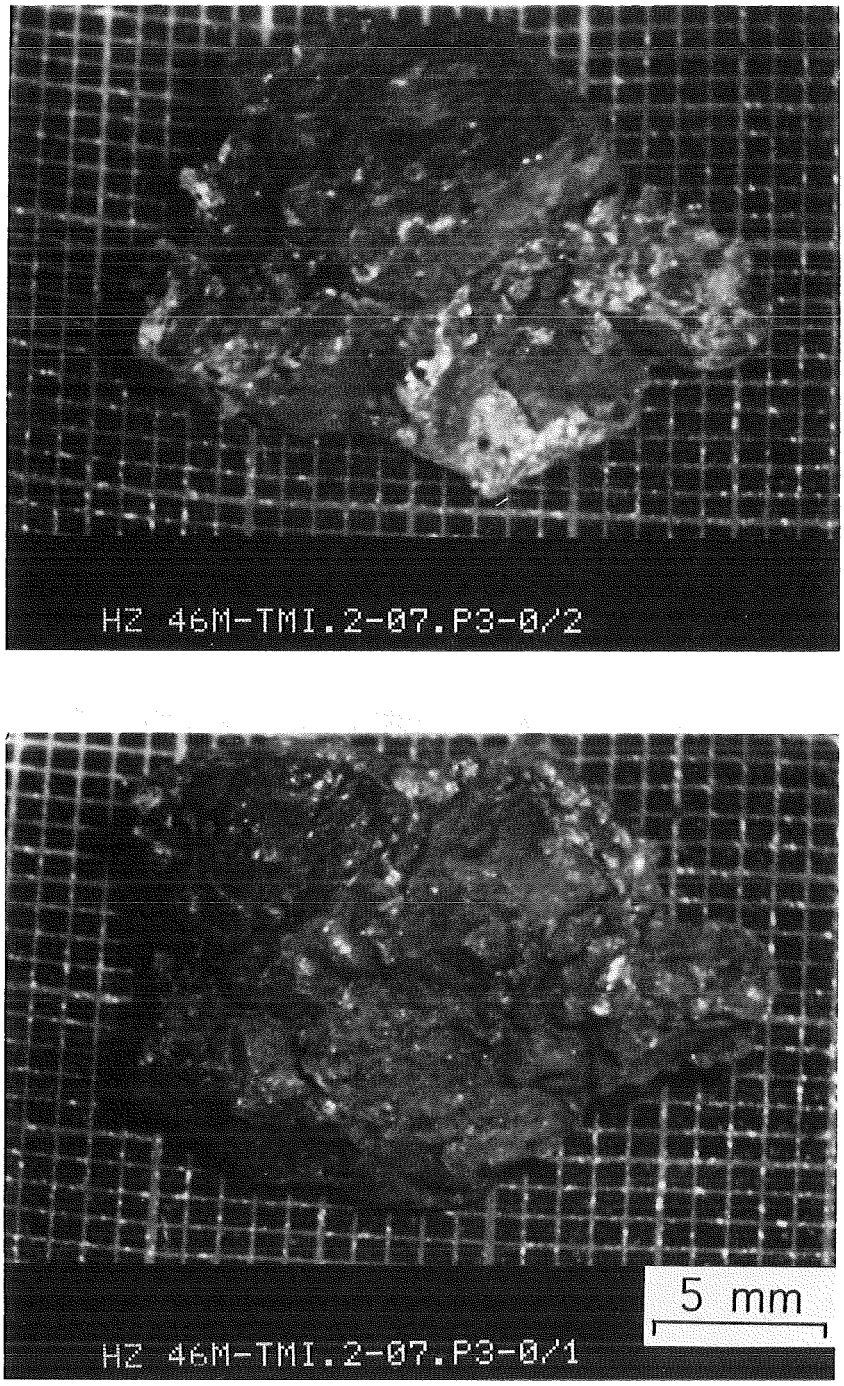

Fig. 30: View of an as-received piece of previously molten rock O7-P3, section A.

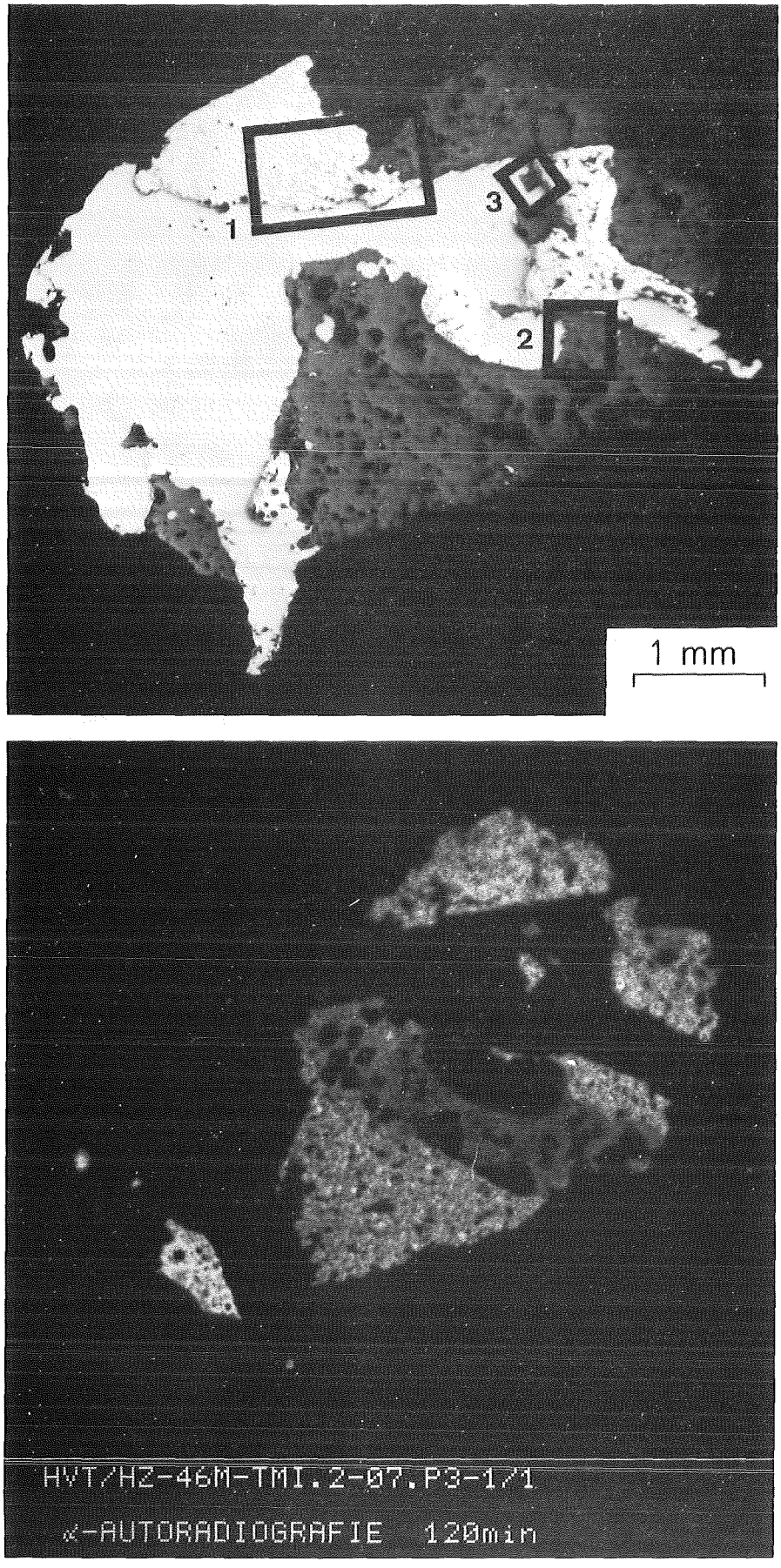

Fig. 31: Light-optical microstructure and α autoradiograph (exposure time 2 h) of rock O7-P3, section 1, showing two ceramic regions with different α activities and the analyzed positions 1, 2 and 3.

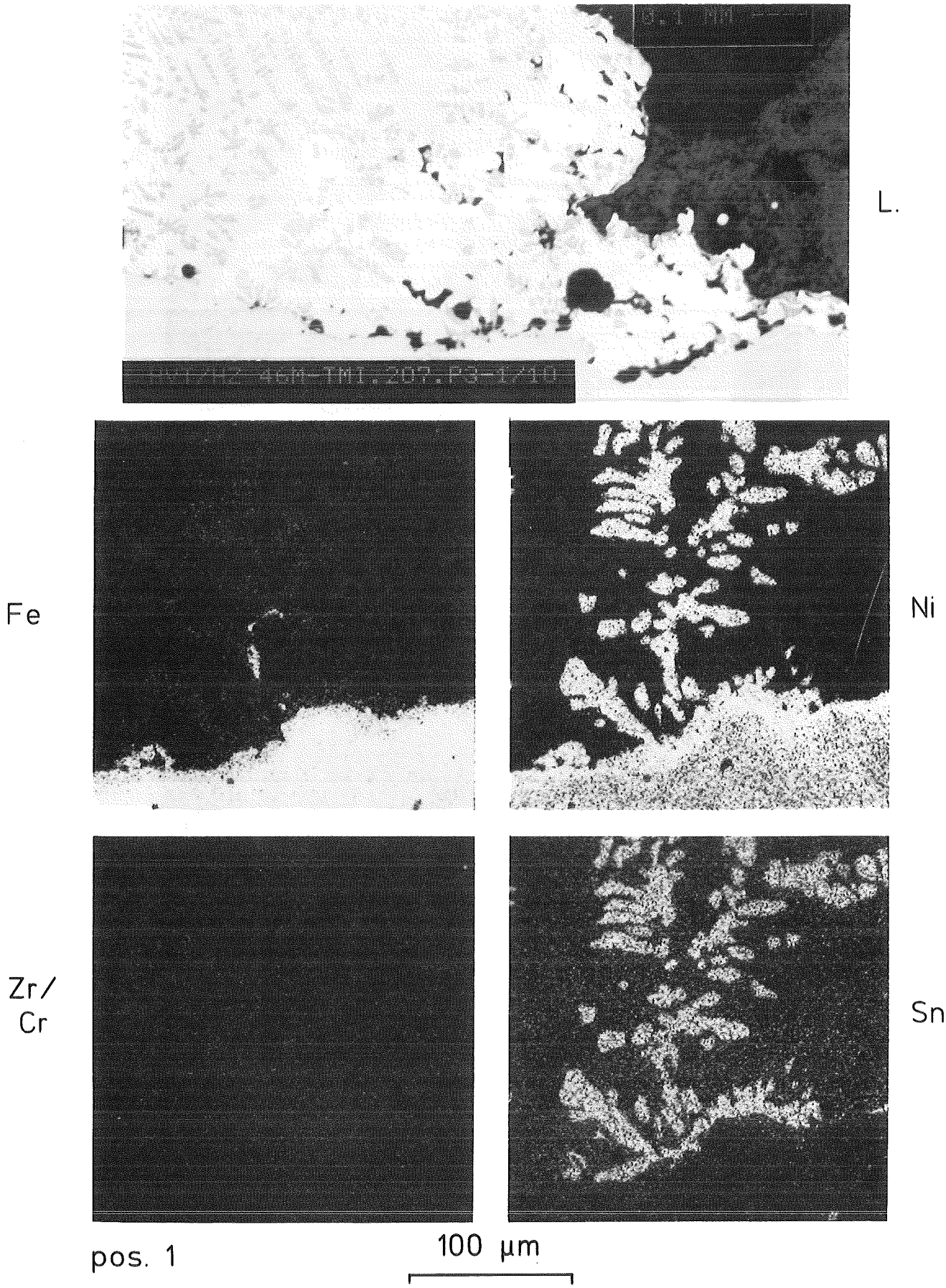

Fig. 32: Light-optical microstructure, absorbed electron images and Fe, Ni, Zr, Cr, Sn, Ag, Cd and In element distribution of rock O7-P3, section 1, position 1 (see fig. 31).

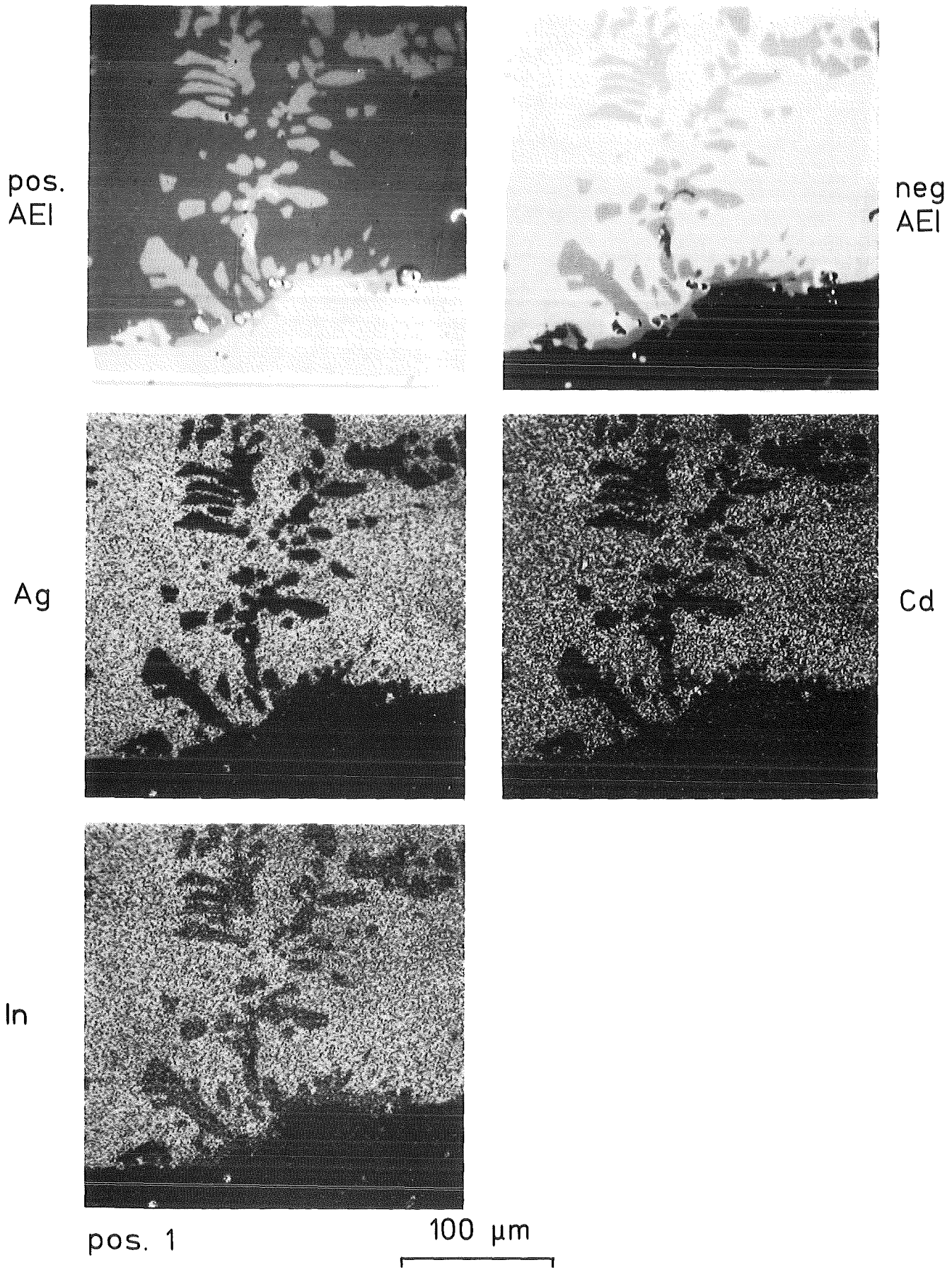

Fig. 32: continued.

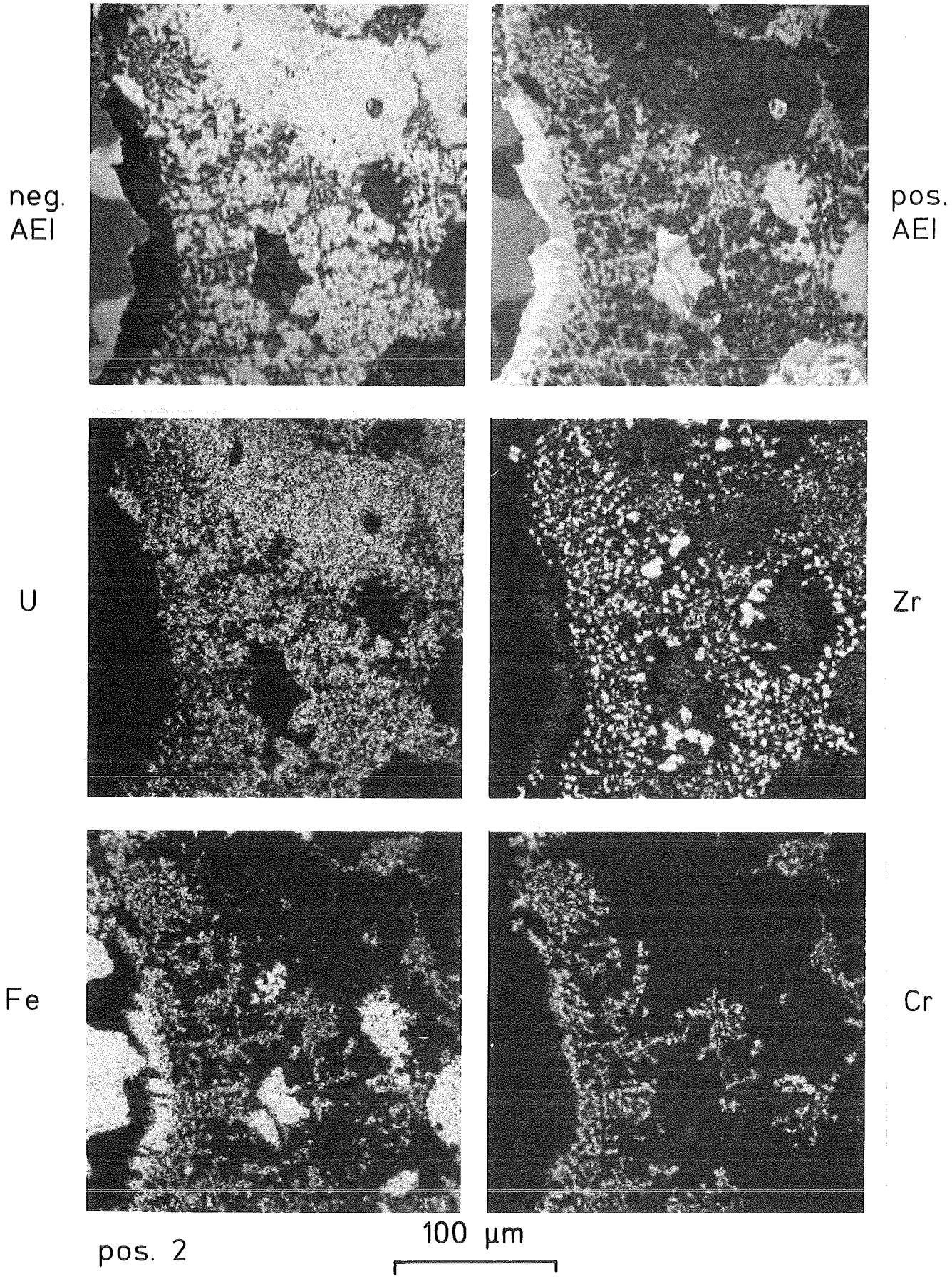

Fig. 33: Absorbed electron images and U, Zr, Fe, Cr, Ag, Cd, In, Ni, and Sn element distribution of rock O7-P3, section 1, position 2 (see fig. 31).

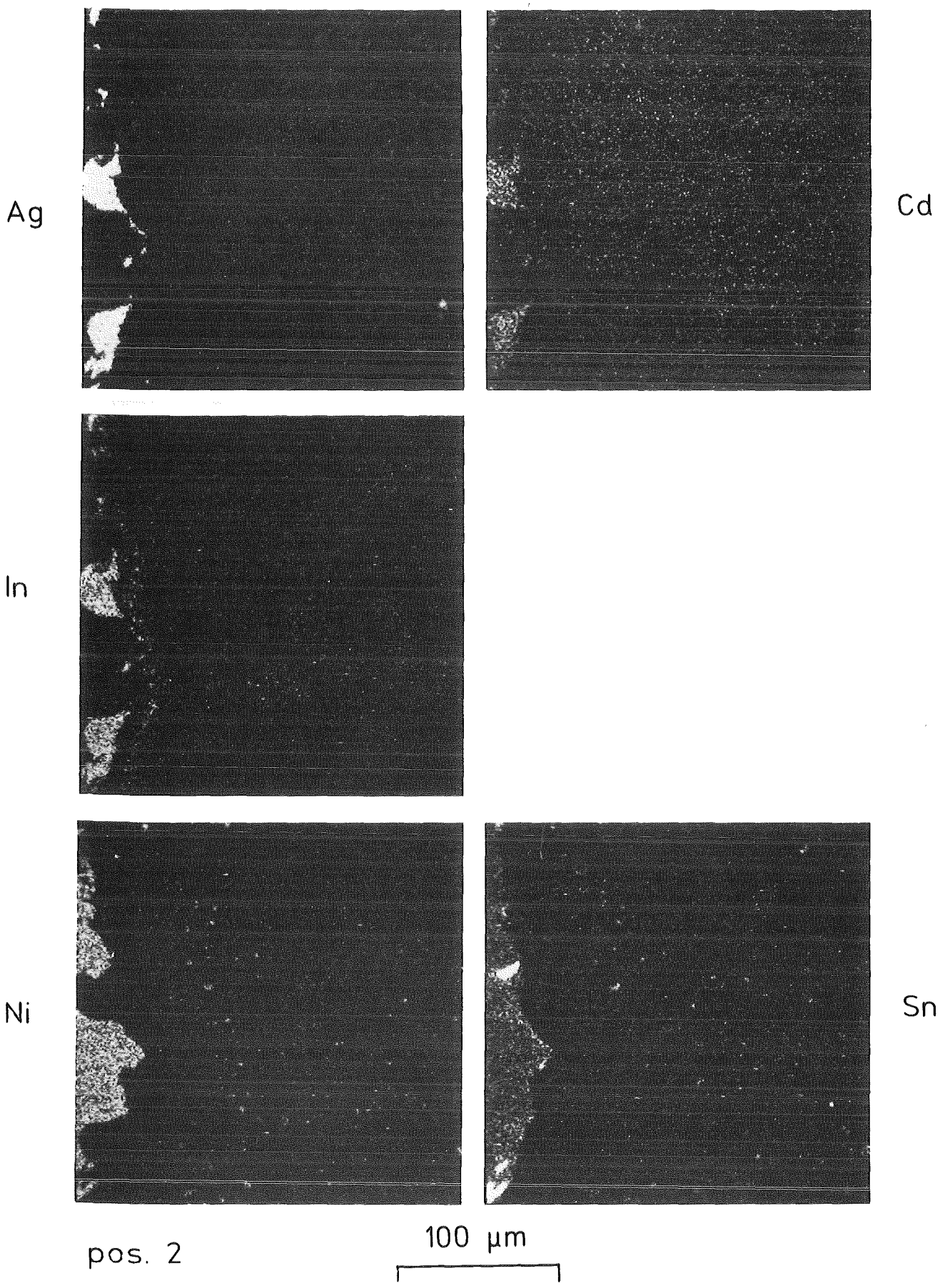

Fig. 33: continued.

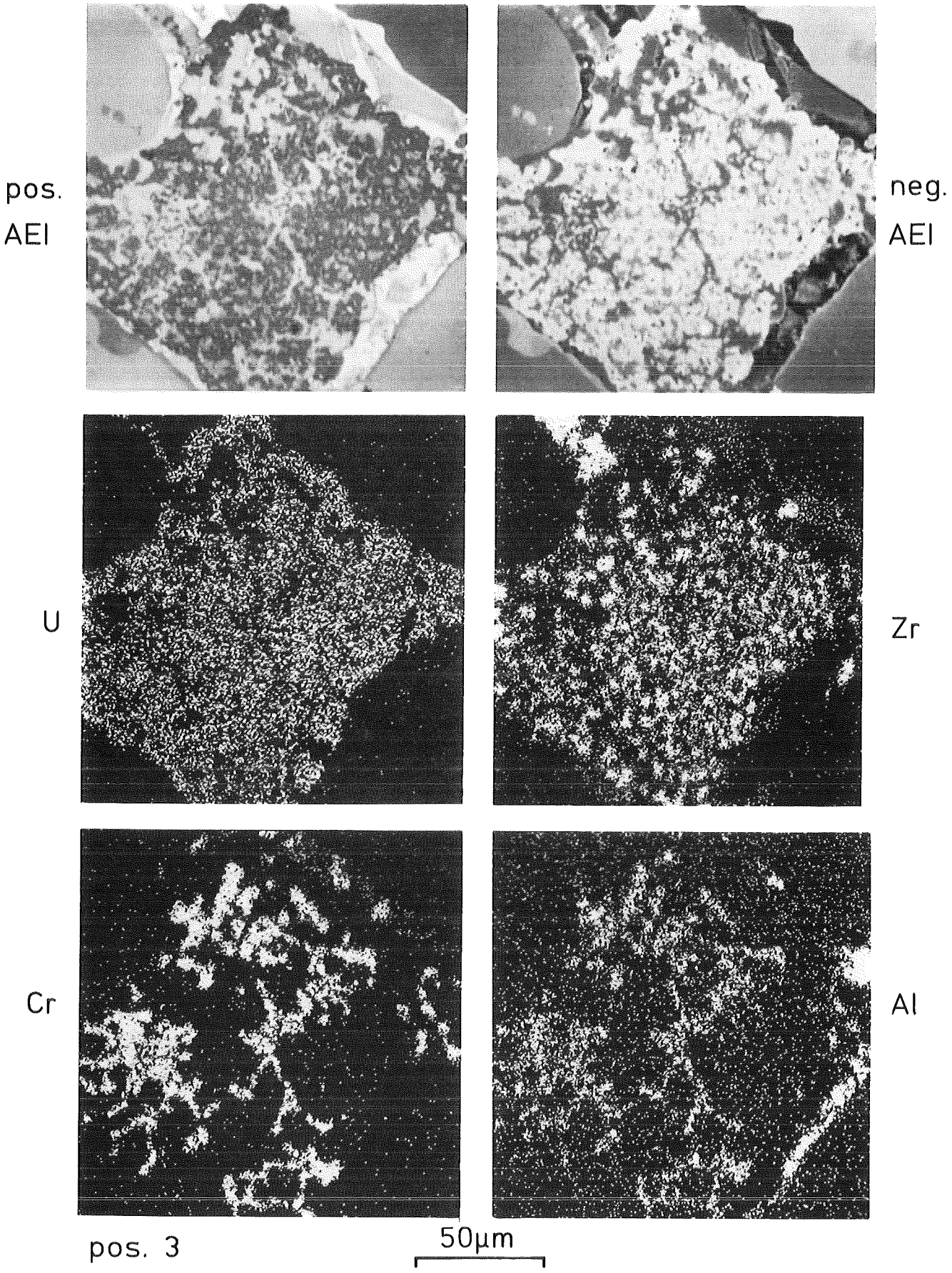

Fig. 34: Absorbed electron images and U, Zr, Cr, Ag, Al, Cd, Fe, Ni, O and Sn element distribution of rock O7-P3, section 1, position 3 (see fig. 31).

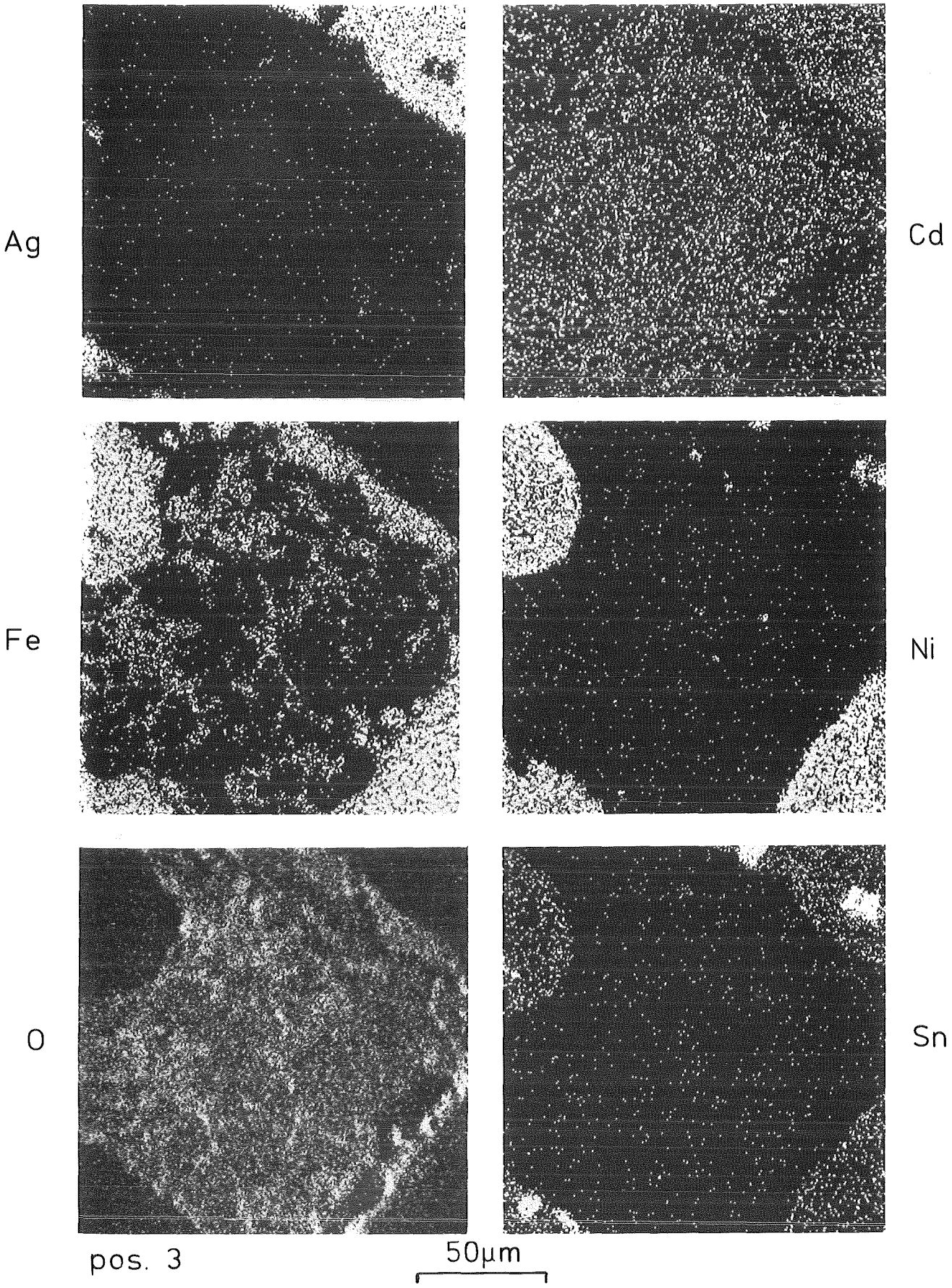

Fig. 34: continued.

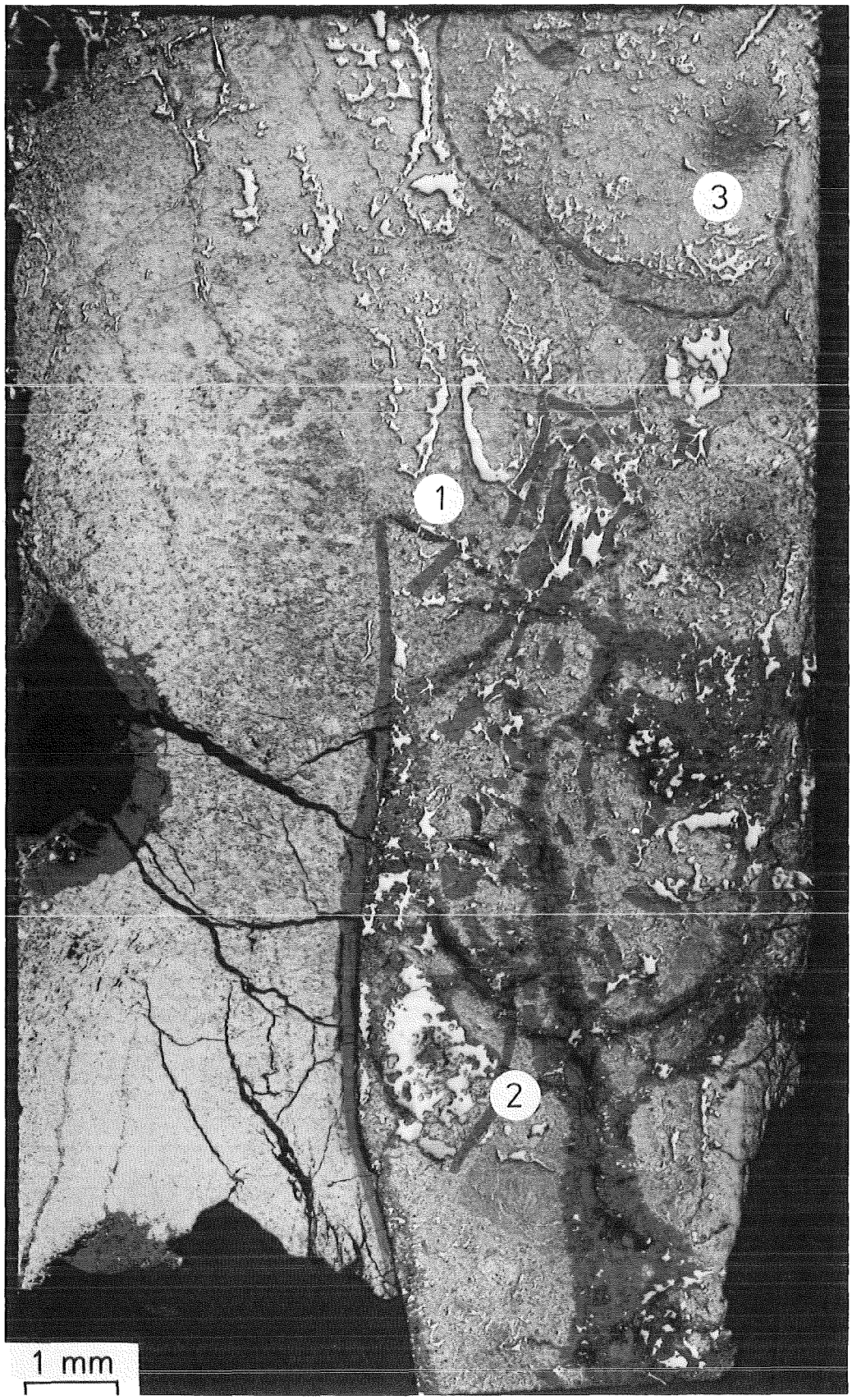

Fig. 35: Light-optical microstructure of loose core debris O7-P8, section B, showing oxidized Zircaloy lyers in a $(Zr,U)O_2$ matrix and the analyzed positions 1, 2 and 3.

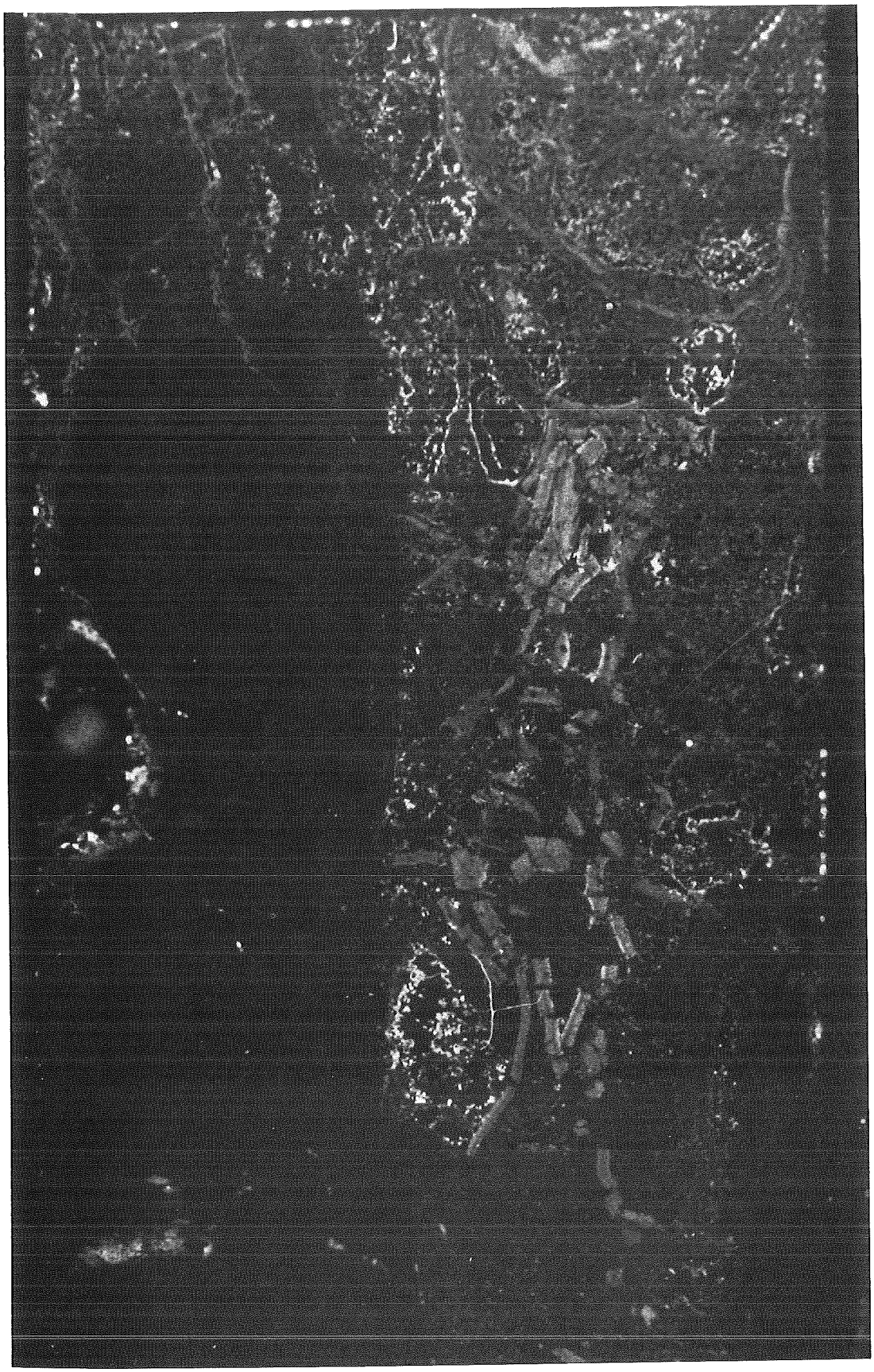

Fig. 36: α autoradiograph (3 h exposure time) of the sample in fig. 35.

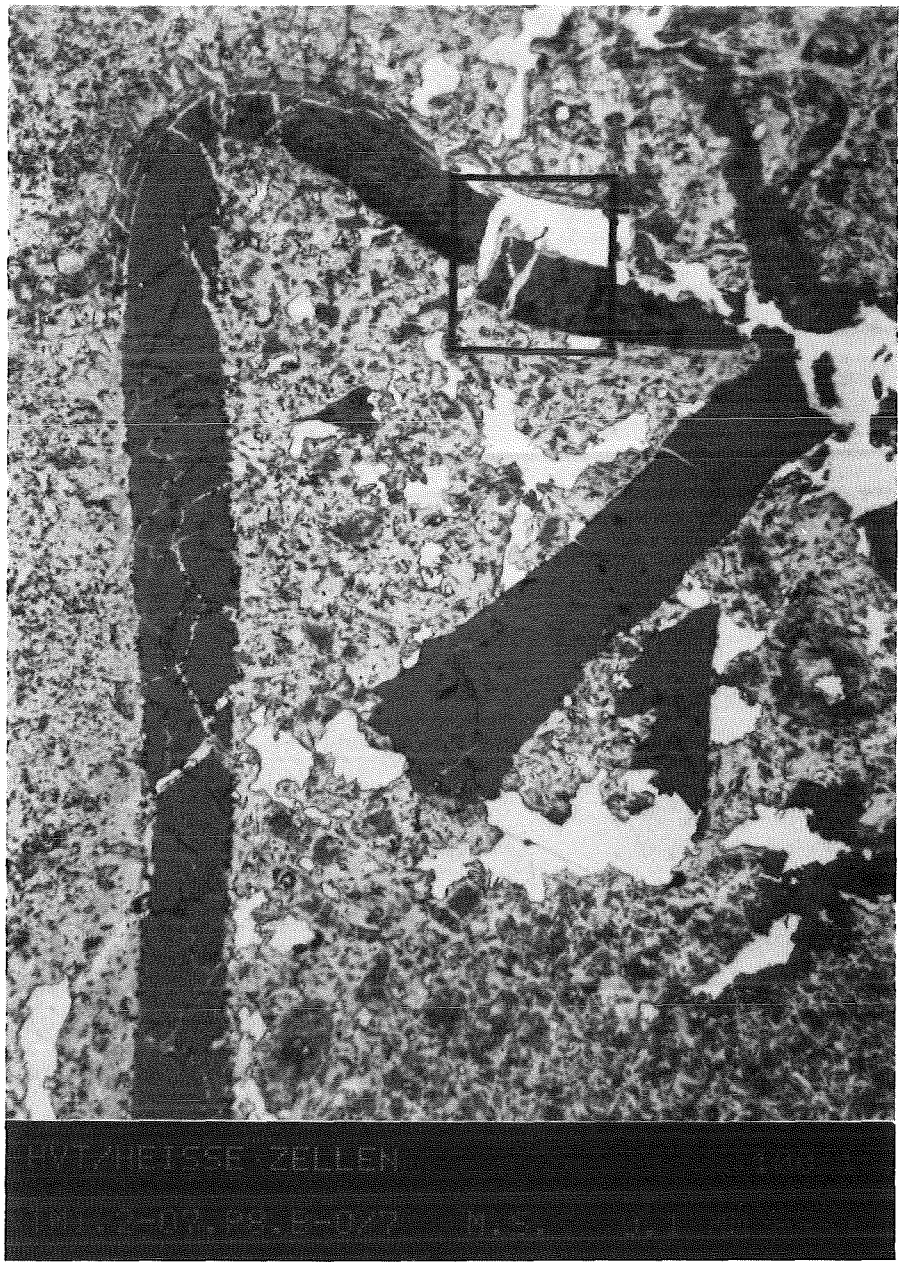

Fig. 37: Light-optical microstructure detail of loose core debris O7-P8, section B, position 1 in fig. 35; the frame refers to the analyzed area in fig. 38.

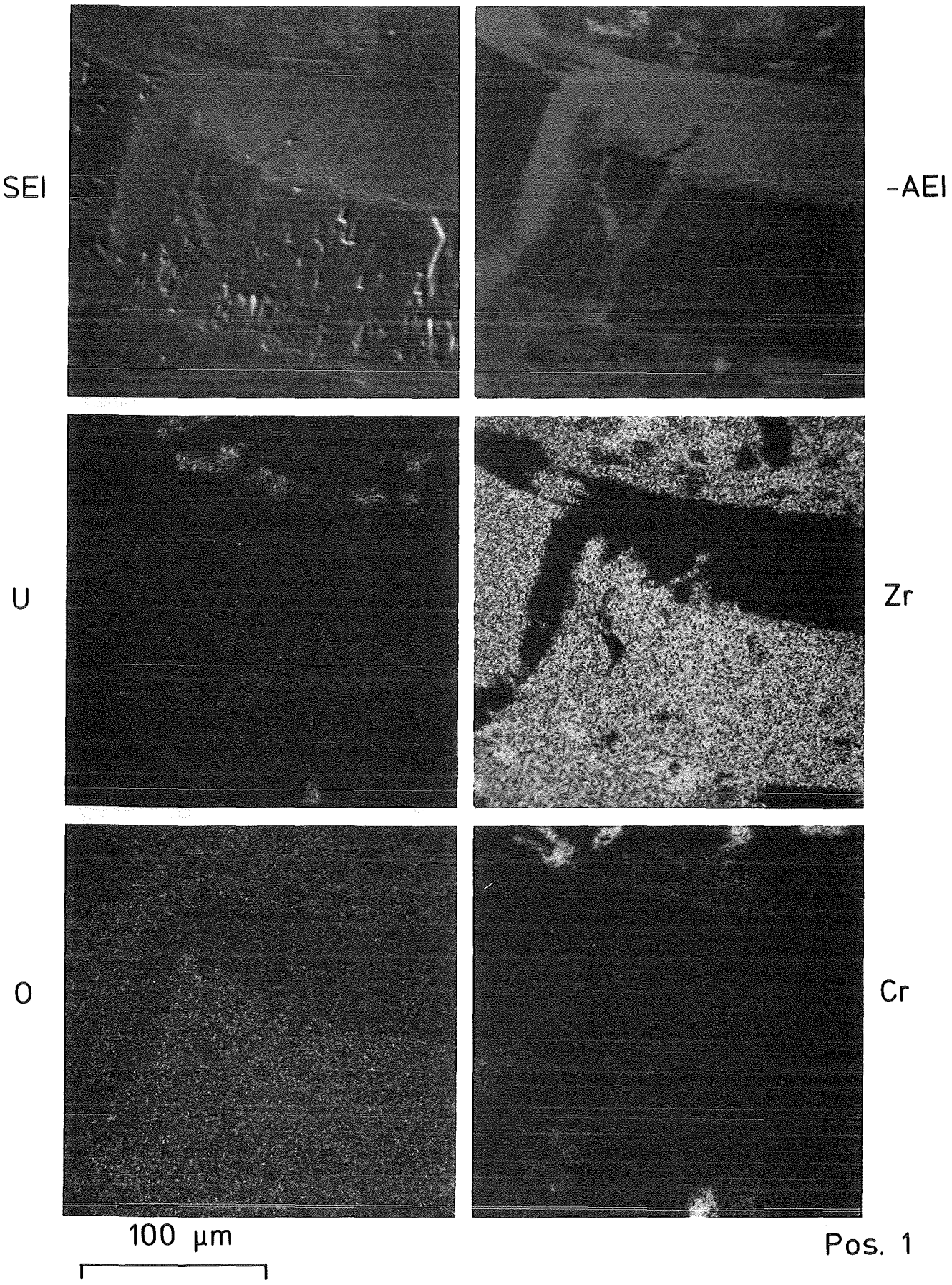

Fig. 38: Secondary and negative absorbed electron image and U, Zr, O, Cr, Ag, Cd, In, Sn, Ni and Fe element distribution of loose core debris O7-P8, section B, posistion 1 in fig. 35.

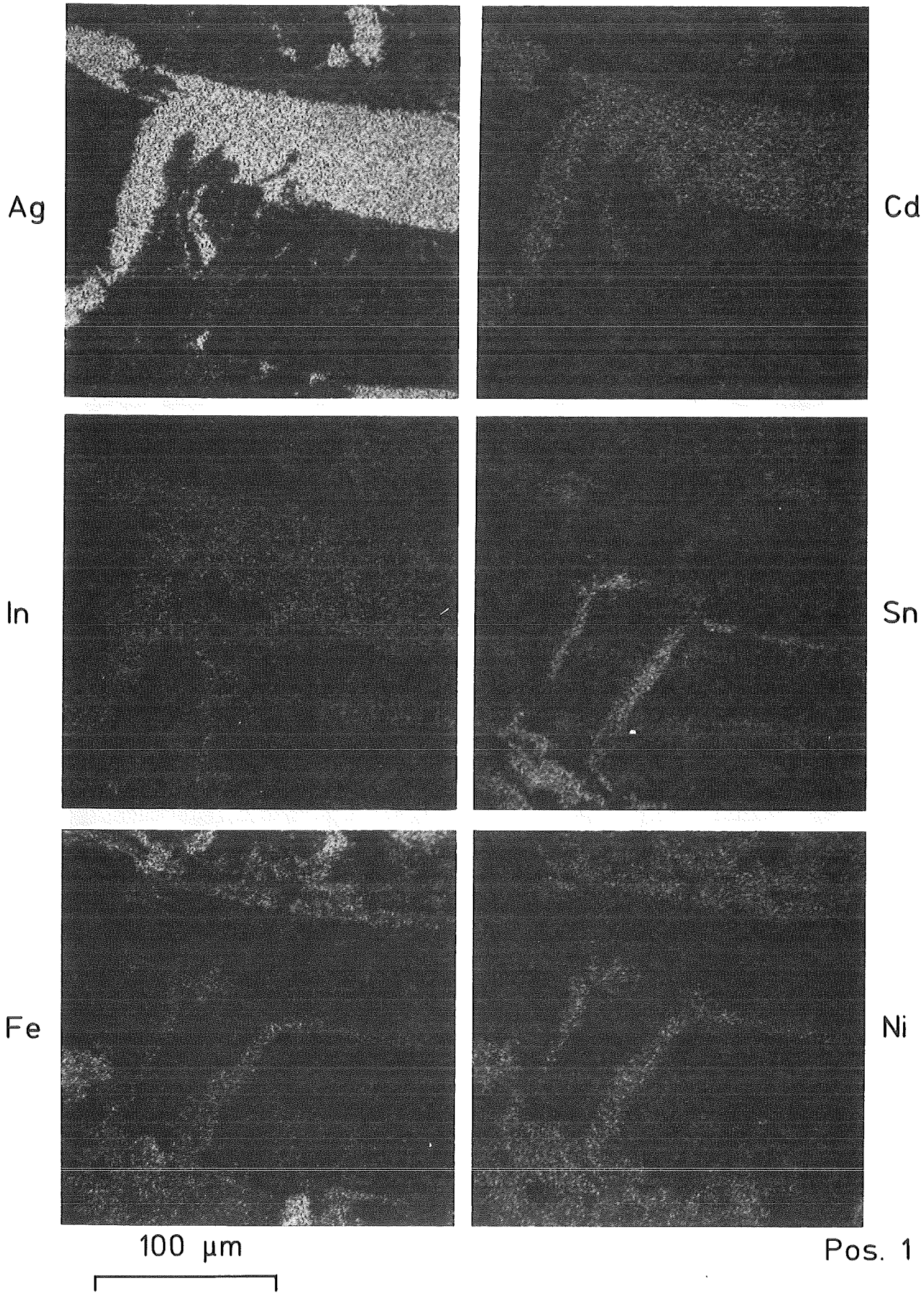

Fig. 38: continued.

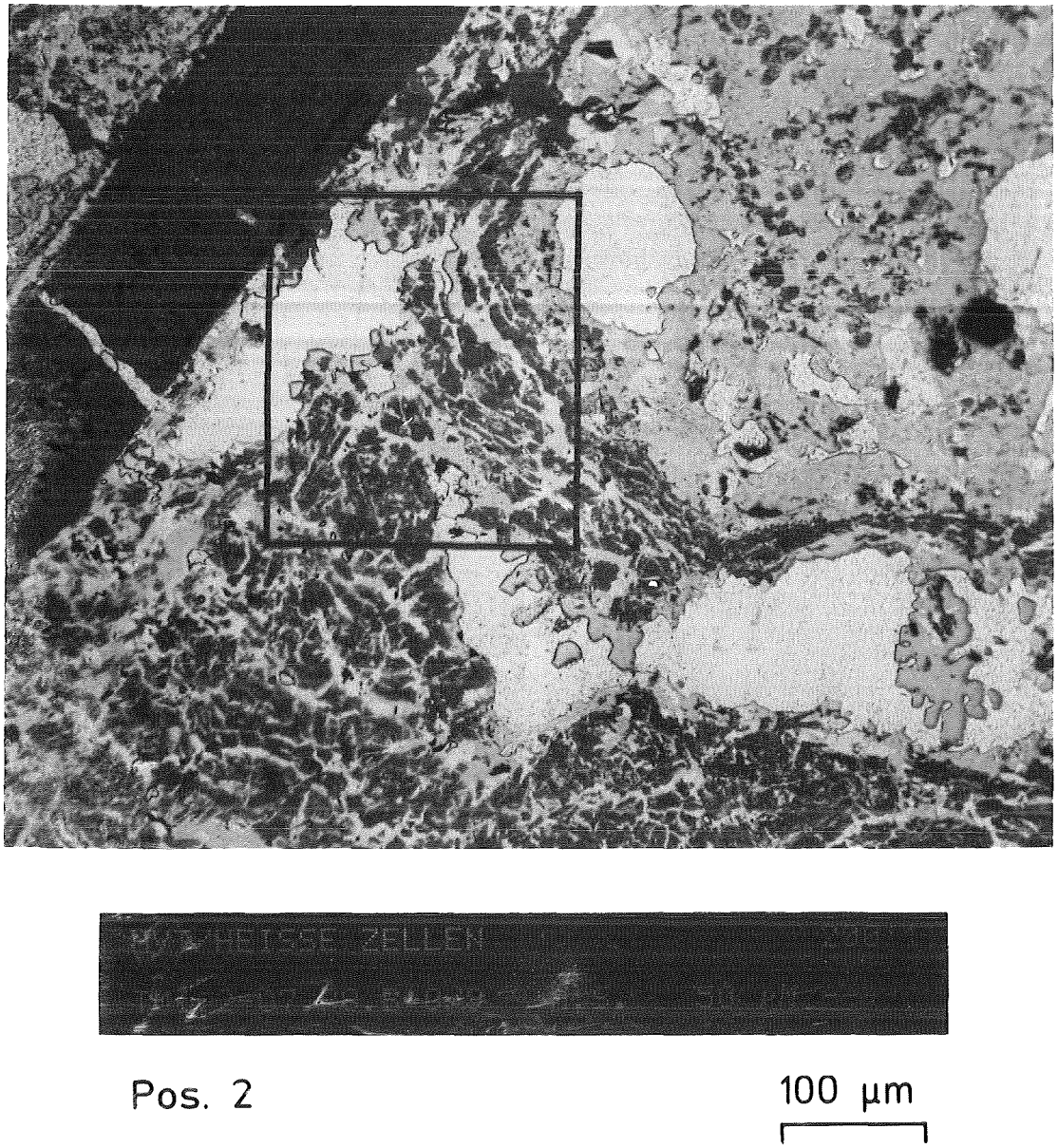

Fig. 39: Light-optical microstructure detail of loose core debris O7-P8, section B, position 2 in fig. 35; the frame refers to the analyzed area in fig. 40.

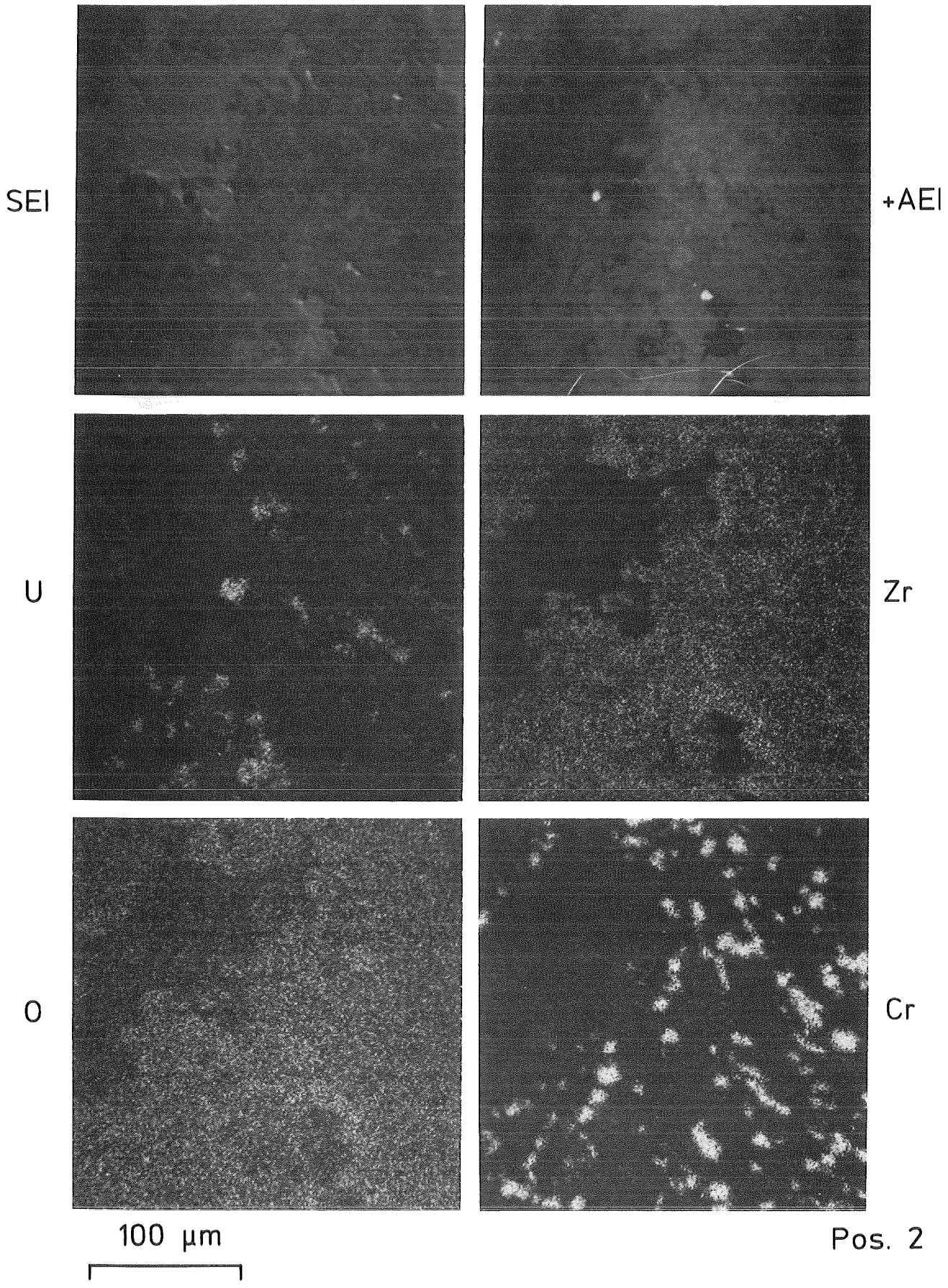

Fig. 40: Secondary and absorbed electron image and U, Zr, O, Cr, Ag, Cd, In, Sn, Ni and Fe element distribution of loose core debris O7-P8, section B, posistion 2 in fig. 35.

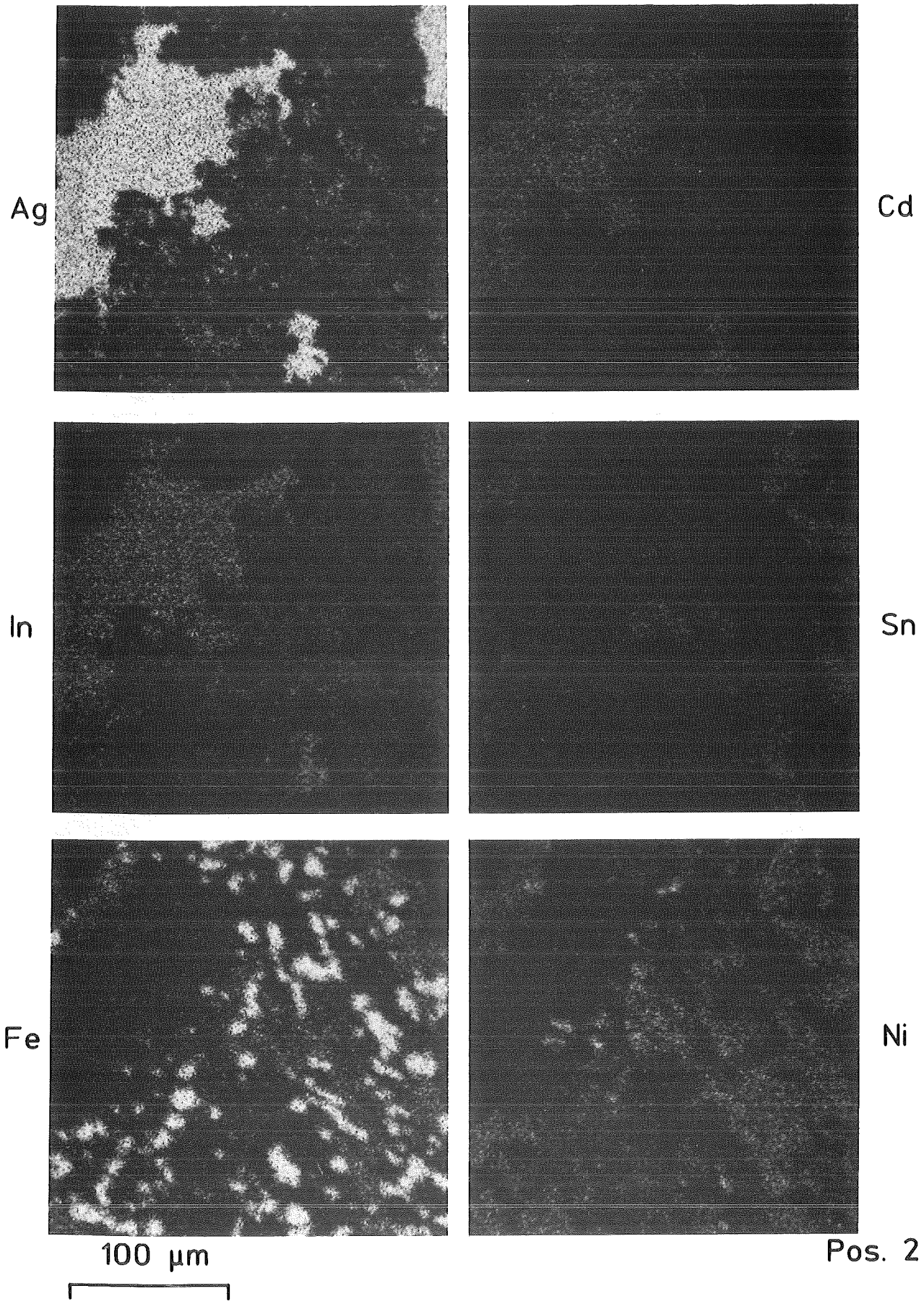

Fig. 40: continued.

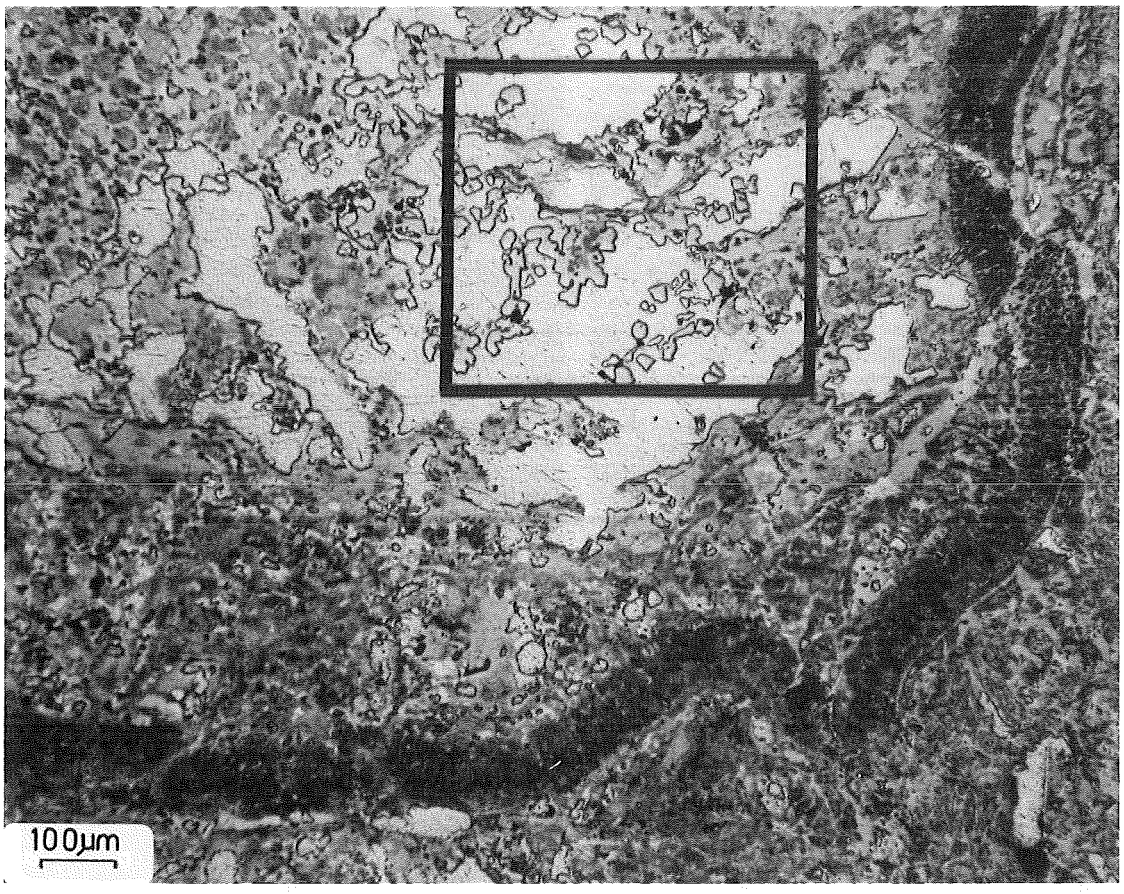

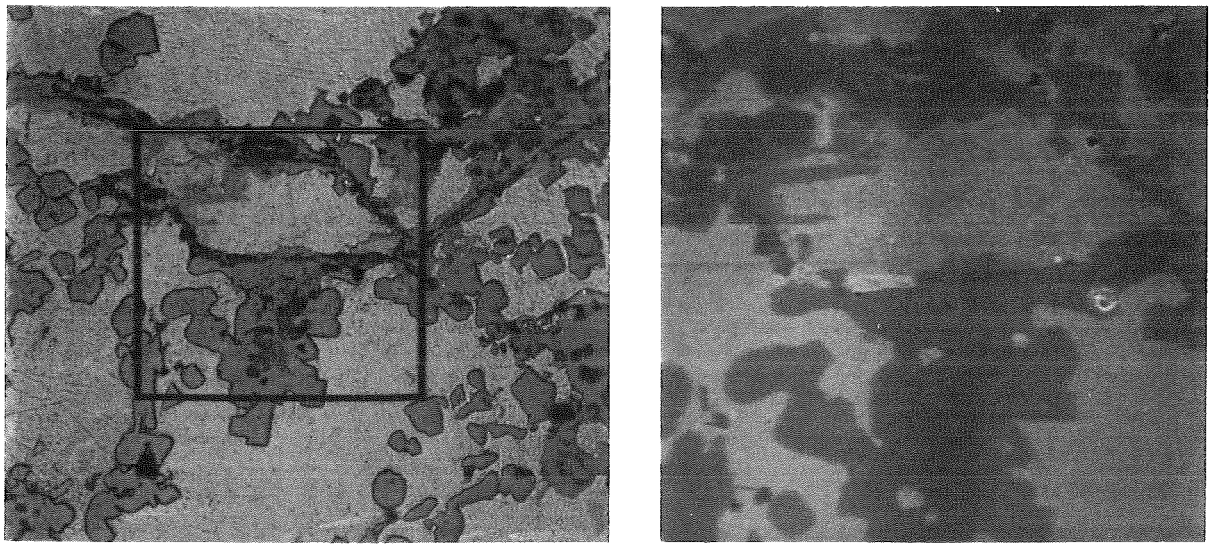

Fig. 41. Light-optical microstructure and negative absorbed electron image of loose core debris O7-P8, section B, position 2 in fig. 35; the frame refers to the analyzed area in fig. 42.

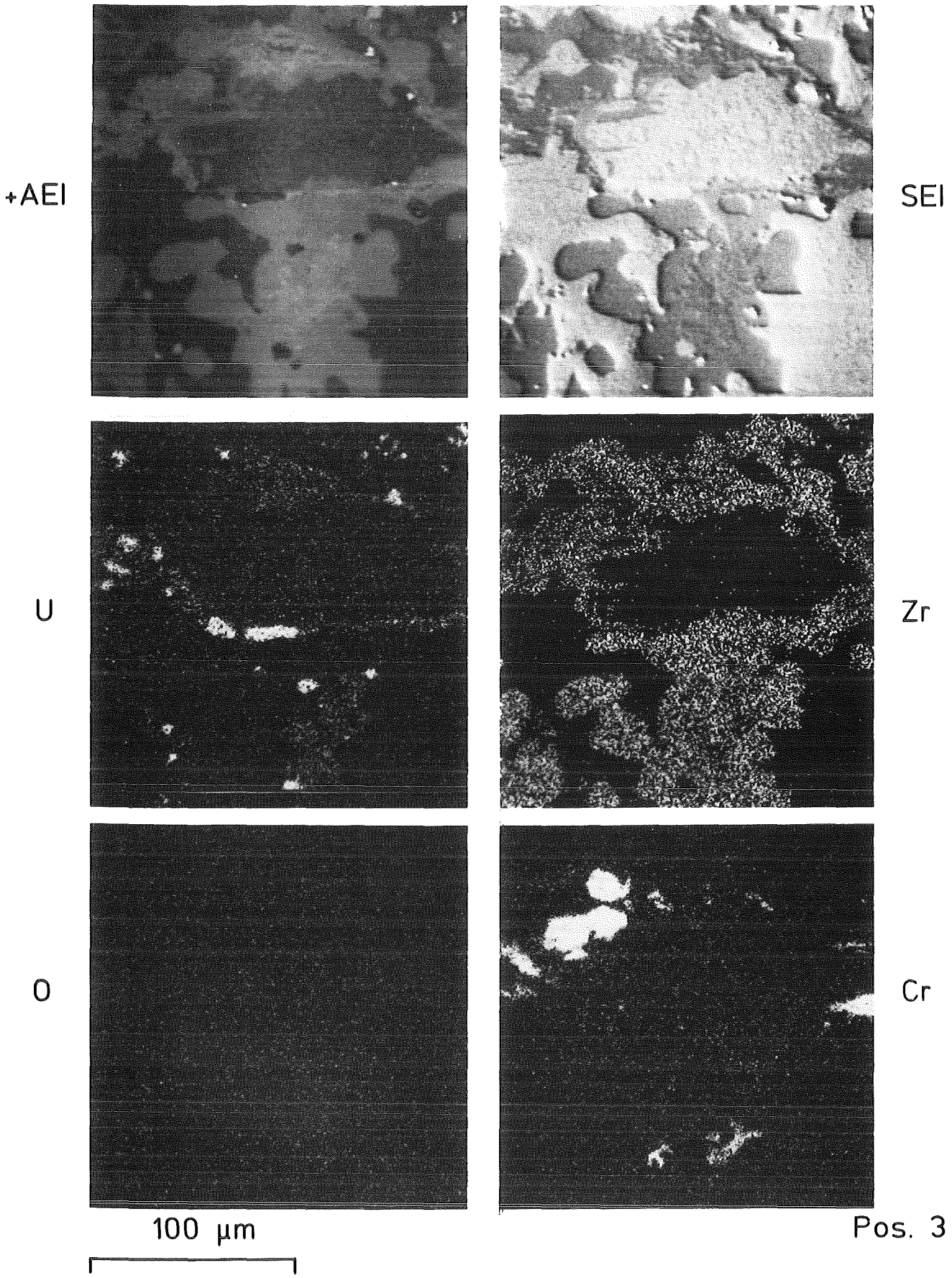

Fig. 42: Positive absorbed electron and secondary electron image and U, Zr, O, Cr, Ag, Cd, In, Sn, Fe and Ni element distribution of loose core debris O7-P8, section B, position 3 in fig. 35.

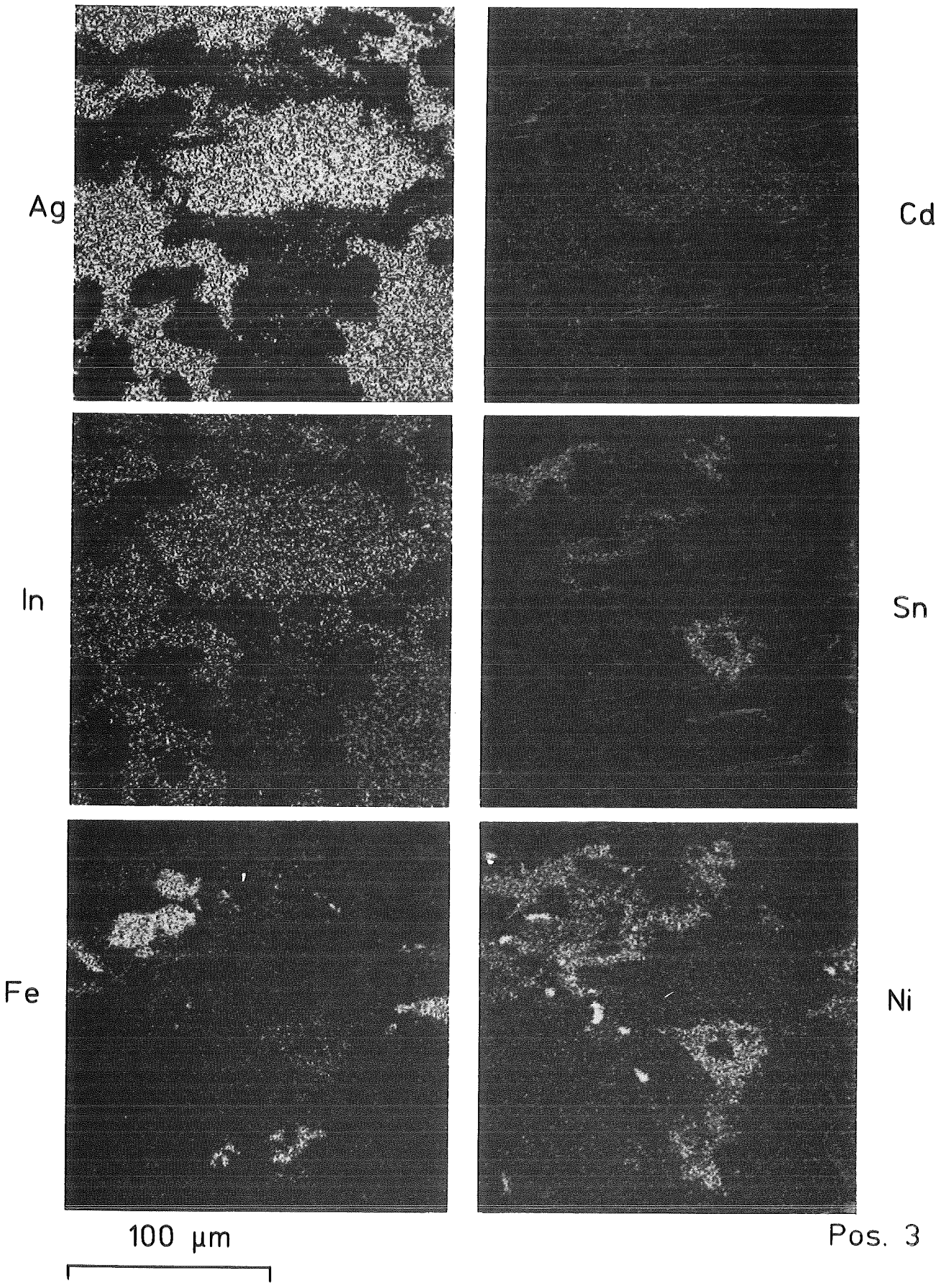

Fig. 42: continued.

Appendix: Constitution diagrams

The constitution diagrams given in Fig. A to J are based on experimental results from the literature and on calculations and estimations as well as on unpublished experimental work of one of the authors.

A. The Fe-Ni-Zr system

The isothermal section of the Fe-Ni-Zr system at 1000 °C in fig. A was estimated from the well-known phase diagrams of the binary Fe-Ni, Fe-Zr and Ni-Zr systems [1], as well as from the isothermal sections between 700 and 900 °C and the solidus surface of the Zr apex of the ternary Fe-Ni-Zr system [2]. Further information was used on the solubility of "$ZrNi_2$" in the cubic $MgCu_2$ type $ZrFe_2$ Laves phase [3]. A ternary eutectic was stated at 930 °C for the compositoin 73 at.% Zr - 22 at.% Fe - 5 at.% Ni.

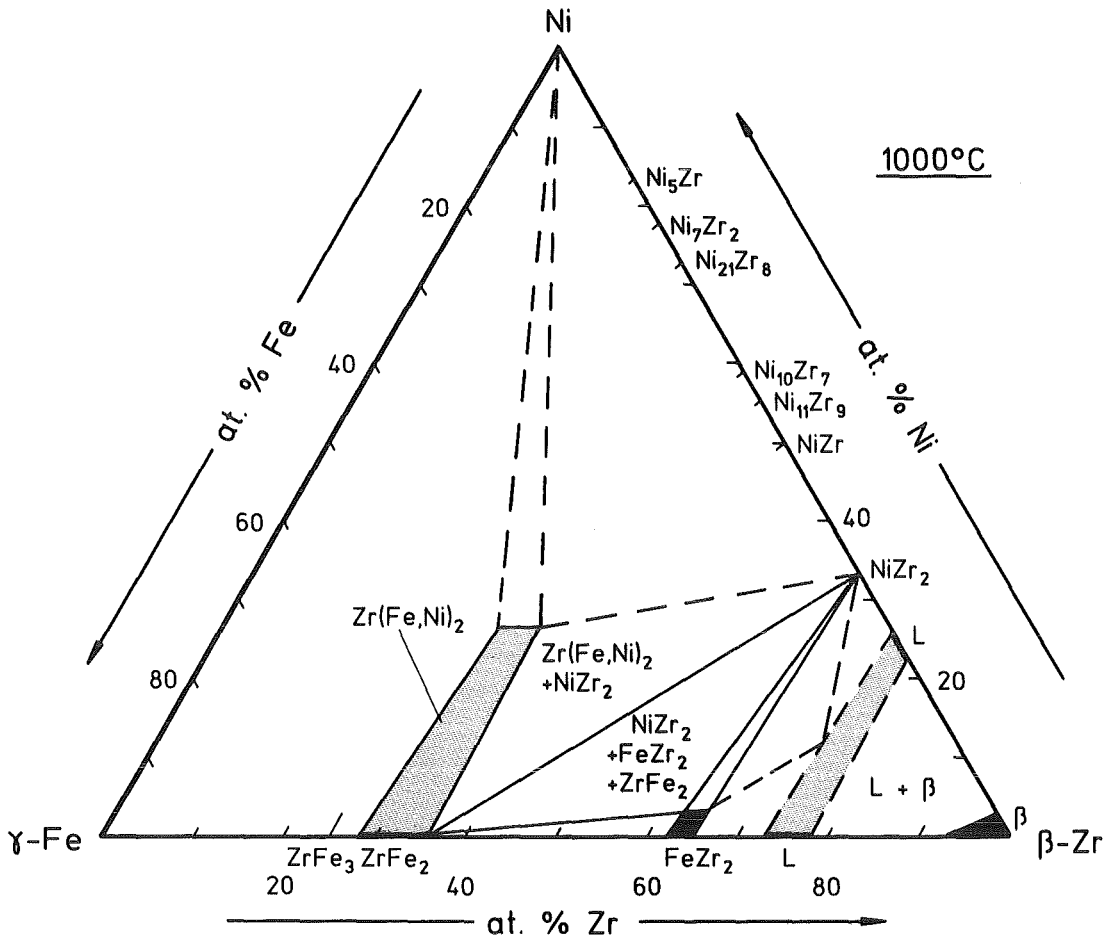

Fig. A: Tentative isothermal section of the Fe-Zr-Ni system at 1000 °C.

B. The Fe-Cr-Zr sytem

The isothermal section of the Fe-Cr-Zr system at 1000 °C in fig. B was constructed on the basis of the well-known phase diagrams of the binary Fe-Cr, Fe-Zr and Cr-Zr systems [1]. Further information is given by the isothermal section at 1000 °C and by the solidus surface of the ternary Fe-Cr-Zr system [4], by the concentration section of the pseudobinary $Fe_{0.98}Cr_{0.02}$-Zr system [4] and by the phase diagram of the pseudobinary $ZrFe_2$-$ZrCr_2$ system [5]. The hexagonal $MgZn_2$ type $ZrCr_2$ Laves phase exists below 1150 °C. The Fe rich cubic ε-$Zr(Cr,Fe)_2$ solid solution range is deflected towards the $ZrFe_3$ direction in the ternary system.

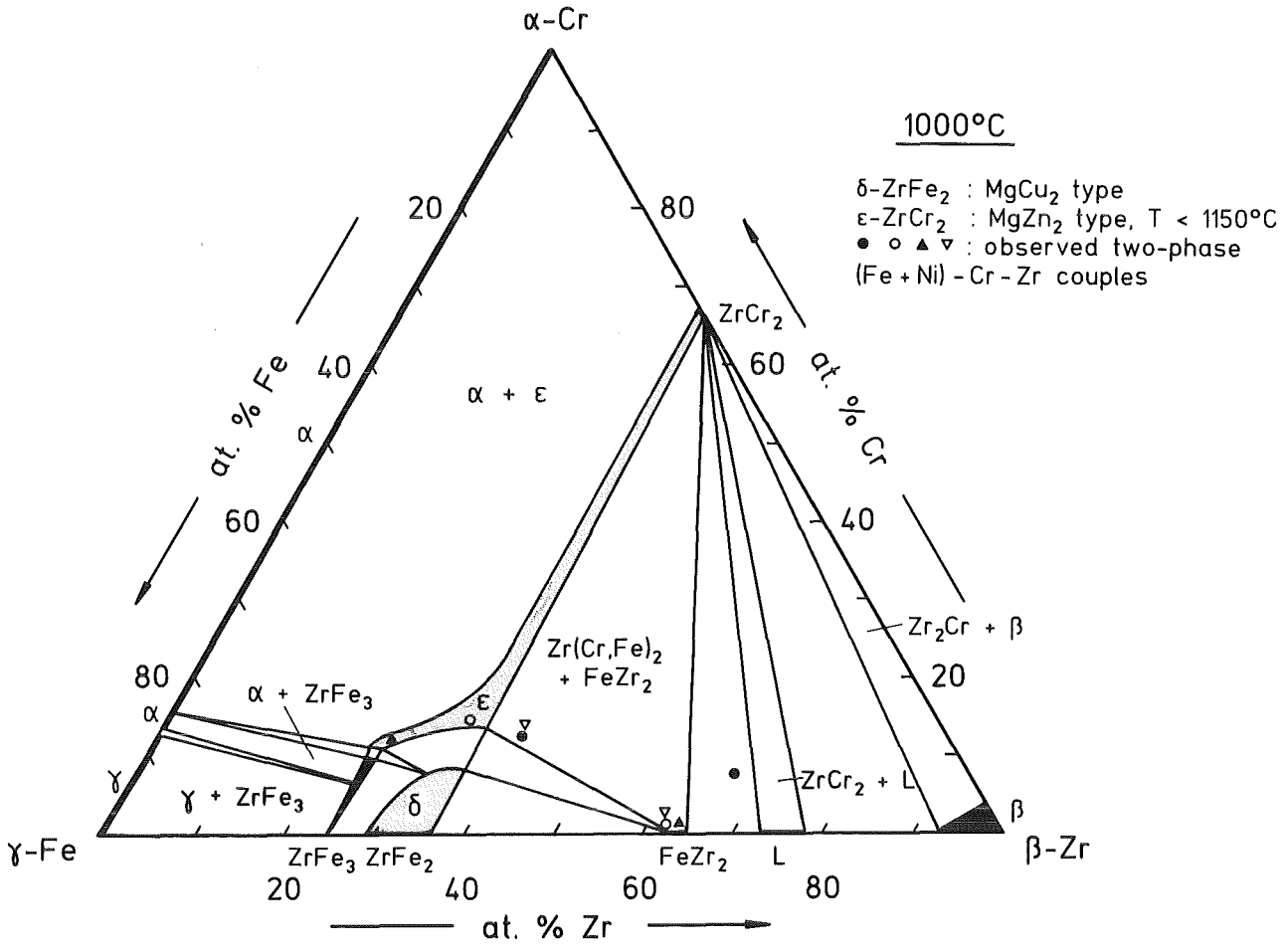

Fig. B: Tentative isothermal section of the Fe-Zr-Cr system at 1000 °C.

C. The Fe-Zr-O system

The isothermal section of the Fe-Zr-O system at 1000 °C in fig. C was investigated by [6] in the Fe-Zr near region with emphasis to the oxygen stabilized cubic η-carbide type Zr_6Fe_3O phase. It is probably separated by a two-phase field from the tetragonal Al_2Cu type $FeZr_2$ phase which is drawn in fig. C at variance of the phase field distribution in [6]. A homogeneity range is assumed in the Zr-Fe and O-(Zr + Fe) directions [7]. Monoclinic ZrO_2 can dissolve up to 21.2 mol% Fe_2O_3 [8]. The maximum solubility corresponds to the formula $Zr_{0.65}Fe_{0.35}O_{1.82}$. This results in a two-phase field $(Zr,Fe)O_{2-x}$-Fe_3O_4 in the ternary Fe-Zr-O system. ZrO_2 and Fe_2O_3 form a cubic solid solution $Zr_{1-x}Fe_xO_{2-x}$ up to x = 0.39 at temperatures above 1900 °C [9].

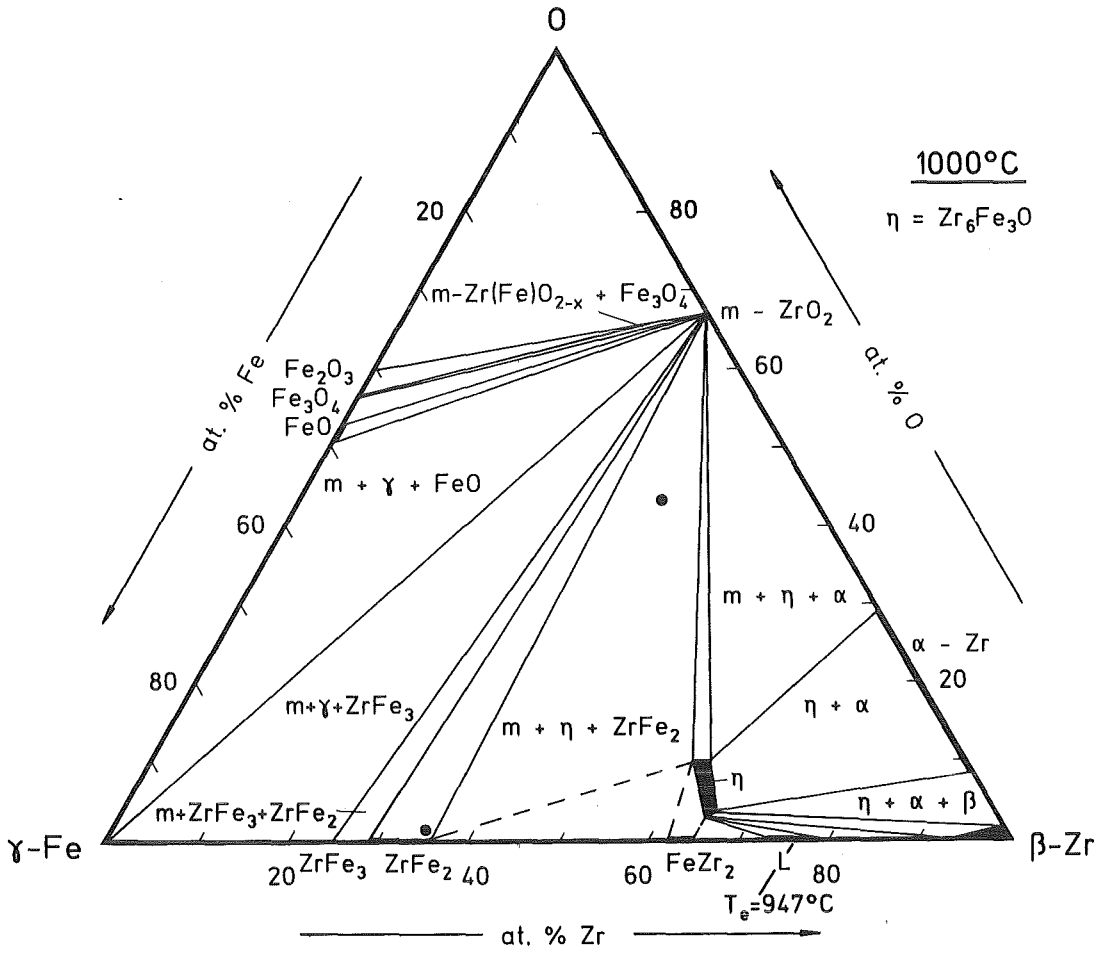

Fig. C: Isothermal section of the Fe-Zr-O system at 1000 °C.

D. The Cr-Zr-O system

The isothermal section of the Cr-Zr-O system at 1200 °C in fig. D. originates from the work given in [10]. The ternary system is characterized by the oxygen stabilized cubic η-carbide type Zr_3Cr_3O phase.

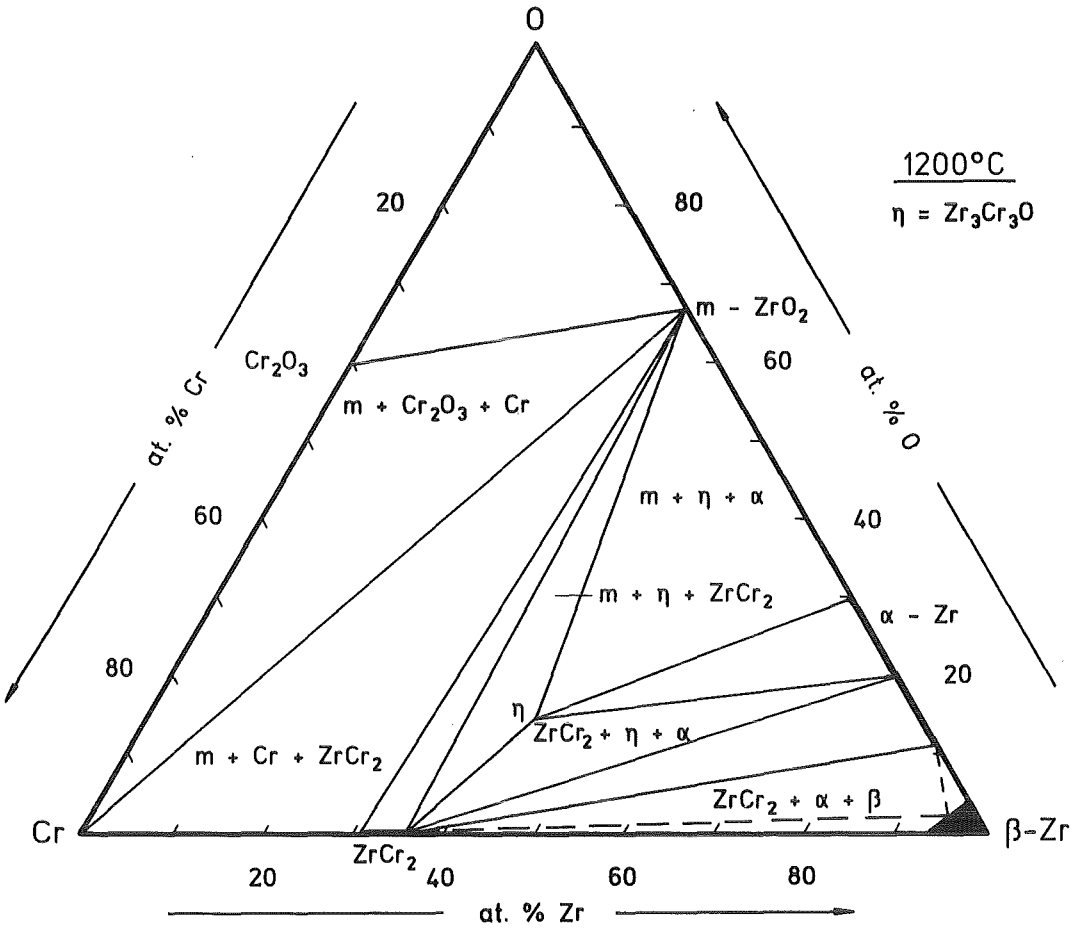

Fig. D: Isothermal section of the Cr-Zr-O system at 1000 °C.

E. The Ag-Cd-In system

The isothermal section of the Ag-Cd-In system at 315 °C in fig. E was taken from [11] and was complemented by the hexagonal ζ-Ag_3In-AgCd solid solution range. The initial composition of the fcc. absorber material is 80.9 at.% Ag - 4.9 at.% Cd - 14.2 at.% In; it is marked by a black dot in fig. E. The solidus temperature of this composition is about 760 °C.

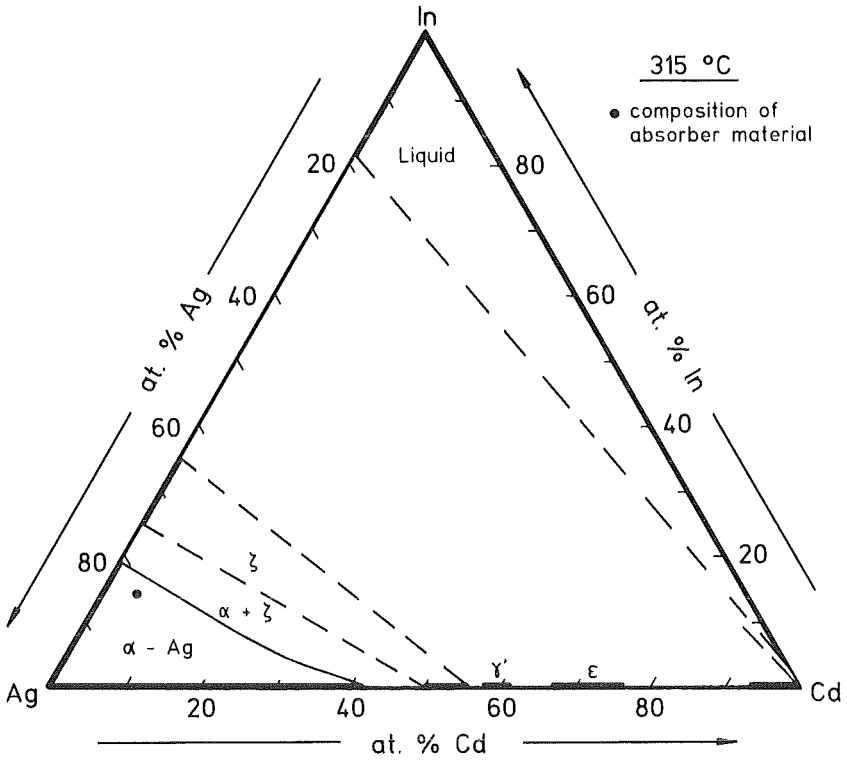

Fig. E: Isothermal section of the Ag-Cd-In system at 315 °C.

F. The pseudobinary UO_2-Zr system

As UO_2 and oxygen free Zr are not in thermodynamic equilibrium the construction of the phase diagram in fig. F is difficult on the basis of the experimental information [12,13]. The tie lines are not parallel to the drawing plane. It is concluded that a liquid phase appears above 1300 °C and the liquid exists exclusively above 2150 °C for concentrations higher than 42 at.% Zr.

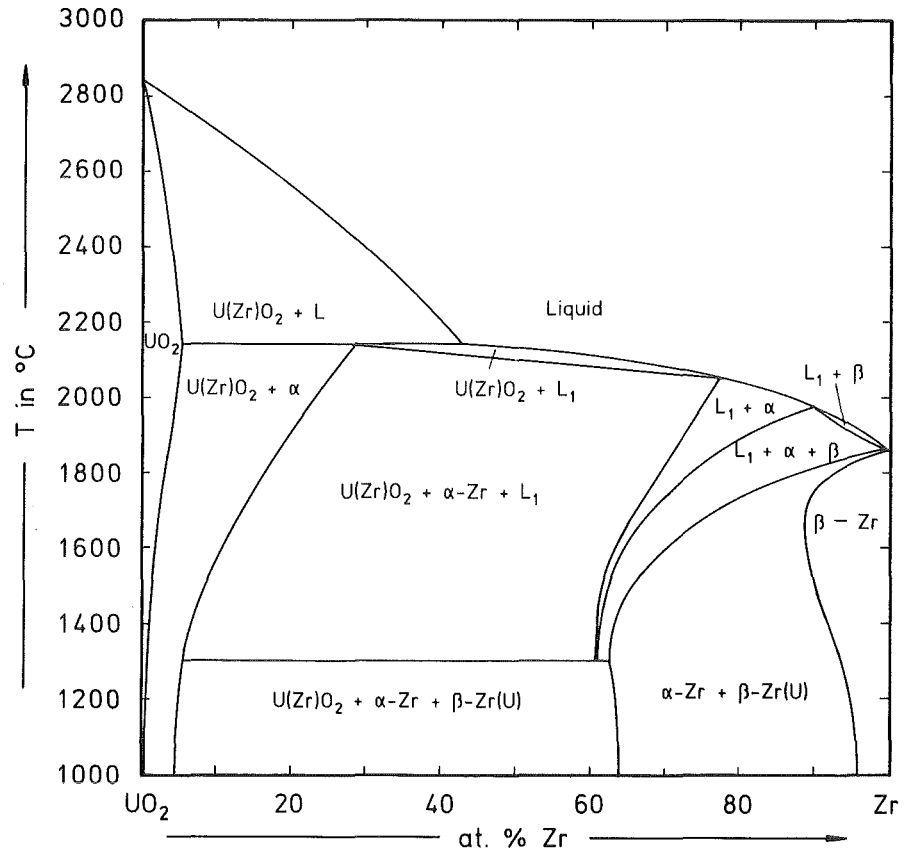

Fig. F: Tentative phase diagram of the pseudobinary UO_2-Zr system sectioning oxygen free zirconium and UO_2.

G./H. The UO_2-ZrO_2 system

There are at least eight different phase diagrams of the binary UO_2-ZrO_2 system. The phase diagram of Romberger et al. [14] in fig. G seems to be the most reliable one. The melting point minimum of the cubic $(U,Zr)O_2$ solid solution was observed at 2550 °C. The maximum solubility of ZrO_2 in UO_2 and UO_2 in ZrO_2 was confirmed at 1700 °C by measurements in [15]. The phase diagram is complemented by room temperature lattice parameters of the cubic $(U,Zr)O_2$ and tetragonal $(Zr,U)O_2$ solid solutions annealed at 1700 °C, see fig. H [15].

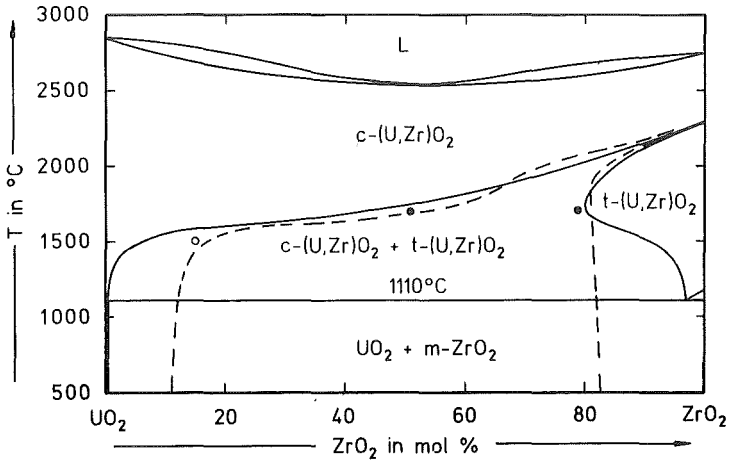

Fig. G: Phase diagram of the pseudobinary UO_2-ZrO_2 system.

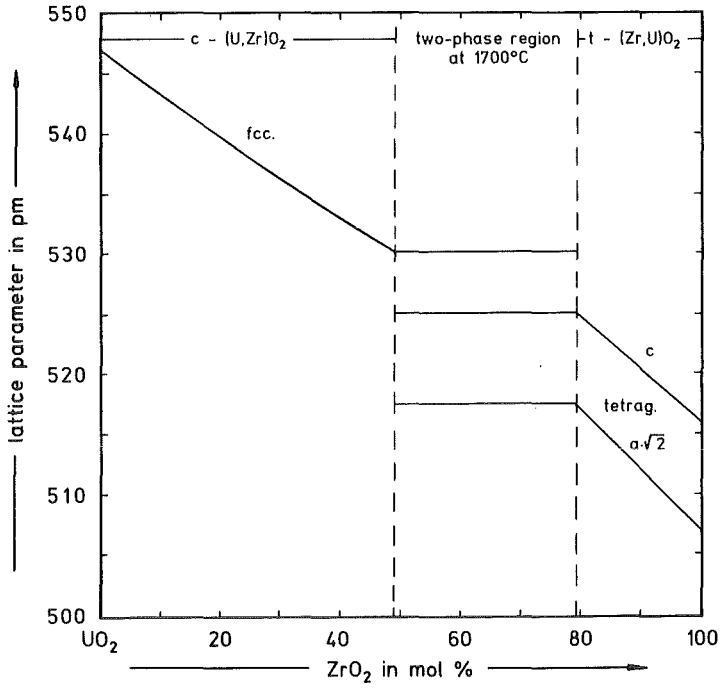

Fig. H: Lattice parameters of the cubic $(U,Zr)O_2$ and tetragonal $(Zr,U)O_2$ solid solutions; phase boundaries for 1700 °C.

I. The $FeO-Cr_2O_3-Al_2O_3$ system

The isothermal section of the pseudoternary $FeO-Cr_2O_3-Al_2O_3$ system at 1760 °C in fig. I is taken from [16]. The compositions are given in wt.%. The black dot in the $Fe(Al,Cr)_2O_4$ single-phase field illustrates the observed $Fe(Cr,Ni,Zr)_{1.4}Al_{0.6}O_4$ composition of the spinel in the lower plenum. The estimated solidus temperature of this composition is 2000 °C.

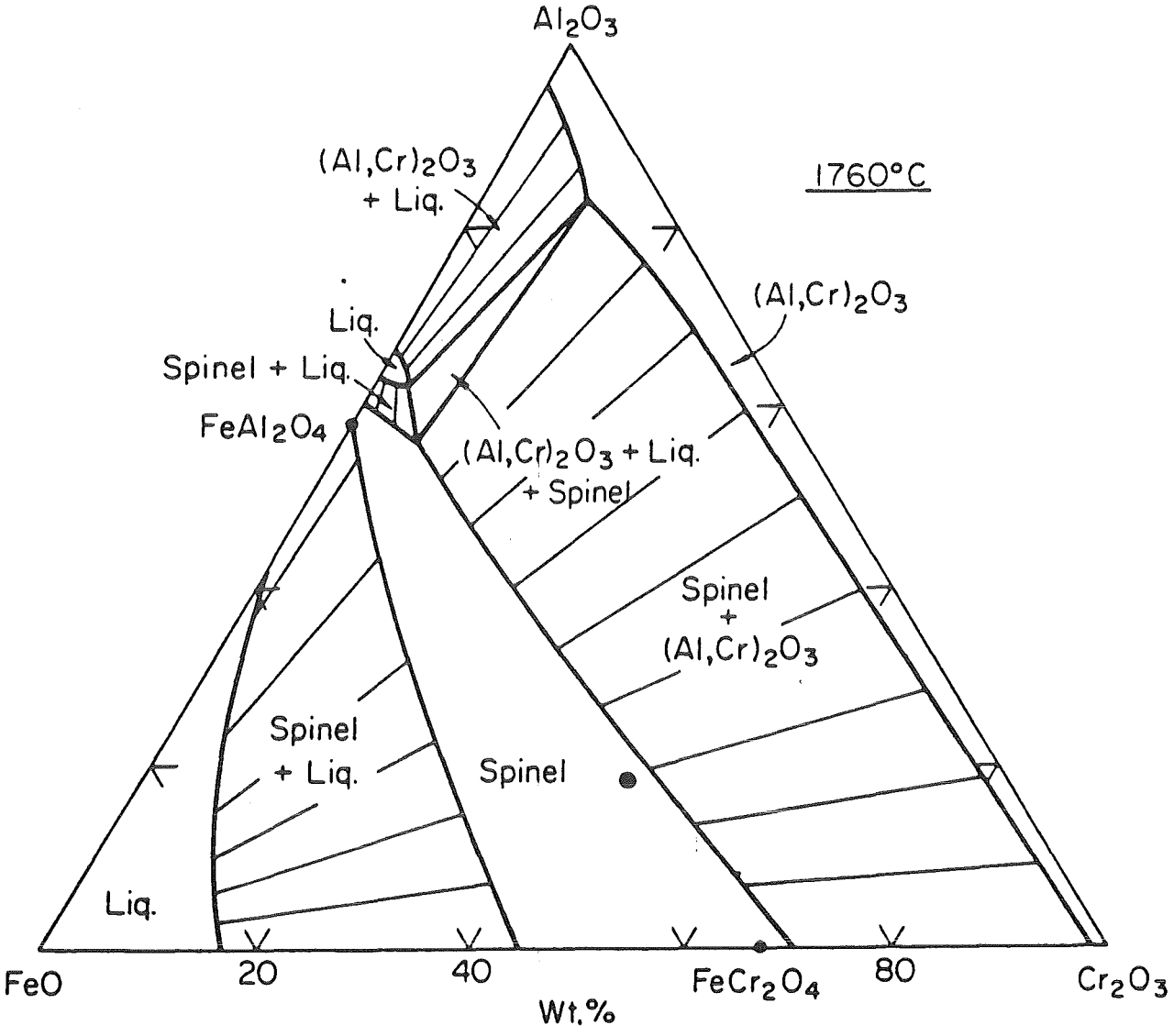

Fig. I: Isothermal section of the pseudoternary $FeO-Cr_2O_3-Al_2O_3$ system at 1760 °C. Compositions in wt.%. The dot in the single-phase field illustrates the observed $Fe(Cr,Ni,Zr)_{1.4}Al_{0.6}O_4$ composition of the spinel.

J. The pseudobinary UO2-steel system

The phase diagram of the pseudobinary UO_2-Fe system in fig. J is based on unpublished experiments [17]. The mutual solubility of UO_2 and steel is negligible below 2500 °C. A monotectic reaction, $\{(U,St)O_2\} = <UO_2> + \{steel\}$, occurs just below the melting point of UO_2, see fig. J.

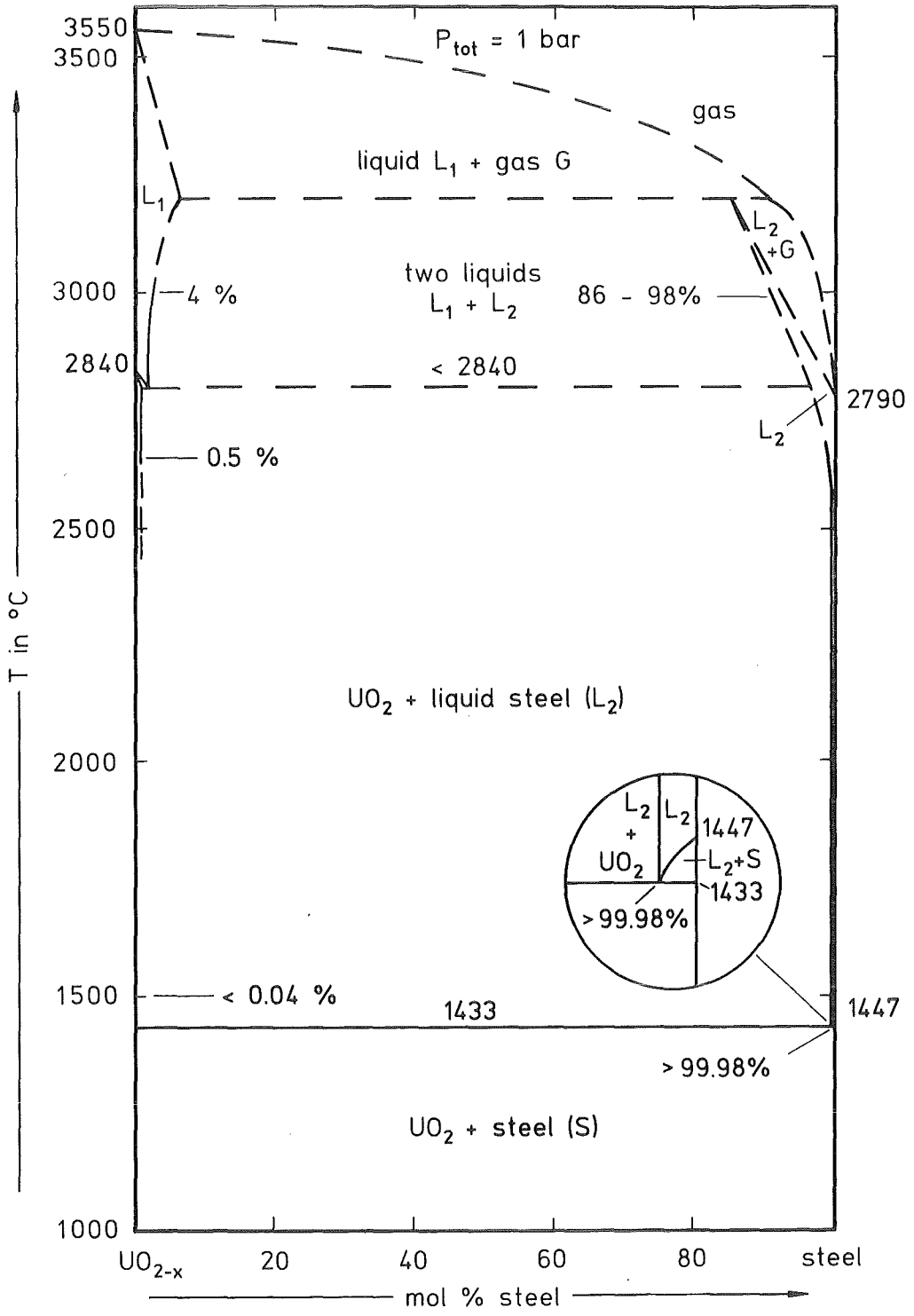

Fig. J: Phase diagram of the pseudobinary UO_2-AISI 316 system

References for the constitution diagrams

[1] T.B. Massalski, Binary Alloy Phase Diagrams, ASM, 1986

[2] E.M. Tararaeva, O.S. Ivanov, Stroenie i Svoistva Splavov dlya Atom. En., Nauka Moskwa, 1973, p. 131-138

[3] Y. Muraoka, M. Shiga, Y. Nakamura, phys. stat. sol. (a) 42 (1977) 369-374

[4] V.N. Svechnikov, A.T. Spektor, Vopr. Fiz. Metallov Metalloved. No. 17 (1963) 181-186

[5] V.N. Svechnikov, V.J. Markiv, V.V. Petkov, Metallofiz., Akad. Nauk Ukrain SSSR 42 (1972) 112-116

[6] M.V. Nevitt, J.W. Downey, R.A. Morris, Trans. Met. Soc. AIME 218 (1960) 1019-1023

[7] H. Holleck, F. Thümmler, J. Nucl. Mater. 23 (1967) 88-94

[8] J.F. Collins, I.F. Ferguson, J. Chem. Soc. (A) 1988, 4-5

[9] S. Ferrier, M. Therasse, G. Montel, Comptes Rend. C 268 (1969) 1043-1046

[10] S.K. Rhee, M. Hoch, Trans. Met. Soc. AIME 230 (1964) 1687-1690

[11] G. Petzow, G. Effenberg, Ternary Alloys, Verlag Chemie, 1988

[12] C. Politis, KfK 2167 (1975)

[13] A. Skokan, in KfK 3880 (1984) 1035-1042

[14] K.A. Romberger, C.F. Baes, H.H. Stone, J. Inorg. Nucl. Chem. 29 (1967) 1619-1630

[15] J.O.A. Paschoal, H. Kleykamp, F. Thümmler, J. Nucl. Mater. 151 (1987) 10-21

[16] K. Rosenbach, J.A. Schmitz, Arch. Eisenhüttenw. 45 (1972) 843-847

[17] H. Kleykamp, unpublished